Seismic assessment of a hybrid light wood-frame structure connected to a balloon-type CLT core

by

Ariya Eini

B.Sc., AmirKabir University of Technology, Iran, 2017

M.Sc., AmirKabir University of Technology, Iran, 2019

A Dissertation Submitted in Partial Fulfillment

of the Requirements for the Degree of

DOCTOR OF PHILOSOPHY

in the Department of Civil Engineering

University of Victoria

We acknowledge with respect the Lək^{w}əŋən peoples on whose traditional territory the university stands and the Songhees, Esquimalt and W̱SÁNEĆ peoples whose historical relationships with the land continue to this day.

Seismic assessment of a hybrid light wood-frame structure connected to a balloon-type CLT core

by

Ariya Eini

B.Sc., AmirKabir University of Technology, Iran, 2017

M.Sc., AmirKabir University of Technology, Iran, 2019

Supervisory Committee

Dr. Lina Zhou, Co-supervisor

Department of Civil Engineering

Dr. Chun Ni, Co-supervisor

Department of Civil Engineering

Dr. Phalguni Mukhopadhyaya, Department Member

Department of Civil Engineering

Dr. Minghao Li, Outside Member

Department of Wood Science, University of British Columbia

Abstract

Light wood-frame structures are the most common type of construction for residential and low-rise buildings in North America. The 2015 edition of the National Building Code of Canada has increased the height limit for light wood-frame construction from 4 to 6 stories. With the increase in building height, the design of light wood-frame structures may be more likely governed by inter-story drift under wind and seismic loads. To reduce the inter-story drift, a hybrid system, consisting of CLT cores and light wood-frame structures, is proposed in this study. Given the lack of design guidelines on the performance of hybrid wood structures under seismic loads, it is imperative to gain a comprehensive understanding of their performance under earthquake load that includes the hybrid performance, as well as performance of individual sub-structure and inter-structure connections.

The first part of this study focuses on assessing the influence of energy dissipation due to different pinching levels on the seismic performance of individual sub-structure, i.e., a light wood-frame shear wall system, over a wide range of fundamental periods. The study revealed that structures with periods less 0.7 s are more susceptible to the effects of hysteresis loop pinching than long-period structures. The residual strength of pinching loops has a greater influence on the seismic performance than the stiffness of the pinching loops. Hysteretic energy dissipation derived from standard reversed-cyclic tests can provide a better understanding on the seismic resistance of timber structures. However, the hysteretic energy under a seismic event at near-collapse stage neither agrees with quasistatic cyclic test's energy dissipation nor is well correlated to the maximum seismic capacity of the structure.

In the second part of this study, monotonic and reversed-cyclic tests were conducted on the connections between the two subsystems in the proposed hybrid building. The CLT core and light wood-frame structures were connected on the floor level with self-tapping screws (STSs) inserted

at 45°, 90°, and mixed angles (45° and 90°). Results show that 45° STSs connections had high stiffness but low energy dissipation, while 90° STS connections had high energy dissipation but low stiffness. Mixed-angle Connections had significantly higher ductility and energy dissipation compared to connections with STSs only inserted at 45° or 90°.

The final part of this study investigated the effect of STS connection ductility on the seismic performance of a hybrid building consisting of light wood-frame shear walls and a balloon-type CLT core. The National Building Code of Canada requires the lowest seismic force modification factors (R_dR_o) of the subsystems be used for the design of a hybrid building if the subsystems are rigidly connected, which may be conservative if a ductile connection is used. Therefore, a numerical study was conducted to determine the possibility of utilizing higher R_dR_o values for the design of the proposed hybrid structures. Hybrid models were developed where the two subsystems were connected using STS inserted at 45°, 90°, and mixed angles (45° + 90°). Pure light wood-frame structures and pure CLT structures were also analyzed as reference cases. One-, four- and six-storey archetypes were designed with trial R_dR_o factors. The OpenSees software was used to develop a 2D numerical model for each archetype. The R_dR_o of the five analyzed cases was evaluated following the Canadian Construction Materials Centre guideline and using the 22 FEMA P695 far-field ground motions. The results show that R_d = 2 and R_o = 1.5 are acceptable for cases of pure CLT structures, and hybrid structures connected using STS inserted at 45° and 90°. The hybrid buildings connected using STS inserted at mixed angles (45° + 90°) can be assigned with R_d = 2.5 and R_o = 1.5. The archetypes designed with R_d = 3 and R_o = 1.7 are deemed satisfactory for pure light wood-frame structures.

Table of Contents

List of Figures

List of Tables

List of Symbols, Nomenclature or Abbreviations

α	Stiffness degradation parameter (SAWS model).
a_p	Pinching stiffness degradation factor
a_r	Reloading stiffness degradation factor
a_u	Unloading stiffness degradation factor
β (SAWS)	Stiffness degradation parameter.
β (DowelType)	Reloading target displacement amplification factor
C	Curve shape factor
CLT	Cross-laminated timber
COV	Coefficient of variation
CUREE	Consortium of universities for research in earthquake engineering
d	Screw diameter
D_1	Displacement of interpolation point 1
D_2	Displacement of interpolation point 2
D_3	Displacement of interpolation point 3
D_4	Displacement of interpolation point 4
D_{b1}	Displacement of the first controlling point
D_{b2}	Displacement of the second controlling point
DBE	Design-basis earthquake
D_c	Displacement of the cap point
DU	Displacement at ultimate load
D_u	Ultimate displacement
D_{ue}	Ultimate displacement of elastic system
D_{up}	Ultimate displacement of plastic system
D_y	Apparent yielding displacement
D_y	Yield displacement
E	Modulus of elasticity
EEEP	Equivalent energy elastic-plastic
EMC	Equilibrium moisture content
EPP	Elastic-perfectly plastic
ESPF	Equivalent static force procedure
ESPF	Equivalent static force procedure
Ey	Hysteretic yielding energy

$F0$	Intercept strength for the asymptotic line to the envelope curve.
F_1	Force of interpolation point 1
F_2	Force of interpolation point 2
F_3	Force of interpolation point 3
F_4	Force of interpolation point 4
f_b	Bending at extreme fibre
F_{b1}	Force of the first controlling point
F_{b2}	Force of the second controlling point
F_c	Force of the cap point
f_c	Compression parallel to grain of wood
f_{cp}	Compression perpendicular to grain
FI	Residual strength (Intercept strength of the pinching branch of the hysteretic curve)
F_{I0}	Intercept strength of the pinching branch of the hysteretic curve
F_{peak}	Peak force
f_s	Rolling shear of wood
f_t	Tension parallel to grain
FT	Fully-threaded
f_v	Longitudinal shear
F_y	Yield force
γ (DowelType)	Reloading degradation factor due to energy dissipation in DowelType material
G	Shear modulus
γ	Capacity adjustment factor (overstrength factor)
GPWL	General piece-wise linear
η	Pinching intercept moving parameter
h	Total building height
HD	Hold-down
IDA	Incremental dynamic analysis
K	Elastic stiffness
K_d	Descending absolute stiffness
K_{p0}	Pinching branch stiffness
K_{u0}	Unloading stiffness to initial stiffness ratio
LLRS	Lateral-load resisting system
LVDT	Linear variable differential transformers

LWF	Light wood-frame
MCE	Maximum considered earthquake
MDOF	Multi-degree-of-freedom
MISD	Maximum interstorey drift ratio
PT	Partially-threaded
R1	Stiffness ratio of the asymptotic line to envelope curve.
R2	Stiffness ratio of the descending branch of the envelope curve.
R3	Stiffness ratio of the unloading branch off the envelope curve.
R4	Stiffness ratio of the pinching branch.
$R_{95^{th}}$	95th percentile of ultimate strength
R_d	Ductility related force modification factor
R_{design}	Design force of the connection
$R_{max,\ mean}$	Mean of test's maximum resistance
R_o	Over-strength related force modification factor
S0	Initial stiffness of the spring element.
Sa	Spectral acceleration
SC	Shear connector
SDOF	Single-degree-of-freedom
SPF	Spruce-pine-fir
STS	Self-tapping screw
T_a	Fundamental period
UHS	Uniform hazard spectrum
V_e	Elastic seismic force as determined by linear dynamic analysis procedure
V_y	Yield seismic force
ζ_{hyst}	Equivalent viscous damping
Δ_{peak}	Displacement at peak force
Δ_u	Ultimate displacement
Δ_y	Yield displacement
μ	Ductility ratio

Author Contributions

The core of this dissertation is composed of three chapters that are based on four peer-reviewed manuscripts. The author list, title, and author contributions are clarified below for each core chapter.

Published papers:

[1] Eini, A., Zhou, L., and Ni, C. (2021). Pinching effect on seismic performance of a SDOF light wood-frame timber structure. In Proceeding of the World Conference on Timber Engineering, Santiago, Chile.

Ariya Eini: Investigation, Methodology, Formal analysis, Writing - original draft

Lina Zhou: Conceptualization, Methodology, Funding acquisition, Supervision, Review

Chun Ni: Conceptualization, Methodology, Review

[2] Eini, A., Zhou, L., and Ni, C. (2022). Behavior of self-tapping screws used in hybrid light wood-frame structures connected to a CLT core. *Buildings*, *12*(7), 1018.

Ariya Eini: Investigation, Methodology, Formal analysis, Writing - original draft

Lina Zhou: Conceptualization, Methodology, Funding acquisition, Supervision, Review

Chun Ni: Conceptualization, Methodology, Review

[3] Eini, A., Zhou, L., and Ni, C. (2022). Cyclic and monotonic test of self-tapping screw connections used in CLT-light wood-frame hybrid structures. In Proceeding of the International Conference on New Horizons in Green Civil Engineering, Victoria, Canada.

Ariya Eini: Investigation, Methodology, Formal analysis, Writing - original draft

Lina Zhou: Conceptualization, Methodology, Funding acquisition, Supervision, Review

Chun Ni: Conceptualization, Methodology, Review

Accepted paper:

[4] Eini, A., Zhou, L., and Ni, C. (2023). Seismic assessment of a hybrid light wood-frame structure connected to a balloon-type CLT core. In Proceeding of the Canadian Conference - Pacific Conference on Earthquake Engineering, Vancouver, Canada.

Ariya Eini: Investigation, Methodology, Formal analysis, Writing - original draft

Lina Zhou: Conceptualization, Methodology, Funding acquisition, Supervision, Review

Chun Ni: Conceptualization, Methodology, Review

Acknowledgments

I would like to acknowledge the support and patience of my supervisor, Dr. Lina Zhou, and co-supervisor, Dr. Chun Ni, whose guidance was invaluable in the completion of this project.

I would also like to extend my gratitude to the member of the committee, Dr. Phalguni Mukhopadhyaya and Dr. Minghao Li, for their time, effort.

I am also grateful for the support provided by the lab technician, Solomon Rosenberg. His technical expertise and assistance with laboratory experiments were critical to the success of my research project.

My heartfelt thanks also go to my research group, who have always been there for me, providing support and encouragement through the ups and downs of my PhD journey.

Lastly, I would like to thank the UVic community and professionals at FPInnovations and MTC solutions that have provided the resources and opportunities for me to pursue my research. Their contributions to the advancement of knowledge in my field have been an inspiration.

Chapter 1 Introduction

Light wood-frame (LWF) construction are most commonly used in North America for low-rise residential buildings [1]. In recent years, there has been an increase of interest in utilizing timber as a primary construction material in taller buildings in urban areas, driven by its low carbon footprint, aesthetic appeal, and ease of construction. Furthermore, wooden materials are increasingly becoming a desirable choice for mid-rise buildings due to their high strength-to-weight ratio [2]. However, despite the recent developments, the application of LWF in mid-rise (up to six storeys) structures is still limited and requires further investigation to address the technical challenges.

1.1 Problem Statement and Background

1.1.1 Architectural Issues

The lateral-load resisting system (LLRS) of LWF buildings typically consist of a large number of framing elements (studs and plates) and wood-based panels that are jointed together by fasteners (e.g., nails, screws or staples). LWF structures are characterized by their high degree of redundancy and energy absorption capabilities through the slip of numerous nailing connections, enabling them to withstand earthquakes well in the past [3]. However, the low shear strength per unit length of LWF walls forces engineers to fit numerous shear walls in a LWF construction which can constrain the architectural design, particularly in terms of open-space design concepts that are becoming increasingly popular [4]. This issue becomes more pronounced for taller structures since the design shear force accumulates with building height, necessitating a denser placement of wood shear walls [5]. Therefore, there is an urgent need to explore alternative systems for lateral load resistance that can offer greater design flexibility while maintaining structural safety. A hybrid system utilizing the resistance of elevator shaft and stair well cores in light wood-frame buildings could be an option to

increase the lateral resistance and stiffness of mid-rise wood-frame buildings, which were investigated in this study.

1.1.2 Pinching Effect

Previous research has established that the LWF shear walls exhibit sufficient amount of cyclic ductility and their global response is highly influenced by the load-displacement of the fasteners [6] and base connections [7]. The current forced-based seismic design codes only account for the characteristics of backbone curves and do not consider other hysteretic features that can affect energy dissipation. For example, ASTM D7989 [8] only considers ductility and ultimate displacement (drift capacity) as the criteria for establishing seismic performance equivalency for LWF shear walls. Nonetheless, timber structures are more susceptible to degradation effects, particularly pinching, during repeated loading in an earthquake compared to steel and concrete buildings [9].

When joints and connections are laterally loaded, fasteners (pinching element) induce local plasticization in wood elements (pinched element)[10]. During the reversed loading, the metal fastener encounters little resistance due to the crushed wood fibers that have already been deformed during the initial loading. This effect appears in hysteresis loops as a significant reduction of stiffness in reloading phase after the first load cycle. In subsequent cycles, and before reaching the maximum deformation achieved in the previous cycle, the fastener compresses the wood material further and resulting in the pinching phenomenon spreading to other adjacent wood fibers.

Aloisio et al. [10] acknowledged that pinching effects should be considered in the development of seismic demand models for LWF shear walls. ASCE SEI 41-17 [11] has incorporated the effect of pinched hysteresis shape, cyclic stiffness degradation, and strength deterioration on the Nonlinear Static Procedure used for retrofitting existing structures. ASCE SEI 41-17 defines only one modification factor that considers the mentioned effects in calculating the pseudo seismic force and

the target displacement of nonlinear static analysis. However, each timber structure has its peculiar pinching characteristics which differs along the unloading and reloading path. Experiments in the literature have shown that pinching impairs the cyclic behavior of connections and it is considered as one of the weaknesses of timber structures [12].

1.1.3 Structural Design Challenges

Using LWF shear walls in construction poses serious challenges in wind design, including insufficient weight to resist overturning forces, and potentially inadequate stiffness which makes it highly vulnerable to wind damage, especially during hurricanes [13]. Another concern is the resistance, serviceability limitation and fire safety of LWF construction [14]. As a result, the National Building Code of Canada (NBCC 2020) [15] has restricted the height of LWF buildings to six stories. At the same time, the NBCC 2020 introduced a significant increase in seismic hazard spectrum compared to its previous provisions. The lack of lateral stiffness poses a significant challenge for designers attempting to meet the drift requirements necessary for seismic design in mid-rise light wood-frame buildings. Therefore, new approaches are needed that can provide superior performance and meet the updated seismic demands of guidelines.

In the recent years optimization of construction process and innovative solutions [16] for LWF shear walls have made possible the rapid development of mid-rise LWF construction. Despite significant advancements in engineering practice, structural design codes have not been updated accordingly to reflect these developments. This is particularly evident in the seismic design of hybrid structures using the equivalent static force procedure (ESFP). NBCC [15] recommends using the lowest value of the seismic force modification factors (R_dR_o) of individual systems when designing a hybrid structure. This means that the higher energy dissipation capacity of the more ductile system would be ignored in the design, which may be a conservative approach.

In design practice, the structural system should be clearly identified to avoid misinterpretation of the components contributing to the energy dissipation capacity. Elevator shafts and stairwells commonly exist in multi-story buildings and can be used as part of the lateral load resisting system to reduce the lateral drift of the light wood-frame system. The core walls are sometimes constructed using Cross-Laminated Timber (CLT) which are composed of a number of crosswise glued-laminated panels. CLT panels behave quite rigidly and are ideal for transmitting high seismic forces to the foundation [17]. NBCC [15] does not provide design details for CLT core-walls and it sets the seismic force modification factors for platform-type CLT structures as $R_dR_o = 2 \times 1.5$. However, the LWF structures can be designed using $R_dR_o = 3 \times 1.7$. According to NBCC, a hybrid building composed of a LWF structure and CLT core walls (LWF/CLT) should be designed with the lowest R_dR_o of the two subsystems (i.e., $R_dR_o = 2 \times 1.5$). Consequently, from the design engineer's point of view, connecting these walls to the LLRS does not provide any advantages in reducing the total design forces.

In addition, there are limited detailing provisions for dissipative and non-dissipative elements of hybrid LWF/CLT systems. Therefore, it's typical for engineers to exclude the walls that support elevators and stairs from the lateral load-resisting system in light wood-frame structures[14].

Further study on hybrid LWF/CLT systems is needed to facilitate their implementation, as well as to investigate their individual components. Specifically, there is a lack of studies investigating the pinching effect and its impact on the seismic performance of LWF buildings. In addition, to address the low stiffness problem of LWF construction, CLT core walls have been suggested as an effective solution; however, new connections need to be developed to increase the ductility level of the CLT core system or the connection between the LWF structure and CLT core wall. Therefore, this study

aims to investigate these research gaps to improve the design and construction of hybrid LWF/CLT systems.

1.2 Objectives

The main objective of this research project is to gain a deeper comprehension of the seismic behavior and the interaction between a light wood-frame structure and a CLT core wall within a hybrid structure, and to explore how the inherent properties of connections between the two subsystems impact the seismic performance of the building. The following objectives have been identified:

1. To understand the pinching effect in hysteresis loops of substructures, i.e., light wood-frame buildings and its influence on the energy dissipation and seismic collapse capacity.
2. To determine possible connection solutions for the hybrid LWF/CLT structure and evaluate their shear behavior under reversed-cyclic and monotonic loadings. Moreover, to optimize the ductility and energy dissipation of the CLT-lumber connection using different self-tapping screw insertion angles.
3. To develop 2D finite-element models of a hybrid LWF/CLT system and to quantify the seismic force modification factors for mid-rise hybrid LWF/CLT systems using the Canadian Construction Material Center (CCMC) guideline [18].

The focus of this study is to demonstrate the efficiency of the hybrid LWF/CLT structure for application in high seismic hazard zones. The main contribution is the estimation of seismic force modification factors for design of the hybrid LWF/CLT structure and evaluating the adequacy of the proposed design procedures.

1.3 Organization of Dissertation

In order to accomplish the aforementioned objectives and to attain the expected significance, a range of procedures were implemented, which are outlined below.

Chapter 2 investigates the impact of pinching effect in hysteresis loops on the seismic collapse capacity of substructure, i.e., light wood-frame buildings. To evaluate how the seismic collapse capacity changes with respect to variations in pinching levels, single-degree-of-freedom systems with varying pinching stiffness and residual strength were analyzed.

Chapter 3 presents experimental tests of self-tapping screw connections between floor headers of light wood-frame floor diaphragms and the CLT wall panel. Three types of connection configurations with different STS insertion angles (90° STS, 45° STS, and mixed angle STS) were studied under monotonic and reversed-cyclic loading. Each configuration was tested using screws with diameters of 8mm and 10 mm. Four replicates were tested for each configuration, and there were 48 specimens tested in total. The hysteretic load-displacement curves derived from the tests were used to calibrate the finite-element models for connections used in the next chapter.

Chapter 4 evaluates the seismic performance of the hybrid LWF/CLT structure through incremental dynamic analysis of 2D finite-element models. CCMC procedure [18] was used to quantify the seismic force modification factors for designing the hybrid LWF/CLT structure. Hybrid structures were developed based on different ductility and energy dissipation levels of connections (90° STS, 45° STS, and mixed angle STS) and were compared with structures constructed from pure light wood frame and pure CLT core.

Chapter 5 discusses key findings and recommendations of this research.

This dissertation is structured in a manuscript-based format, featuring four manuscripts referred to in chapter 2 , 3 and 4. The first three manuscript have already been published [19], [20] and [21] .The

fourth manuscript has been accepted for publication at the time of submitting this dissertation. Rather than including a separate literature review chapter, the relevant literature has been integrated throughout Chapters 2 to 4.

Chapter 2 Pinching Effect on Seismic Performance of a SDOF Light Wood-Frame Timber Structure

2.1 Introduction

Most common seismic design practices rely on the ductility and damping of the structural system to dissipate energy under seismic load. The ductility factor is defined as the ratio of the deformation at the failure stage to the deformation at yield. It is derived from the backbone of the hysteresis curves without considering the effect of pinching on the energy dissipation of the structure. In timber construction, such as light wood-frame shear wall systems, the force-deformation relationship is usually highly nonlinear and pinched. The current seismic design codes only account for the characteristics of backbone curves without consideration of energy dissipation. For example, ASTM D7989 [8] only considers ductility, ultimate displacement (drift capacity) as criteria for establishing seismic performance equivalency.

However, previous studies have shown that the strength and stiffness degradation, and pinching of hysteresis loops do affect the seismic response of structures. Hyung Lee et al. [22] established the functional form of ductility-related seismic force modification factor (R_d) based on various hysteretic models, including pinched models with different residual strength. A lower R_d was obtained with an increase of pinching level. A study by Paevere and Foliente [23] focused on generating response statistics for generic single-degree-of-freedom (SDOF) systems, using the Bouc-Wen-Barber-Noori hysteresis model [24] and 8 general piece-wise linear (GPWL) models. The GPWL models covered all possible combinations of strength and stiffness degradation and full pinching (zero residual strength and zero pinching stiffness). Large variation was observed for both maximum displacement and energy dissipation values. Medina and Krawinkler [25] evaluated the sensitivity of story drifts

of frame structures to three types of hysteresis models: peak-oriented, bilinear and pinching. They found that pinched models have higher displacement demands than those without pinching, which was more evident in multi-degree-of-freedom (MDOF) systems than SDOF systems. Another study by Goda et al. [26] on probabilistic characteristics of inelastic SDOF systems revealed that shape, degradation and pinching parameters of Bouc-Wen hysteresis model [24] had significant effect on ductility demand of structures. Pu and Wu [27] compared bilinear hysteretic SDOF systems with pinched hysteresis systems and concluded that the pinched structures were more affected by seismic sequences.

Hysteretic yielding energy (*Ey*) has proven to be one of the key factors affecting the seismic capacity of structures. Researchers have tried to establish the correlations between the Ey and the other hysteresis properties of a system. *Ey* is the energy dissipated through inelastic performance. A study by Gebrekirstos Mezgebo [28] showed that the *Ey* demand for different hysteresis models varies in the following order: bilinear plastic model > strength degradation model > bilinear flag model > bilinear slip model. Molazadeh et al. [29] demonstrated that in short-period pinched models, the ground motion duration had significant influences on the central tendency of *Ey* and ductility demand of the structures. Kazantzi and Vamvatsikos [30] conducted incremental dynamic analysis (IDA) on kinematic hardening model, curved kinematic hardening model, peak-oriented model, flag-shaped model, pinching model, and nonlinear elastic model. No consistent correlation was found between the *Ey* values and seismic demand of structures.

The above-mentioned studies are mostly focused on hysteresis loops of typical steel and reinforced concrete structures. Research on the effect of pinching characteristics on seismic performance of timber structures is limited. In this paper, incremental dynamic analysis was conducted on 72 SDOF

timber structures with different pinching levels and fundamental periods via OpenSees [31] to investigate the influence of energy dissipation on the seismic performance of timber structures.

2.2 Numerical Modeling Analysis

2.2.1 Hysteretic Model

SAWS model [32] in OpenSees was adopted in this project to simulate the hysteresis performance of wood shear walls. The SAWS model is composed of a series of segmental linear functions and an exponential function describing the envelope curve until the peak load (**Figure 2.1**a). The unloading path includes two segments, the elastic unloading phase and the pinched unloading phase. The reloading path also includes two segments, the pinched reloading phase and the stiffness recovering phase. The stiffness of pinched phases and the residual strength (intercept resistance at zero displacement) represent the level of pinching and affect the hysteretic energy dissipated in a hysteresis loop.

There are ten parameters in the SAWS model (**Figure 2.1**a) to describe the hysteresis loops, in which *S0* is the initial stiffness of the structure; *R4* is the ratio of the pinching stiffness to the initial stiffness, and *FI* is the residual strength of the system, etc. To obtain the SAWS hysteresis characteristics, a simple shear wall model was developed in OpenSees with three rigid truss elements and one bracing diagonal spring (**Figure 2.1**b). It is a 2-dimensional (2D) simulation of the shear wall with pin support connections. A fitting procedure was employed to calibrate these 10 parameters based on a quasi-static reversed-cyclic test of a wood shear wall by Zhou [14]. **Figure 2.2** shows the comparison of the numerical hysteresis loops of the reference case (model S1 in **Table 2.1**) with experimental hysteresis loops. **Figure 2.3** shows the cyclic cumulative energy history of the calibrated numerical model (S1) which is in good agreement with the test data by a difference of ± 5%. The 10 calibrated parameters for S1 are listed in **Table 2.1**.

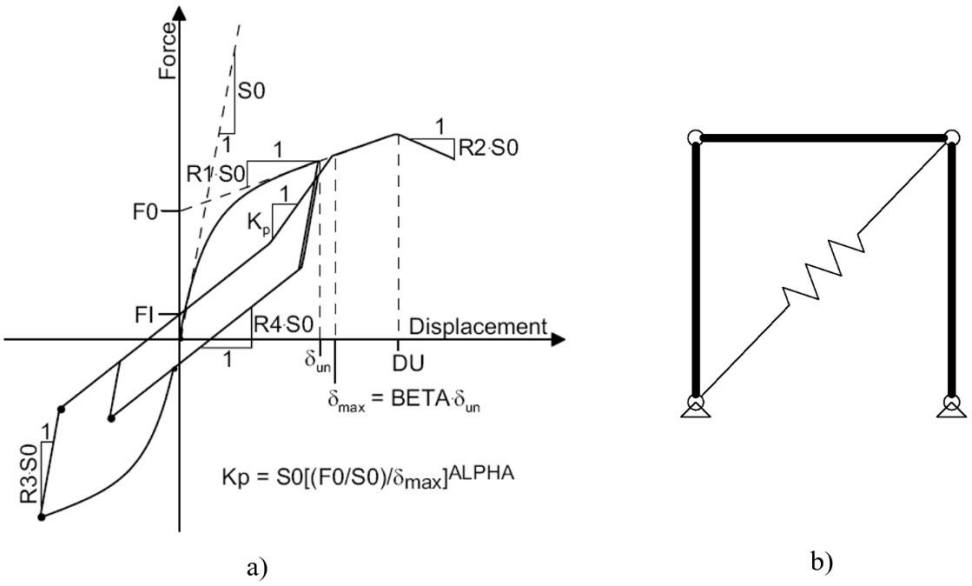

Figure 2.1. Numerical model of SDOF system: (a) SAWS-10 parameters; and **(**b) 2D finite element model.

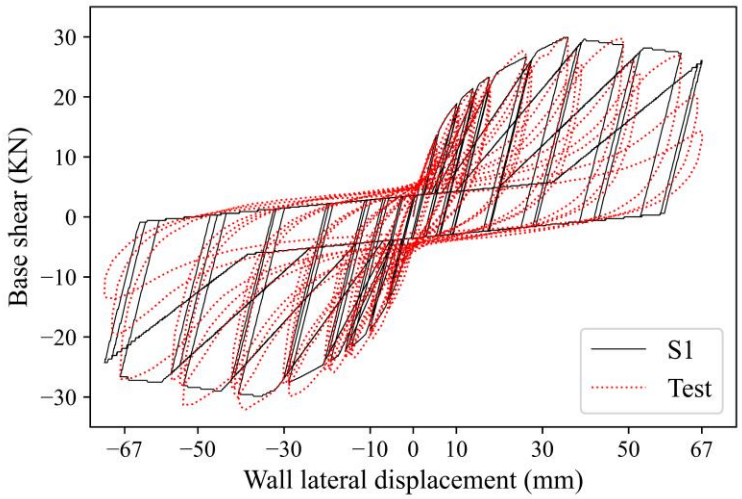

Figure 2.2. Comparison of hysteresis loops between the test and the numerical model (S1).

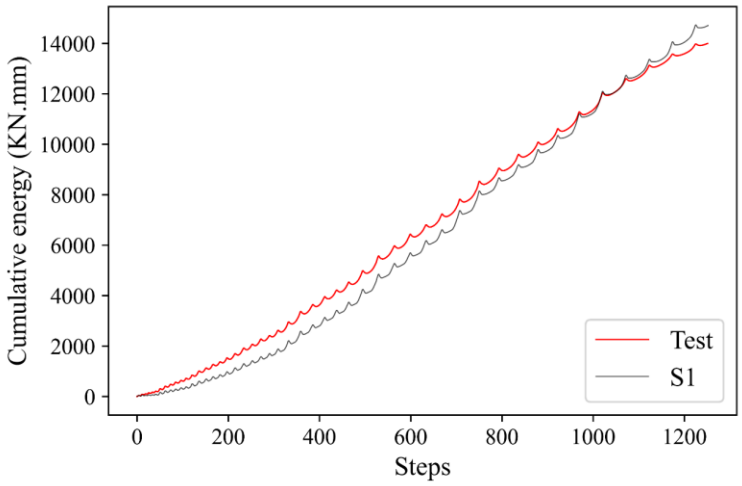

Figure 2.3. Comparison of hysteretic energy between the test data and the numerical model (S1).

Table 2.1 Hysteretic parameters for shear wall spring elements

Models	*S0 (kN)*	*DU*	*α*	*ß*	*R1*	*R2*	*R3*	*R4*	*F0* (kN)	*FI* (kN)
S_1(reference)	7.7	25	0.7	1.1	0.09	-0.025	0.75	0.018	25	5
S_2	7.7	25	0.7	1.1	0.09	-0.025	0.75	0.018	25	2
S_3	7.7	25	0.7	1.1	0.09	-0.025	0.75	0.018	25	10
S_4	7.7	25	0.7	1.1	0.09	-0.025	0.75	0.005	25	5
S_5	7.7	25	0.7	1.1	0.09	-0.025	0.75	0.045	25	5

2.3 Structures with Varying Pinching Level

Pinched hysteresis loop is a typical feature of wood shear walls under reversed cyclic load. Under the cyclic load, fasteners crush the wood fibers, creating permanent gaps between the fastener and wood material. When the nails are loaded in the opposite direction passing through the gaps, they face a reduced resistance due to indented wood [33]. Softening of the fasteners and crushing of wood fibers make the area under the force-deformation curves pinched.

The pinching degree is controlled by both the residual strength and its stiffness. To assess the pinching effect, besides S1 which is based on an actual test result, four other pinching models with the same backbone curve but different residual strength or pinching stiffness were developed (**Figure**

2.4). Models S2 and S3 (**Figure 2.4**a) were assigned with different residual strength (*FI*), while models S4 and S5 (**Figure 2.4**b) were assigned with different pinching stiffness. The range of residual strength and pinching stiffness were selected based on available test results [6], [34-43]. **Table 2.1** lists the 10 parameters for all SAWS models. An Elastic Perfectly Plastic (EPP) model based on the equivalent energy elastic-plastic method [44] derived from the backbone of test hysteresis loops was also investigated (**Figure 2.4**c).

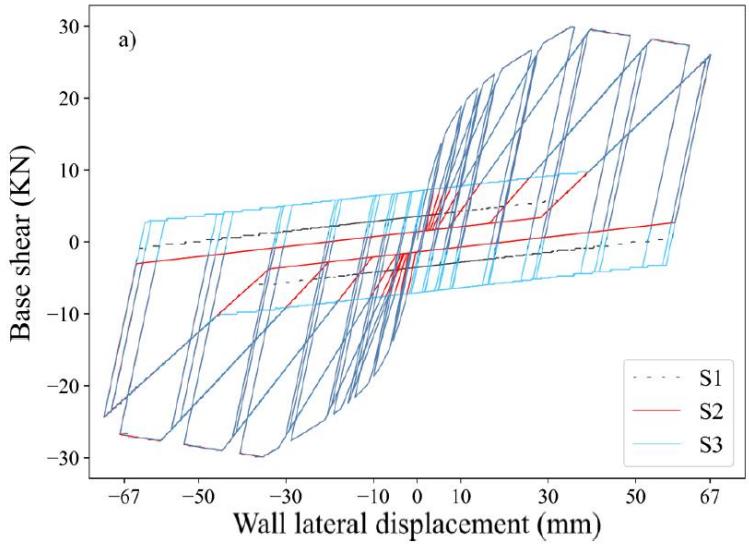

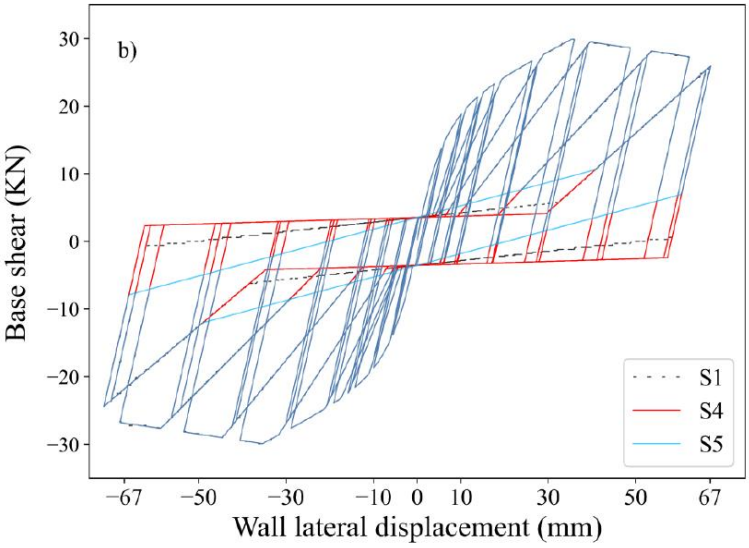

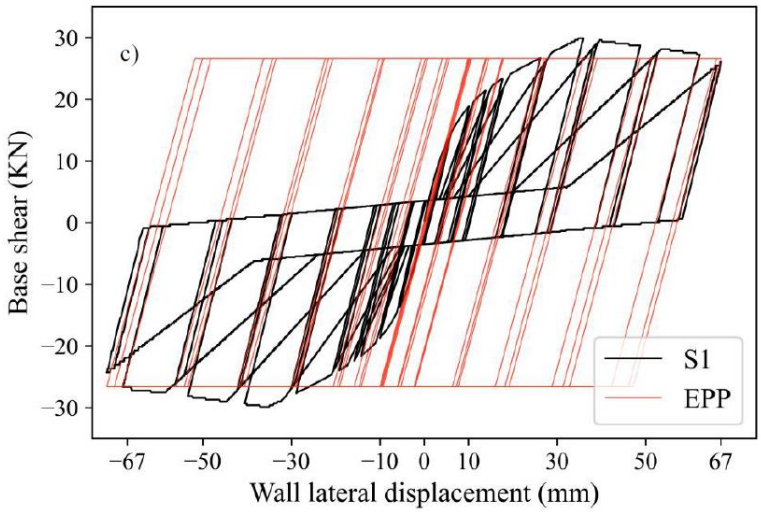

Figure 2.4. Comparison of hysteresis models to the reference case S1: (a) residual strength (S2 and S3); (b) pinching stiffness (S4 and S5); and (c) Elastic Perfectly Plastic (EPP).

Figure 2.5 presents the energy dissipation history of all SAWS models. The cumulative energy from reversed-cyclic test for five SAWS models and the EPP model is listed in **Table 2.2**. Compared to the reference case S1, S2 with lower residual strength has lower (21% less) energy dissipation capacity and S3 with higher residual strength has higher (37% more) energy dissipation capacity. The energy dissipation of S4 with lower pinching stiffness is 5% more than that of S1. On the other hand, S5 with higher pinching stiffness had an energy dissipation 11% less than S1. Generally, this hysteresis energy is more sensitive to a change of the residual strength than that of the pinching stiffness. The order of models from the highest energy dissipation capacity under standard loading protocol to the lowest is EEP > S3 > S4 > S1 > S5 > S2.

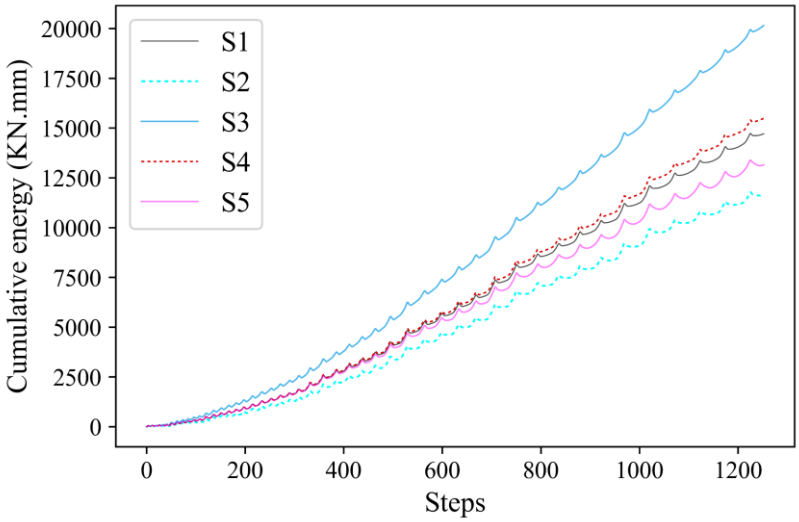

Figure 2.5. Comparison of hysteretic energy history of SAWS models.

Table 2.2. Comparison of all models' cumulative hysteretic energy.

Models	S1	S2	S3	S4	S5	EPP
Energy (kN.mm)	14707	11621	20144	15478	13147	51600
Energy ratio to S1	1	0.79	1.37	1.05	0.89	3.51

2.4 Incremental dynamic analysis

Incremental dynamic analysis (IDA) [45] was conducted to investigate the seismic response of the SDOF timber structures under a suite of 22 far-field ground motions (two horizontal components per motion) from FEMA P-695 [46]. The intensity measure was represented by the spectral acceleration (*Sa*) at the fundamental period of the SDOFs, and the damage measure was chosen to be the lateral displacement of the SDOF system. In this research, twelve fundamental periods (0.1 s, 0.2 s, 0.3 s, 0.4 s, 0.5 s, 0.6 s, 0.7 s, 0.8 s, 0.9 s, 1 s, 1.5 s, 2 s) that cover the common periods of timber structures in practice were analyzed for each hysteretic model by changing the assigned mass. Mass was lumped at the top two nodes of the wall. The viscous damping ratio of 1% was applied as suggested in [47]. Although some references reported higher critical damping but the purpose of this

study was to investigate the significance of yielding hysteresis energy, so the lower bound was selected.

IDA was carried out on the 72 SDOF systems by scaling up each record until the near-collapse stage. Failure of the structures is defined as when the ultimate lateral displacement reaches to 67 mm based on the shear wall test data (deformation which load drops below 80% of maximum resistance) or the tangent slope of the IDA curve (**Figure 2.6**a) drops to 20% of the initial slope [48], whichever comes first. A total of 63360 nonlinear dynamic analyses were run.

In IDA analysis, the *Sa* value causing near-collapse of a SDOF system was captured first with reduced scaling intervals. The tolerance of maximum lateral displacement at the near-collapse stage and failure of the structure falls within 1 mm. Once the *Sa* at the near-collapse stage for different ground motion records and hysteresis models were obtained, these *Sa* values were divided into 20 equal steps to trace the grid points of IDA curves. Since the *Sa* values causing failure of the structures are different for different ground motions and different hysteresis models, the *Sa* interval is not consistent in this project. **Figure 2.6**a shows an example of the IDA curves for S1 model with period of 0.2 s under 44 ground records. The median IDA curves of the 44 ground records were used for parametric study described in the next section. The same procedure was followed for the development of *Sa* vs hysteretic energy curves (**Figure 2.6**b). The hysteretic energy is calculated by the sum of the areas in hysteresis loops at each ground motion intensity and the last point of each curve in **Figure 2.6**b represents the hysteresis energy dissipated at the near-collapse stage.

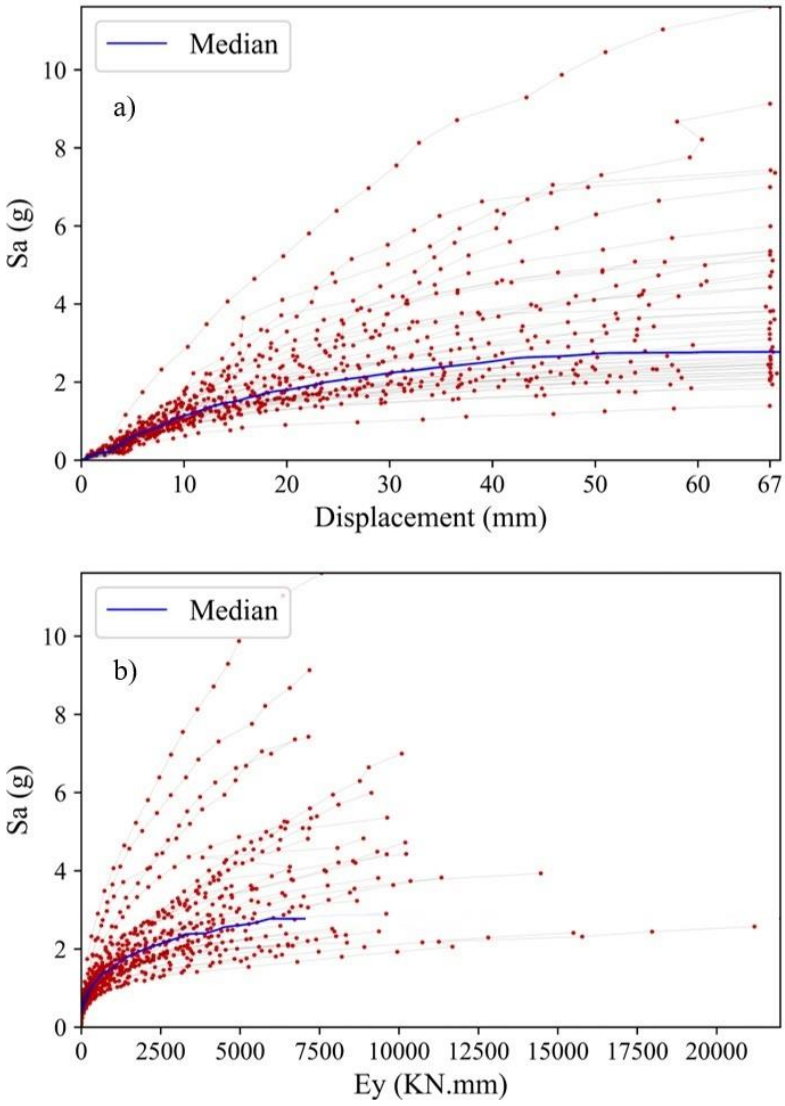

Figure 2.6. IDA curves of model S1 with period of 0.2 s: (a) *Sa* vs Displacement; and (b) *Sa* vs *Ey*.

2.5 Results

Figure 2.7 presents the examples of median IDA curves (*Sa* vs displacement) for the six models with periods of 0.2 s, 0.4 s, 0.7 s and 2 s. At the early stage of IDA curves when *Sa* is relatively small, the difference among all models is limited. When *Sa* are large enough, the EPP curve starts to deviate significantly from the pinched models for low period structures (0.2 s and 0.4 s), but almost shows no difference among models for medium and long period structures (0.7 s and 2 s).

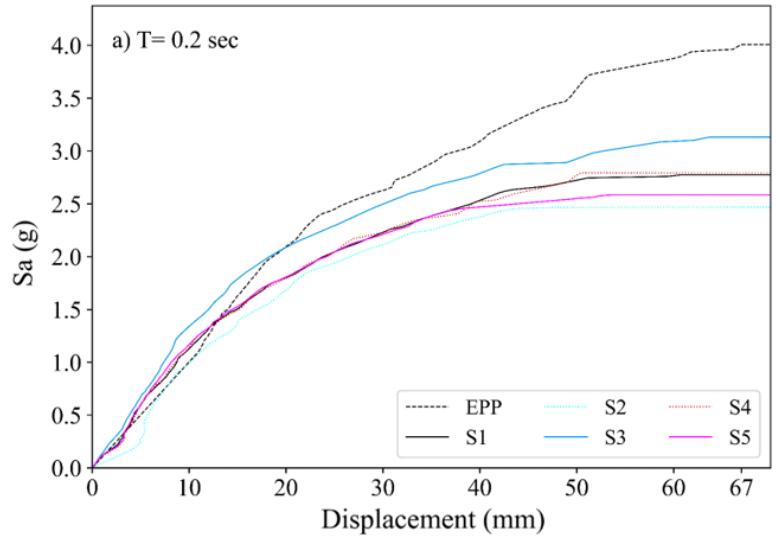
a) T= 0.2 sec
Sa (g)
Displacement (mm)
EPP
S1
S2
S3
S4
S5

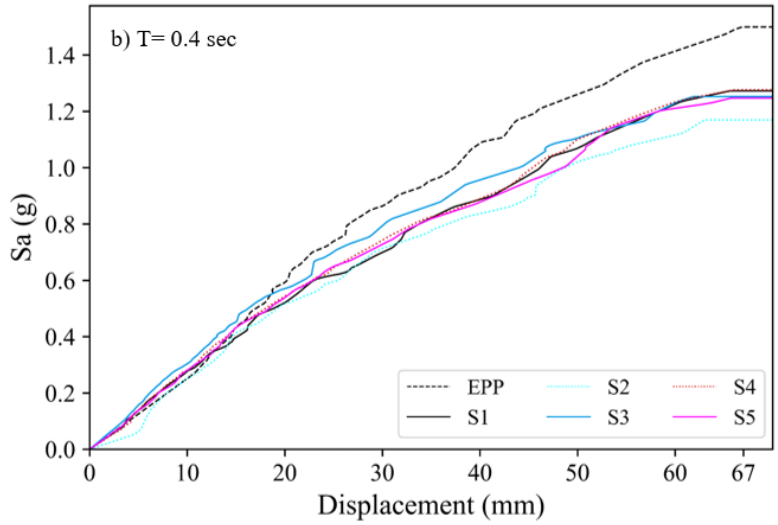
b) T= 0.4 sec
Sa (g)
Displacement (mm)
EPP
S1
S2
S3
S4
S5

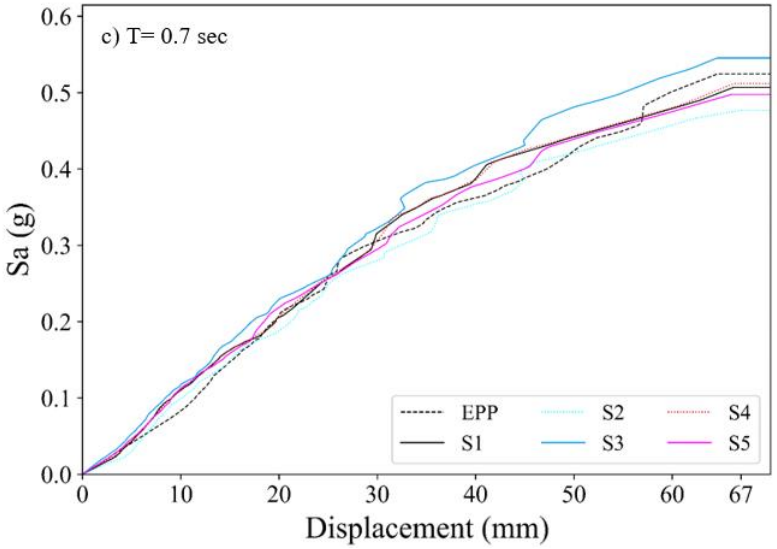
c) T= 0.7 sec
Sa (g)
Displacement (mm)
EPP
S1
S2
S3
S4
S5

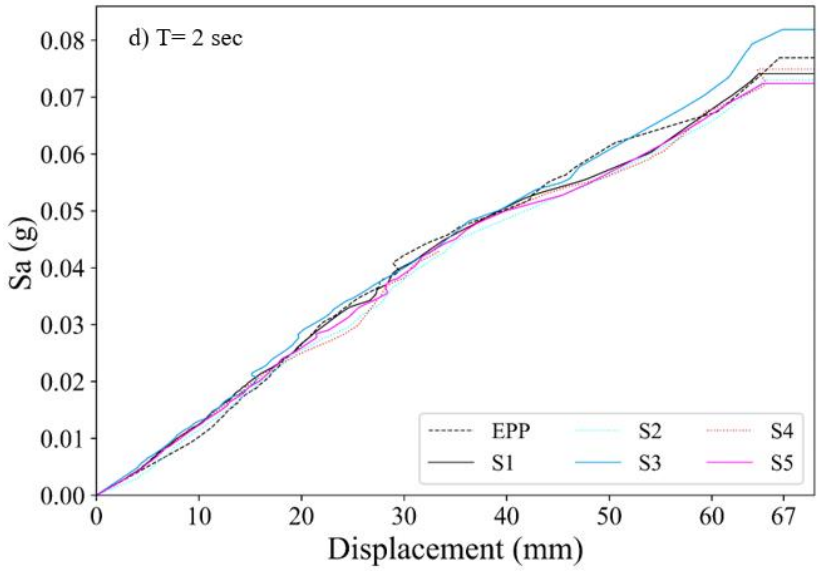

Figure 2.7. Median IDA curves (*Sa* vs Displacement) of models: (a) T = 0.2 s; (b) T = 0.4 s; (c) T = 0.7 s; and (d) T = 2 s.

Generally, for long period structures (2.0 s), the IDA curves (*Sa* vs displacement) are almost linear, which means these SDOF plastic systems have similar ultimate displacement compared to their corresponding elastic systems (**Figure 2.8**), which is consistent with the R-μ equations proposed by Newmark [49] that for long period structures, R factor equals to ductility ratio, μ. While for short period structure (0.2 s), the slope of the curves decreases when displacement increases (**Figure 2.7** a), which indicates the ultimate displacement of these systems is larger than their corresponding elastic systems (**Figure 2.8**).

Appendix A contains additional IDA curves of the SDOF systems that are not presented in this chapter.

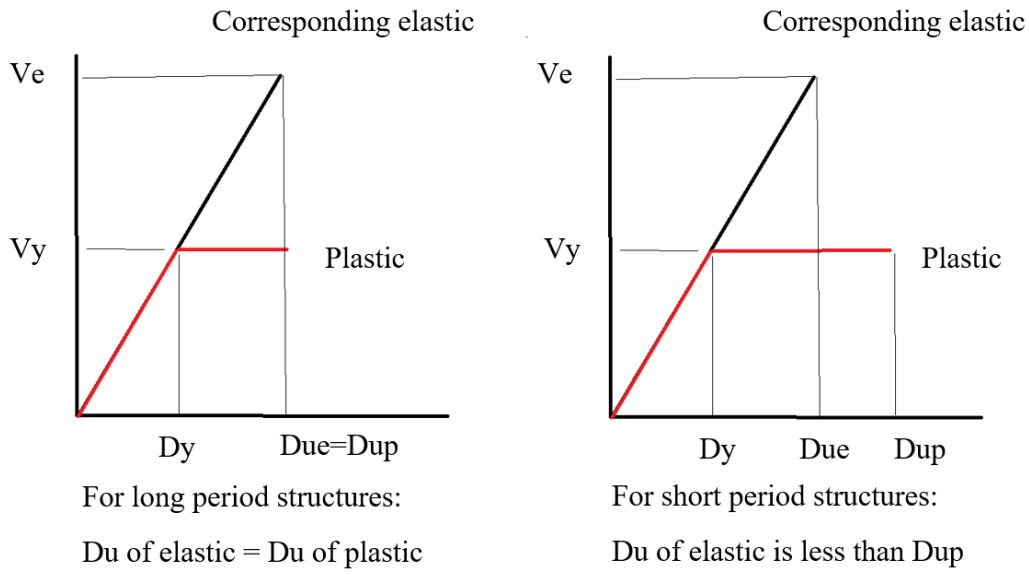

Figure 2.8. Elastic-perfectly-plastic model and its corresponding elastic system

Table 2.3 lists the median values of *Sa* of all 72 cases at near-collapse stage. **Figure 2.9** shows the normalized spectral accelerations of models based on the values of reference case, S1. **Figure 2.9** and **Table 2.3** show that in most cases of pinching models, S3 with larger residual strength has higher seismic capacity and S2 with smaller residual strength has lower capacity compared to the reference case S1. Although there's no clear trends on the relative difference, the absolute difference of *Sa* at near-collapse stage was more obvious for short period structures. For long period structures such as the ones with period of 2 s, the absolute difference between models is limited. For the effect of pinching stiffness, generally, S4 with smaller pinching stiffness has relatively larger ultimate seismic capacity and S5 with larger pinching stiffness has relatively smaller capacity. The difference among S4, S5 and S1 is much smaller than that among S3, S2 and S1.

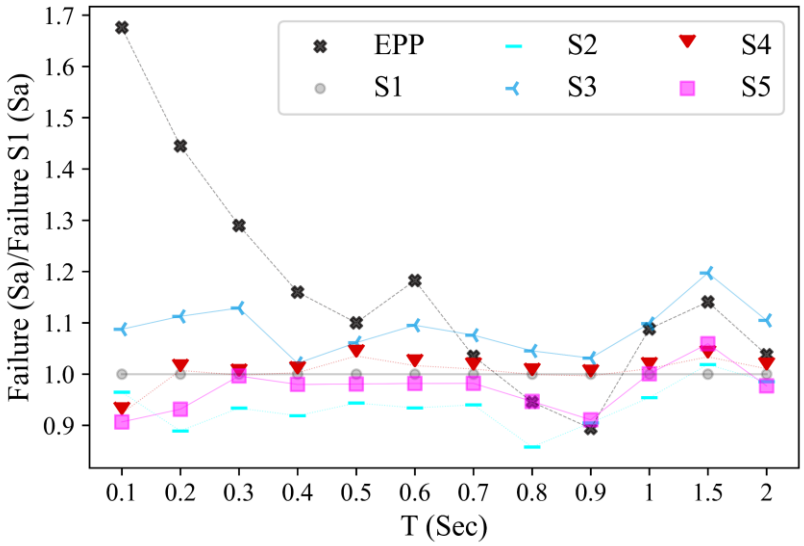

Figure 2.9. Ratio of *Sa* at the near-collapse stage (S1 as reference case).

Table 2.3. Median spectral acceleration (*Sa*(g)) at near-collapse stage.

Period (s)	EPP	S1	S2	S3	S4	S5
0.1	8.814 (68%*)	5.26	5.075 (-3.5%)	5.719 (8.7%)	4.856 (-7.7%)	4.769 (-9.3%)
0.2	4.007 (45%)	2.773	2.466 (-11%)	3.085 (11%)	2.793 (0.72%)	2.583 (-6.9%)
0.3	2.330 (29%)	1.806	1.687 (-6.6%)	2.039 (13%)	1.803 (-0.21%)	1.800 (-0.38%)
0.4	1.476 (16%)	1.273	1.169 (-8.1%)	1.299 (2.1%)	1.276 (0.23%)	1.247 (-2.0%)
0.5	1.066 (10%)	0.969	0.914 (-5.6%)	1.028 (6.1%)	1.003 (3.5%)	0.950 (-1.9%)
0.6	0.804 (18%)	0.680	0.635 (-6.6%)	0.745 (9.5%)	0.691 (1.6%)	0.667 (-1.8%)
0.7	0.525 (3.5%)	0.507	0.476 (-6.0%)	0.545 (7.6%)	0.512 (1.0%)	0.498 (-1.8%)
0.8	0.403 (-5.4%)	0.426	0.365 (-14%)	0.445 (4.5%)	0.426 (-0.07%)	0.403 (-5.3%)
0.9	0.341 (-11%)	0.382	0.346 (-9.5%)	0.394 (3.1%)	0.381 (-0.26%)	0.348 (-8.9%)
1	0.281 (8.8%)	0.258	0.246 (-4.6%)	0.283 (9.9%)	0.261 (1.1%)	0.258 (0.05%)
1.5	0.148 (14%)	0.130	0.132 (1.9%)	0.155 (20%)	0.134 (3.4%)	0.137 (5.9%)
2	0.077 (3.8%)	0.074	0.073 (-1.5%)	0.082 (11%)	0.075 (1.0%)	0.072 (-2.3%)

*Difference to the S1 model.

In general, the order of seismic resistance of the pinched models is S3 > S4 > S1 > S5 > S2 (**Table 2.3**) which agrees well with the order of the energy dissipation capacity of the five models under standard loading protocol (**Table 2.2**). EEP model has the highest seismic resistance compared to pinched models for short period structures less than 0.7 s. Beyond 0.7 s, the advantages of EEP model are not significant.

The IDA curves based on cumulative yielding energy (*Ey*) are presented in **Figure 2.10** for the six models with periods of 0.2 s, 0.4 s, 0.7 s and 2 s. It shows that at the same intensity of ground motions, *Sa*, EPP model dissipates less *Ey* than the pinched models for 0.2 s structures, while it dissipates more *Ey* for 2 s structures. For structures with periods within the two extreme cases (**Figure 2.10**b and c), the difference is limited.

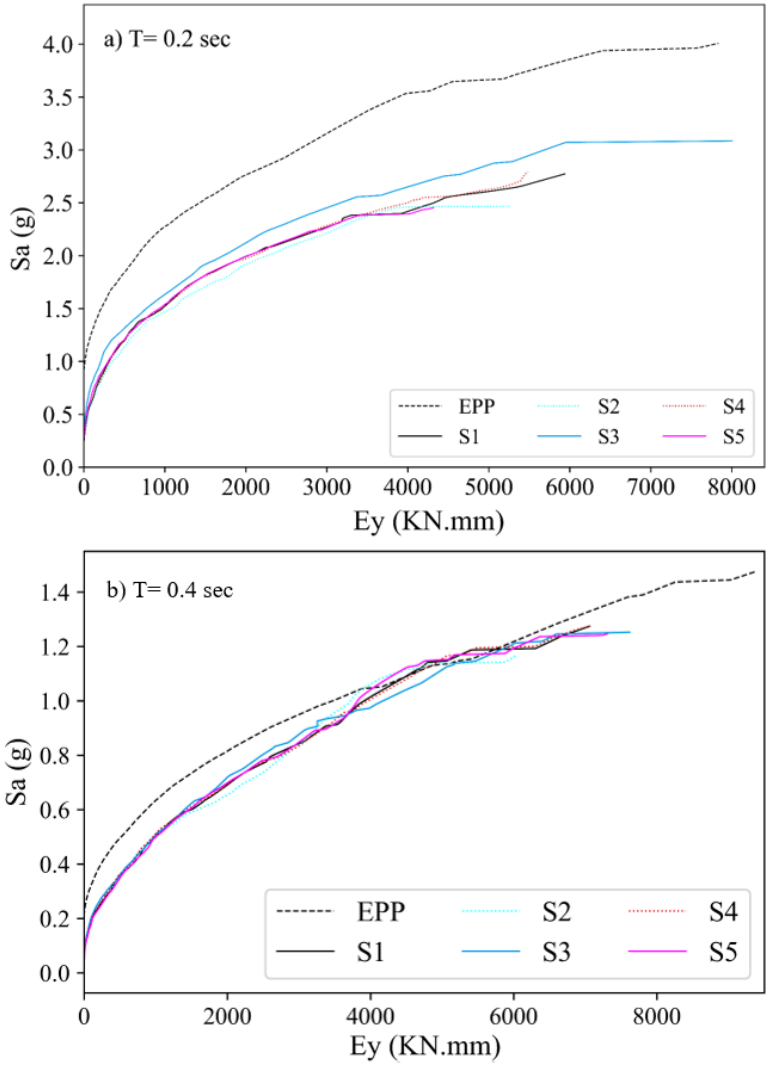

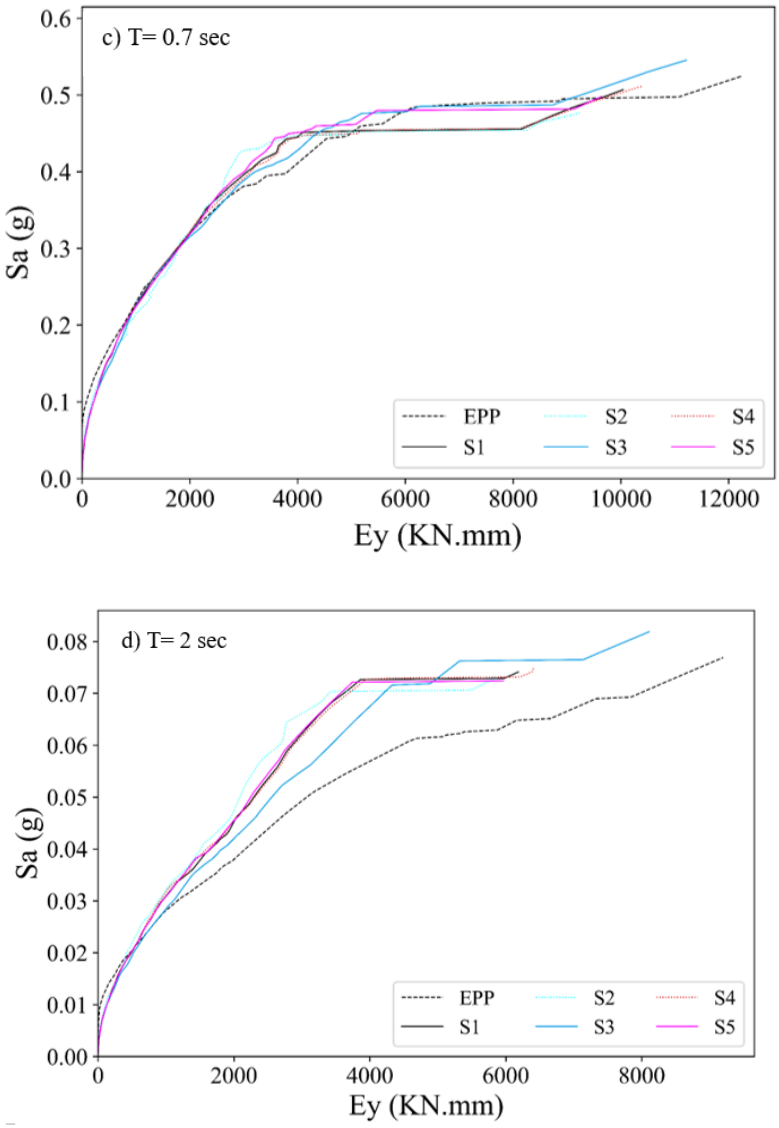

Figure 2.10. Median IDA curves (*Sa* vs *Ey*) of models: (a) T = 0.2 s; (b) T = 0.4 s; (c) T = 0.7 s; and (d) T = 2 s.

Table 2.4 lists the median values of *Ey* of all 72 cases at near-collapse stage. **Figure 2.11** shows the normalized hysteresis energy of models based on the values of S1. Generally, S2 has the lowest and S3 has the highest *Ey* within the pinched models, but the order (**Table 2.4**) is not always consistent with that of the seismic resistance (**Table 2.3**). The hysteresis energy dissipated under seismic events has no correlation with the periods of structures.

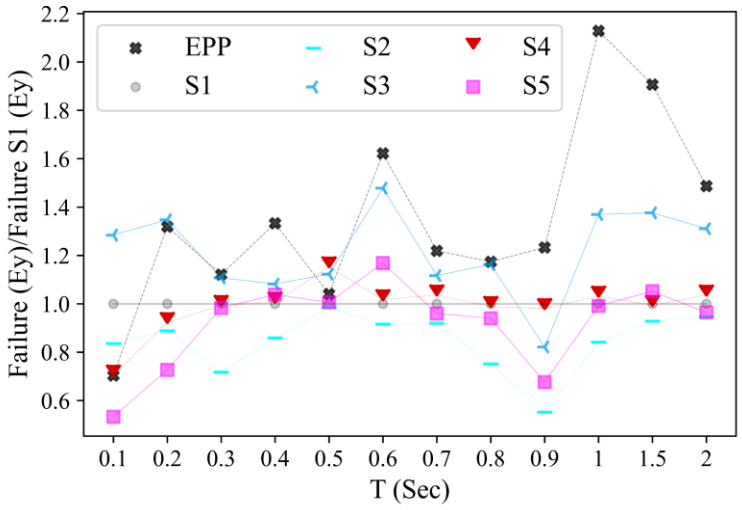

Figure 2.11. Ratio of *Ey* at the near-collapse stage (S1 as reference case)

Table 2.4. Median hysteretic energy (*Ey*) at near-collapse stage (kN.m)

Period (s)	EPP	S1	S2	S3	S4	S5
0.1	4.46 (-30%*)	6.33	5.29 (-17%)	8.13 (28%)	4.47 (-30%)	3.37 (-47%)
0.2	7.83 (32%)	5.94	5.28 (-11%)	8.00 (35%)	5.48 (-7.7%)	4.32 (-27%)
0.3	14.71 (12%)	13.12	9.42 (-28%)	14.53 (11%)	13.04 (-0.65%)	12.90 (-1.7%)
0.4	9.39 (33%)	7.04	6.05 (-14%)	7.62 (8.2%)	7.09 (0.63%)	7.31 (3.8%)
0.5	11.12 (4.0%)	10.69	10.54 (-1.4%)	12.00 (12%)	12.32 (15%)	10.75 (0.58%)
0.6	13.39 (62%)	8.26	7.56 (-8.4%)	12.21 (48%)	8.40 (1.7%)	9.65 (17%)
0.7	12.24 (22%)	10.04	9.23 (-8.0%)	11.21 (12%)	10.41 (3.7%)	9.64 (-4.0%)
0.8	11.06 (17%)	9.42	7.08 (-25%)	10.95 (16%)	9.31 (-1.1%)	8.86 (-6.0%)
0.9	13.40 (23%)	10.87	6.00 (-45%)	8.93 (-18%)	10.65 (-2.0%)	7.35 (-32%)
1	13.99 (113%)	6.57	5.53 (-16%)	9.00 (37%)	6.78 (3.2%)	6.52 (-0.89%)
1.5	11.03 (91%)	5.79	5.37 (-7.1%)	7.97 (38%)	5.75 (-0.63%)	6.09 (5.2%)
2	9.20 (49%)	6.18	5.86 (-5.3%)	8.11 (31%)	6.41 (3.6%)	5.96 (-3.6%)

*Difference to the S1 model.

2.6 Conclusion

In this project, the effect of pinching and energy dissipation capacity on seismic performance of timber structures was investigated through IDA analysis of 72 SDOF systems that covers three levels of pinching stiffness, three levels of residual strength, and 12 fundamental periods. The

seismic resistance represented by *Sa*, and the hysteresis energy, *Ey*, of SDOF systems were compared and discussed. The main study findings are summarized as follows:

- Pinching effect on seismic performance of timber structures is period-dependent. Short period structures are more sensitive to the pinching effect of hysteresis loops than long period structures.
- Higher residual strength of pinched model leads to higher seismic resistance, while higher pinching stiffness leads to lower seismic resistance. The effect of pinching stiffness on the seismic performance of timber structures is less than that of residual strength.
- A linear relationship between spectral acceleration and the maximum displacement of hysteresis models is observed in IDA curves until the near-collapse state for long period structures, while short period structures experience softening of IDA curves.
- The elastic-perfectly plastic model has much higher seismic capacity than pinched models for structures with periods less than 0.7 s. For longer period structures, the benefit of EEP model is not significant.
- For pinched models, increasing the hysteretic energy dissipation capacity of systems under standard loading protocols will increase the seismic capacity of the systems. For EEP model, the same conclusion is only valid for short period structures.
- The relationship between the seismic capacity, *Sa*, and the hysteretic energy, *Ey*, under seismic loads is not always consistent.

Chapter 3 Behavior of Self-Tapping Screws Used in Hybrid Light Wood-Frame Structures Connected to a CLT Core Wall

3.1 Introduction

Traditional light wood-frame buildings have proven to be a practical and sustainable solution for residential construction. The height limit of light wood-frame construction has been increased from four to six stories in the National Building Code of Canada (NBCC) [15]. With the increase in building height, these structures become more flexible and may have large lateral deformation under wind and seismic loads. As a result, the drift requirements may be hard to meet for the design of mid-rise light wood-frame buildings. Elevator shafts and stairwells commonly exist in multi-story buildings and can be used as part of the lateral load resisting system to reduce the lateral drift of the wood frame system. Cross-Laminated Timber (CLT) core has become more popular in multi-story light wood-frame buildings due to its fast construction compared with a reinforced concrete or masonry core. This core can provide the building with additional lateral load resistance, if sufficiently connected to the wood frame, and reduce the lateral deformation [50]. In this project, a hybrid system consisting of a light wood-frame structure connected to a CLT core was proposed. CLT cores are connected to light wood-frame structures on the floor level as shown in **Figure 3.1**a, where light wood-frame shear walls dissipate energy through deformation of the sheathing-to-framing nail joints [51], while CLT panels are rigid and rely on the panel-to-panel and panel-to-foundation connections to provide ductility [17]. Therefore, connections between the two sub-systems play an important role in the performance of the hybrid structure and can be used as one source of energy dissipation for seismic design if ductile performance is achieved through detailed

design. In this project, self-tapping screws were used to transmit lateral loads between the two sub-systems.

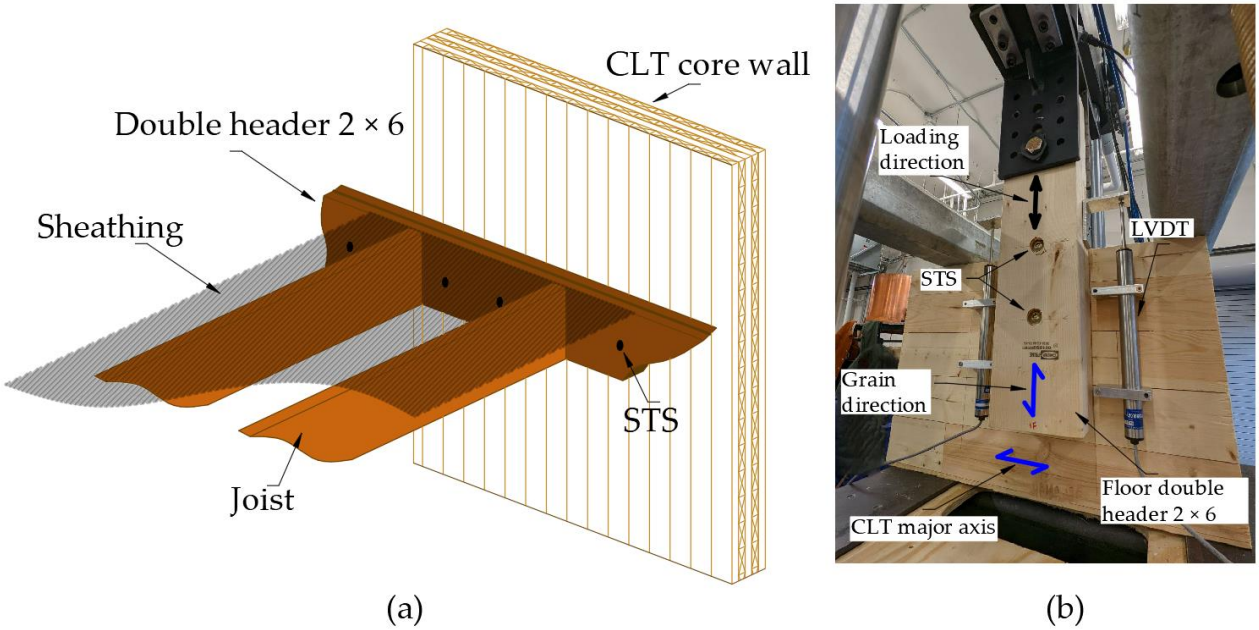

Figure 3.1. Self-tapping screw connections: (a) schematic of STS connections used in CLT and light wood-frame hybrid systems; and (b) test specimen setup.

Previous studies on CLT light wood-frame hybrid structures have been very limited. Nguyen et al. [52] tested a hybrid shear wall system consisting of light wood-frame shear wall segments and post-tensioned CLT panels. The CLT wall was connected to the studs of the light wood-frame shear wall using common nails. Test results showed that this hybrid wall system had high stiffness, energy dissipation, and a self-centering capability. Anandan et al. [53] conducted a full-scale shake table test on a one-story post-tensioned CLT building. Additional light wood-frame shear walls were connected to the CLT floor diaphragm through threaded steel rods. The hybrid system was tested under the 1994 Northridge earthquake, with a hazard level of 10% and a 2% probability of exceedance in 50 years, which corresponds to design-basis earthquake (DBE) and maximum

considered earthquake (MCE), respectively. Results showed that the system was able to recenter itself after shaking. The sheathing of the wood frame was marginally shifted after DBE excitation. The light wood-frame sustained moderate damage under MCE excitation.

Self-tapping screws (STSs) are commonly used in CLT construction [54]. With relatively higher capacity compared with dowel-type connections, STSs are very efficient in resisting lateral and axial loads for timber-to-timber connections [55]. There has been much research conducted on the STSs used in CLT structures. Munoz et al. [56] studied typical CLT floor-to-floor and wall-to-floor connections connected with STSs. Results showed that lap connections using STSs had better lateral capacity, stiffness, and ductility than spline configurations with normal wood screws. Hossain et al. [57] studied the performance of STS connections connecting 3-ply CLT panels under cyclic and monotonic loading. They found that STS connections with mixed angles had high stiffness and ductility. Tomasi et al. [58] also confirmed the superior performance of STSs installed with mixed angles in glued laminated timber joints. Gavric et al. [59] performed reversed-cyclic tests on different configurations of STS connections used in coupled CLT wall panels. They concluded that 90° STSs can achieve high ductility if sufficient spacing is provided. Brown et al. [60] investigated the behavior of STS joints between CLT panels with varying ratios of STSs installed inclined and at 90° to the timber grain. They found that a ratio of 2:1 yielded more efficient design. These studies were all focused on CLT-to-CLT or CLT-to glulam connections. There has been no investigation on CLT shear wall-to-light wood-frame floor, i.e., CLT-lumber connections connected with STSs. In this project, cyclic and monotonic tests were conducted on CLT-lumber STS connections inserted at 90°, 45° and mixed angles (90° and 45°) to assess the stiffness, load-carrying capacity, ductility, and energy dissipation capacity of these connections.

3.2 Test program

Figure 3.1a shows a schematic of the CLT-lumber connection. The CLT wall panel was directly connected to the floor headers of light wood-frame structures with STSs. **Figure 3.1**b shows the test setup of the connection specimen. Five-layer CLT panels with a thickness of 175 mm were used in this project. The panel had an E1 stress grade according to ANSI/APA PRG 320 [61] and was made of Spruce-Pine-Fir (SPF) machine stress rated lumber in longitudinal layers and No. 3/Stud SPF lumber in transverse layers [62]. **Table 3.1** shows the mechanical properties of E1 stress grade CLT panels cited from ANSI/APA PRG 320 [61] as no material tests were performed in this project. Three types of connection configurations with different STS insertion angles were studied, i.e., STS inserted at 90° (**Figure 3.2**a), 45° (**Figure 3.2**b), and mixed angles (90° and 45°) (**Figure 3.2**c) to the grain of the lumber (hereafter named 90° STS, 45° STS, and mixed angle STS). Two diameters of ASSY® SK and VG CSK STSs made from carbon steel (8 and 10 mm) were tested (**Figure 3.2**d). The mechanical properties of STSs cited from the CCMC report [63] are listed in **Table 3.1**. The 90° STS loaded in shear was partially threaded (PT) and 160 mm long, and the 45° STS loaded in both shear and withdrawal was fully threaded (FT) and 240 mm long. The floor header was composed of double 2 × 6 SPF lumber. For the 90° STS or 45° STS connections, each specimen had 2 screws. The mixed angle (90° and 45°) connection had two screws installed at 45° and the other two installed at 90°. Screws penetrated around two and a half layers into the CLT panel for all cases. Initially, 10d (d = 10 mm) was used as the screw spacing and end distance for both diameter screws. However, with the splitting of lumber in two replicates of STS connections with 10 mm diameter screws inserted at 90° under monotonic load, it was decided that 12d and 15d (d = 10 mm) be used for screw spacing and end distance, respectively, according to the MTC Solution Handbook [64].

Table 3.1. Material properties.

Cross-laminated timber [61]	**Layers**	
	Longitudinal	Transversal
Bending at extreme fibre, f_b (MPa)	28.2	7.0
Longitudinal shear, f_v (MPa)	1.5	1.5
Rolling shear, f_s (MPa)	0.5	0.5
Compression parallel to grain, f_c (MPa)	19.3	9.0
Compression perpendicular to grain, f_{cp} (MPa)	5.3	5.3
Tension parallel to grain, f_t (MPa)	15.4	3.2
Modulus of elasticity, E (MPa)	11700	9000
Shear modulus, G (MPa)	731	563
Longitudinal shear, f_v (MPa)	73.1	56.3
Self-tapping screw [63]	**Diameter**	
	8 mm	10 mm
Bending yield strength (MPa)	1015	942
Unfactored tension strength (kN)	18.9	24
Unfactored shear strength (kN)	641	691

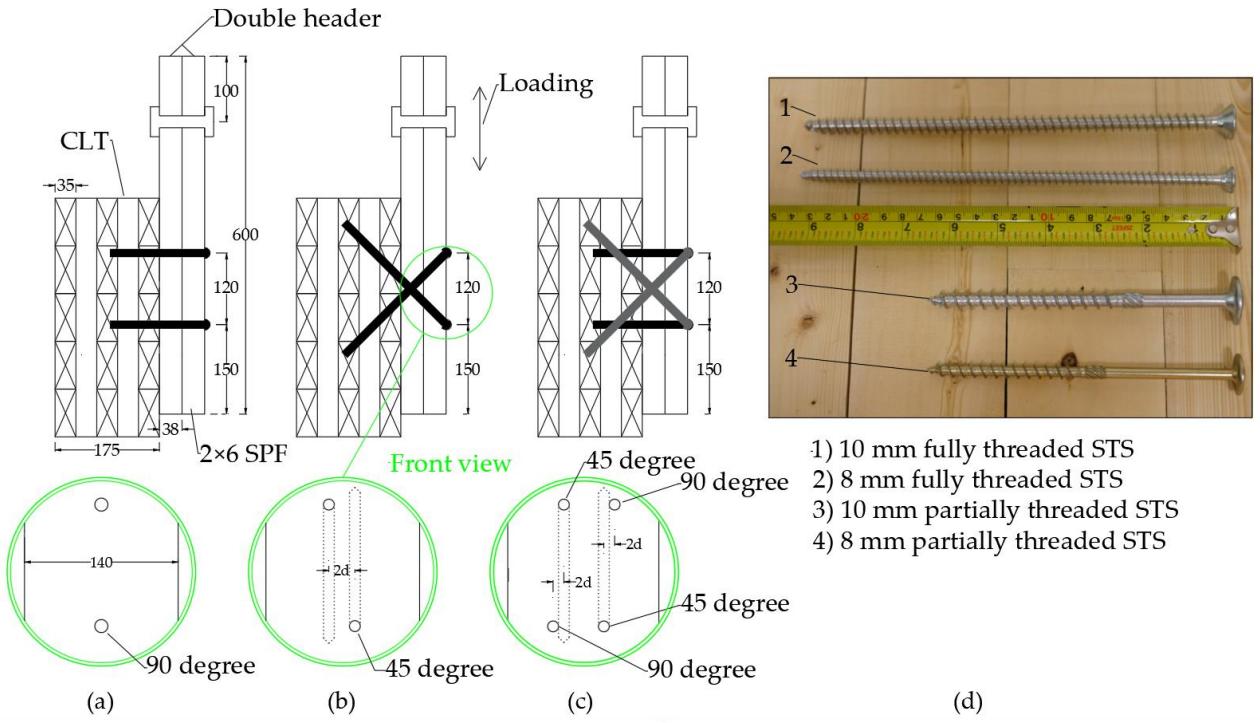

Figure 3.2. STS connection configurations (mm): (a) 90° STS; (b) 45° STS; (c) mixed angle (45° + 90°) STS; and (d) self-tapping screws.

In the proposed hybrid system, lateral forces were assumed to be transferred between the CLT core and floor header through the STSs. Cyclic and monotonic loadings were applied parallel to the grain of the lumber (**Figure 3.1**b). A summary of tested series is provided in **Table 3.2**. Four replicates were tested for each configuration, and there were 48 specimens tested in total. According to ASTM D1761-20 [65], the speed of the monotonic and cyclic test was set to 0.05 and 2 mm/s, respectively. Test method C (CUREE) [66] was used to define the loading protocol of the reversed-cyclic tests. The reference deformation of the CUREE protocol was derived based on monotonic test results, which were 3.6 and 30 mm for the 45° and 90° STS connection test, respectively. To measure the relative displacement between lumber and the CLT panel, two Linear Variable Differential Transformers (LVDTs) were attached to both sides of the lumber, as shown in **Figure 3.1**b. Prior to testing, lumbers were conditioned in an environmental room with 20° C and 65% relative humidity until they reached equilibrium moisture content (EMC). Lumber with relative density within 0.4 ± 0.04 were used in this project.

Table 3.2. Test matrix.

Loading type	STS insertion angle	STS type	Diameter of fasteners (mm)	Length of fasteners (mm)
Monotonic	90°	PT[1]	8	160
			10	160
	45°	FT[2]	8	240
			10	240
	45° + 90°	PT + FT	8	160 + 240
			10	160 + 240
Cyclic	90°	PT	8	160
			10	160
	45°	FT	8	240
			10	240
	45° + 90°	PT + FT	8	160 + 240
			10	160 + 240

Notes: [1]: partially threaded. [2]: fully threaded.

3.3 Experimental results

Displacement from both LVDTs was averaged. Data was recorded at a frequency of 10 and 100 Hz for the monotonic and cyclic tests, respectively. An example of cyclic load-deformation curves is shown in **Figure 3.3**a–c. It can be seen that both 90° STS and mixed angle STS connections achieved large displacement at around 30 mm without significant reduction in resistance, while the 45° STS connection had higher resistance compared with the 90° STS but failed at much smaller displacement. **Figure 3.3**d and e show comparisons of individual backbone curves for each connection configuration and the superposition of 45° STS and 90° STS curves under cyclic and monotonic load, respectively. It can be seen that the shape of the superposition curve and mixed angle connection curve were similar, which indicates that in the mixed angle connection, 45° STSs mostly contribute to the initial stiffness and 90° STSs mainly contribute to the ultimate displacement. There was a clear drop-down phase of the curve in the mixed angle connection when the 45° STSs withdrew from the CLT panel. After that, the resistance recovered and further increased when the 90° STSs contributed more resistance due to redistribution of the load between the two groups of fasteners.

Appendix B shows the loading protocol and hysteretic loops of the cyclic experiments conducted.

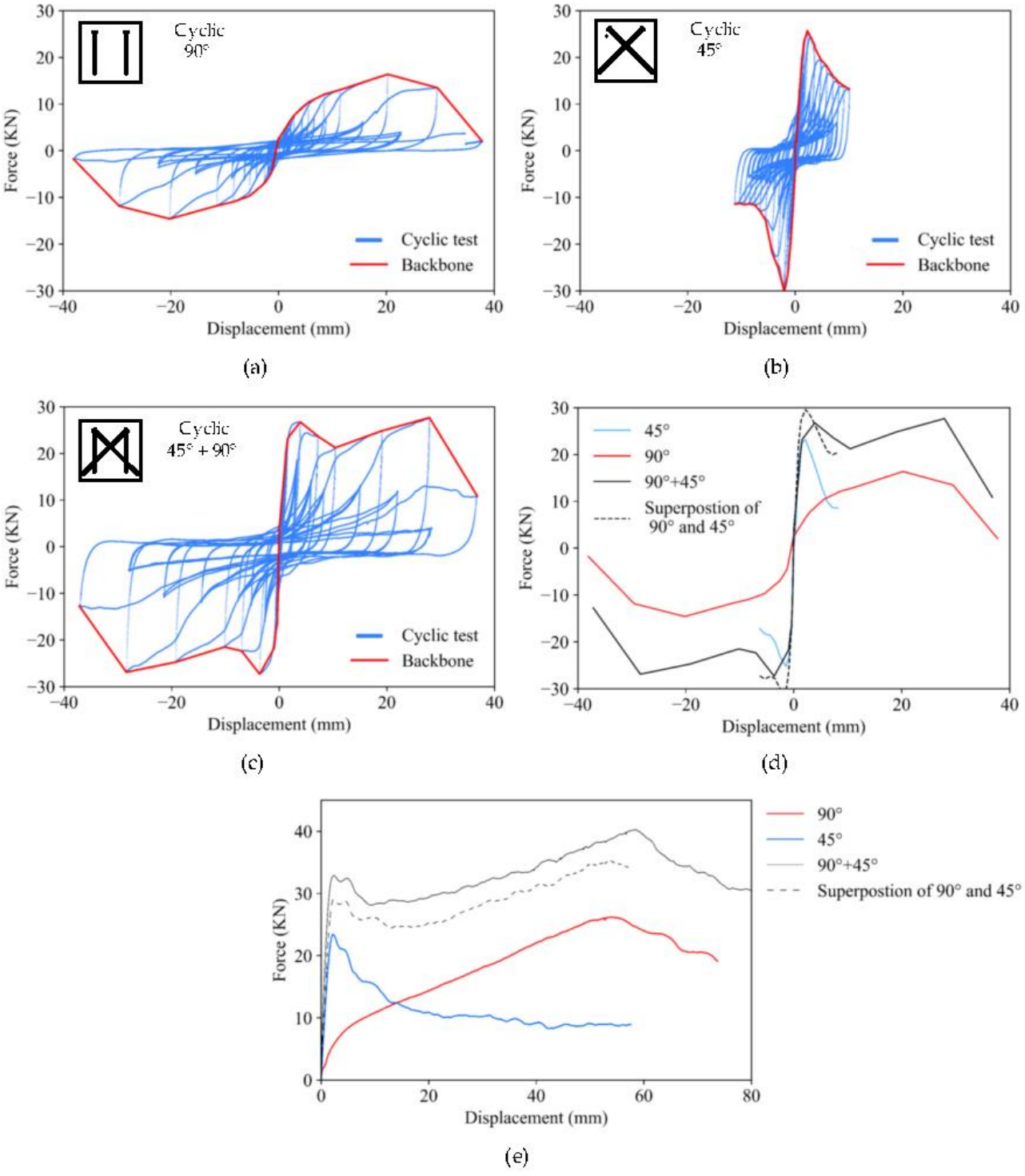

Figure 3.3. Load-displacement curves for 8 mm STSs (single replicate data): (a) 90° STS; (b) 45° STS; (c) mixed angle STS; (d) cyclic backbone curves; and (e) monotonic curves.

The positive and negative backbones of the cyclic tests were averaged. All the averaged backbone and monotonic curves of tests with their associated failure points are shown in **Figure 3.4**. Failure was defined when the load dropped to 80% of the maximum resistance. In the case of the mixed angle connections, failure was defined after the second peak load when the 90° STSs also lost their resistance. Although in some cases there was a 20% drop-down after the first peak when the 45° STSs lost their resistance, the overall resistance of the mixed angle connections was recovered due to redistribution of forces between the two groups of fasteners. The drop-down amount after the first peak can be optimized by adjusting the ratio of 45° STSs over 90° STSs [13]. As shown in **Figure 3.4**, two specimens of 10 mm STSs inserted at 90° under monotonic load (10d screw spacing, 10d end distance, and 7d edge distance) and one specimen of 10 mm STS inserted at 90° under cyclic load (12d screw spacing, 15d end distance, and 7d edge distance) failed at much smaller ultimate displacement than the other replicates. One specimen of 8 mm STS inserted at mixed angles under monotonic load (12d screw spacing, 15d end distance, and 3d edge distance) failed at a slightly smaller displacement than the other replicates. These failures happened because of splitting in the lumber (**Figure 3.5**d and e). In the other cases, wood only showed localized crushing around the STSs (**Figure 3.5**a–c). Therefore, connections with lumber splitting showed a less ductile behavior compared with the other replicates. With larger end distances or predrilling, this failure may be prevented. In general, 10 mm STS connections have higher resistance and are more prone to splitting wood than 8 mm STS connections. Mixed angle and 90° STS connections failed at much smaller displacement under cyclic load compared to those under monotonic load; however, there was not much difference for 45° STS connections.

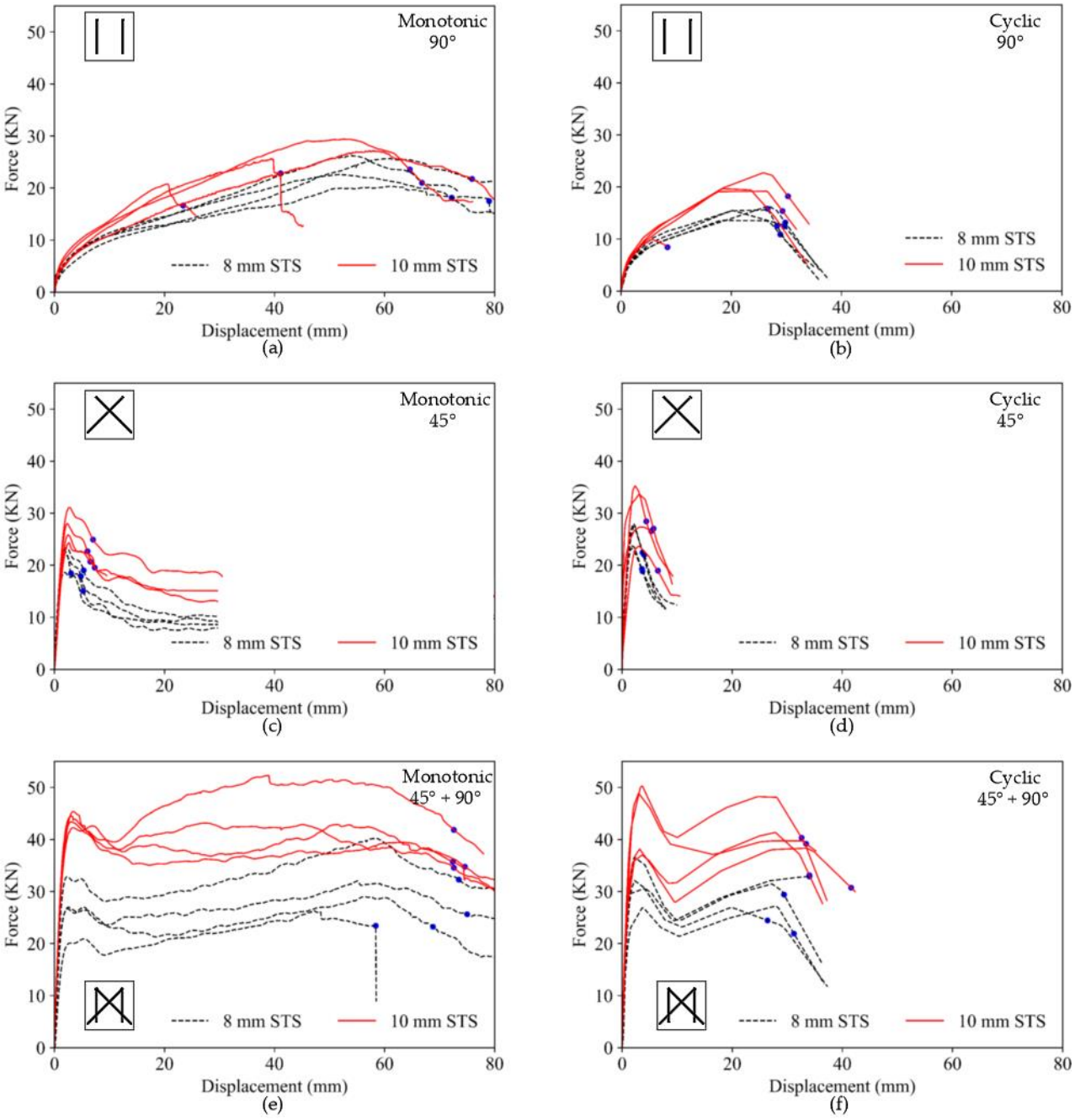

Figure 3.4. Cyclic backbones and monotonic curves of STS connections: (a) 90° STS under monotonic; (b) 90° STS under cyclic; (c) 45° STS under monotonic; (d) 45° STS under cyclic; (e) mixed angle (45° + 90°) STS under monotonic; and (f) mixed angle (45° + 90°) STS under cyclic. **Notes:** Failure points are marked with dots at 80% of maximum load on the descending phase.

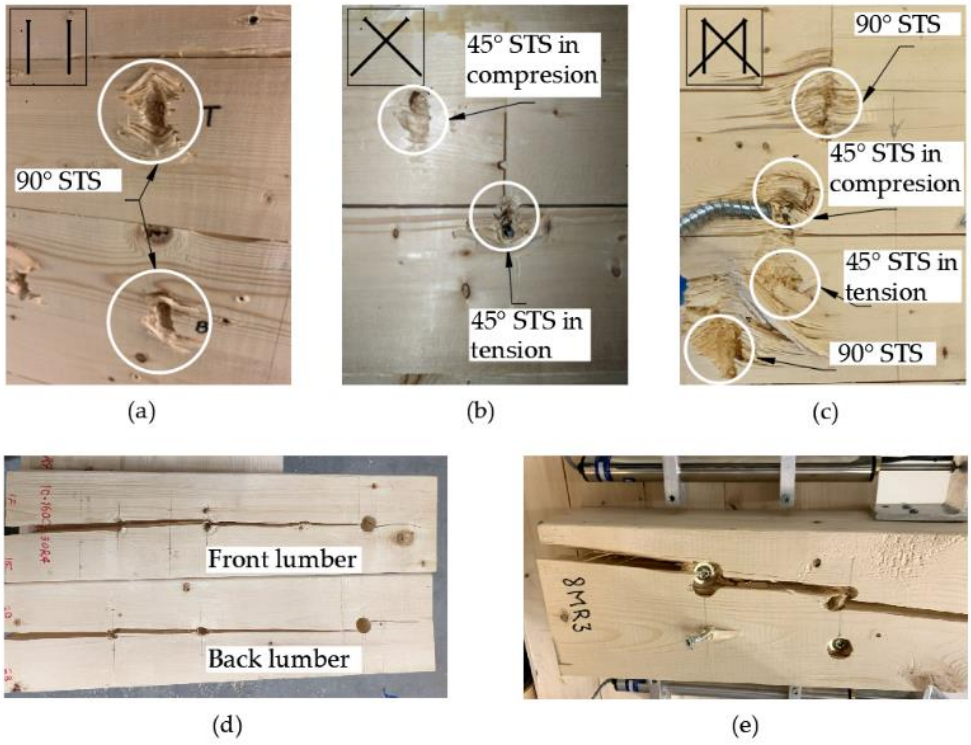

Figure 3.5. Failure on wood: (a) wood crush in 90° STS; (b) wood crush in 45° STS; (c) wood crush in mixed angle connection (90° + 45°); (d) wood splitting in 10 mm connection with STS installed at 90°; and (e) wood splitting in 8 mm connection with STS installed at mixed angles.

Using the Equivalent Energy Elastic-Plastic [66] method, the mechanical properties of CLT-lumber STS connections were obtained. The ultimate displacement was defined as the displacement at 80% of the maximum load on the descending phase (after the second peak in the case of mixed angle connections) (**Figure 3.4**) [66]. The mean and coefficient of variation (COV) of these properties were: yield force (F_y) and its corresponding yield displacement (Δ_y), peak force (F_{peak}) and its corresponding displacement (Δ_{peak}), ultimate displacement (Δ_u), stiffness (K), ductility (μ), and energy dissipation (E). These are presented in **Table 3.3** and **Table 3.4** for monotonic and cyclic loading. Comparison of the mean values of these mechanical properties is shown in **Figure 3.6**. Specimens with STSs installed at 90° had larger ultimate displacement (around 70 mm under monotonic load and 30 mm under cyclic load) than that of STSs inserted at 45° (around 5 mm under

both monotonic and cyclic loads). Interestingly, although the 90° STS connections had much larger ultimate displacement, the ductility was similar to that of the 45° STS connections (ranging from 3.8 to 5.6). This is because the 45° STS is much stiffer than the 90° STS, so the yield displacement of STSs inserted at 45° (around 1.1 mm under both monotonic and cyclic loads) was much smaller than STSs inserted at 90° (around 17 mm under monotonic and 6 mm under cyclic load). Therefore, the ratio of ultimate displacement to yield displacement (i.e., ductility value) was similar for these two groups of connections. It is worth mentioning this conclusion is dependent on the definition of the ductility and the methods to drive the yielding point. Since the yield point for the 45° STSs based on the EEEP method in ASTM E2126 [66] is only around 1.1 mm, defining the ductility as a ratio to the yielding displacement introduces a similar ductility value as that of 90° STS connections variation. Despite having similar ductility ratio, 90° STS connections have higher energy dissipation capacity than that of 45° STS connections (more than six times under monotonic load and 1.9 times under cyclic load). There has been much discussion on the definition of ductility, however achieving a universally accepted quantitative definition remains challenging. To classify the connection in this context, the deformation capacity was also considered an indicator. Therefore, the 45° STS connection was classified as non-ductile connection due to very small ultimate deformation (around 5 mm). For the mixed angle STS (45° and 90°) connections, small yield displacement and large ultimate displacement are both presented. Accordingly, the ductility of the specimens with mixed angle connections greatly increased (around 56 under monotonic and 32 under cyclic load) compared with connections with 90° STSs or 45° STSs (ranging from 3.8 to 5.6). Mixed angle STS connections had an energy dissipation of more than 11 times the value of 45° STS connections. This effect was more pronounced in 8 mm STSs compared with 10 mm STS specimens. The 45° STS connection had on average more than 50% load-carrying capacity (52% for 10 mm STSs and 64% for 8 mm

STSs) compared with 90° STS under cyclic loading. However, it had relatively less capacity compared with 90° STS under monotonic loading. Connections with mixed 45° and 90° STSs had higher peak resistance compared with that with 90° STSs or 45° STSs only but less than the sum of the resistance of the two connections. This is because the 45° STSs and 90° STSs in the mixed angle connections did not reach their peak resistance at the same displacement. A transition of load sharing between 45° STSs and 90° STSs was observed in mixed angle connections.

Table 3.3. Mechanical properties of STS connections under monotonic loading.

Monotonic	Screw diameter	Δ_y (mm)	F_y (kN)	F_{peak} (kN)	Δ_{peak} (mm)	Δ_u (mm)	K (kN/mm)	μ	E^2 (kN·mm)
90°	8 mm	18.4	21.1	26.2	53.9	66.9	1.1	3.6	1217.5
		22.4	20.6	25.7	61.1	86.1	0.9	3.9	1542.9
		12.3	18.8	22.6	52.0	72.3	1.5	5.9	1243.6
		8.7	16.6	20.3	61.7	79.1	1.9	9.1	1240.9
	Mean	15.4	19.2	23.7	57.2	76.1	1.4	5.6	1311.2
	COV	34%	9%	10%	8%	10%	27%	39%	10%
45°	8 mm	0.9	20.6	22.9	1.7	3.1	23.9	3.6	54.6
		1.0	20.0	22.2	2.0	4.8	21.0	5.1	86.0
		1.3	21.2	23.4	2.2	5.4	16.0	4.1	100.7
		0.9	17.5	18.6	1.9	5.2	19.4	5.8	83.1
	Mean	1.0	19.8	21.8	1.9	4.6	20.1	4.6	81.1
	COV	18%	7%	9%	9%	20%	14%	19%	21%
45° + 90°	8 mm	1.12	24.9	29.0	56.5	68.8	22.2	61.5	1699.2
		1.18	27.6	32.0	55.2	75.0	23.3	63.4	2053.7
		1.63	22.1	26.3	47.4	58.5	13.5	35.9	1274.8
		1.17	33.4	40.2	58.4	73.6	28.5	62.9	2438.7
	Mean	1.28	27.0	31.9	54.4	69.0	21.9	55.9	1866.6
	COV	16%	16%	16%	8%	9%	25%	21%	23%
90°	10 mm	20.8	22.7	27.2	57.3	75.9	1.1	3.7	1486.9
		14.1[1]	21.1[1]	25.7[1]	39.3[1]	41.1[1]	1.5[1]	2.9[1]	718.5[1]
		5.6[1]	16.2[1]	20.8[1]	20.7[1]	23.3[1]	2.9[1]	4.2[1]	332.1[1]
		16.0	24.6	29.4	52.6	64.7	1.5	4.0	1394.8
	Mean	18.4	23.6	28.3	42.5	70.3	1.3	3.8	1440.8
	COV	13%	4%	4%	33%	8%	17%	5%	3%
45°	10 mm	1.4	25.4	28.0	2.3	6.1	17.5	4.2	137.2
		1.5	28.3	31.1	2.7	7.0	18.7	4.6	176.9
		1.5	23.0	25.8	2.5	6.5	15.2	4.3	132.3
		1.5	22.3	24.3	2.6	7.3	14.7	4.8	146.1
	Mean	1.5	24.8	27.3	2.5	6.7	16.5	4.5	148.1
	COV	2%	9%	9%	6%	7%	10%	5%	12%

45˚ + 90˚	10 mm	1.21	39.3	44.5	51.0	72.4	32.5	59.9	2821.5
		1.15	37.4	43.4	63.1	74.6	32.5	64.9	2768.5
		1.30	40.3	43.2	44.8	72.7	31.1	55.9	2903.6
		1.53	47.5	52.3	38.6	72.6	31.1	47.5	3412.2
	Mean	1.30	41.1	45.8	49.4	73.1	31.8	57.1	2976.5
	COV	11%	9%	8%	18%	1%	2%	11%	9%

Notes: [1] The specimen failed due to splitting of wood and its mechanical properties are not used in calculation of mean and COV.

[2] Energy dissipation under monotonic load is calculated to the failure point (Figure 4). The energy dissipation under cyclic load is calculated to the end of the first primary cycle that causes drop of the peak resistance below 80% of the maximum load. The two subsequent cycles with 75% amplitude are not included.

Table 3.4. Mechanical properties of STS connections under reversed-cyclic loading.

Cyclic	Screw diameter	Δ_y (mm)	F_y (kN)	F_{peak} (kN)	Δ_{peak} (mm)	Δ_u (mm)	K (kN/mm)	μ	E^2 (kN·mm)
90˚	8 mm	6.1	13.0	16.6	26.8	29.8	2.1	4.9	550.6
		4.2	11.8	14.4	26.2	28.3	2.8	6.7	495.8
		5.4	13.3	16.7	26.5	27.9	2.5	5.2	530.3
		4.4	13.0	15.5	20.2	29.7	3.0	6.8	520.6
	Mean	5.0	12.8	15.8	24.9	28.9	2.6	5.9	524.3
	COV	15%	4%	6%	11%	3%	13%	15%	4%
45˚	8 mm	1.0	21.5	23.9	2.5	4.3	21.9	4.4	174.8
		1.1	25.5	28.1	2.0	3.8	23.6	3.5	150.2
		1.2	24.9	27.8	2.2	3.9	20.5	3.2	174.1
		0.8	22.1	24.2	1.8	3.5	27.0	4.3	151.4
	Mean	1.0	23.5	26.0	2.1	3.9	23.2	3.9	162.6
	COV	14%	7%	8%	12%	7%	10%	13%	7%
45˚ + 90˚	8 mm	0.92	29.4	32.9	34.1	34.1	32.0	37.1	2214.5
		0.81	24.2	27.2	27.9	31.3	30.0	38.8	2184.1
		0.91	29.3	36.6	27.5	29.5	32.2	32.5	2411.4
		1.11	26.0	30.6	19.9	26.5	23.4	23.9	2409.2
	Mean	0.94	27.2	31.8	27.4	30.4	29.4	33.1	2304.8
	COV	12%	8%	11%	18%	9%	12%	17%	5%
90˚	10 mm	7.0	17.3	20.9	26.4	30.0	2.5	4.3	621.5
		8.3	18.6	23.0	25.8	30.3	2.2	3.7	663.4
		5.4	16.8	20.9	23.5	25.8	3.1	4.7	608.3
		1.8[1]	9.1[1]	10.4[1]	8.0[1]	9.0[1]	5.1[1]	5.2[1]	163.0[1]
	Mean	6.9	17.6	21.6	20.9	28.7	2.6	4.2	631.1
	COV	17%	4%	5%	36%	7%	13%	10%	4%
45˚	10 mm	1.5	31.8	35.7	2.3	4.8	21.9	3.3	250.0
		0.7	35.1	39.5	0.6	4.0	52.6	6.0	261.1
		0.9	28.8	32.2	1.0	5.8	32.9	6.6	300.0
		1.5	21.4	23.8	3.2	6.6	14.3	4.4	252.3
	Mean	1.1	29.3	32.8	1.8	5.3	30.4	5.1	265.8
	COV	32%	17%	18%	59%	18%	47%	26%	8%
45˚ + 90˚	10 mm	1.10	34.5	38.3	33.6	41.7	31.2	37.7	3052.6

	1.15	39.9	48.9	24.8	33.5	34.8	29.2	3252.6
	1.17	44.9	50.2	27.1	32.7	38.4	27.9	3326.7
	1.06	36.6	41.3	27.5	34.1	34.4	32.0	2614.9
Mean	1.12	39.0	44.7	28.2	35.5	34.7	31.7	3061.7
COV	4%	10%	11%	11%	10%	7%	12%	9%

Notes: [1] The specimen failed due to splitting of wood and its mechanical properties are not used in calculation of mean and COV.
[2] Energy dissipation under monotonic load is calculated to the failure point. The energy dissipation under cyclic load is calculated to the end of the first primary cycle that causes drop of the peak resistance below 80% of the maximum load. The two subsequent cycles with 75% amplitude are not included.

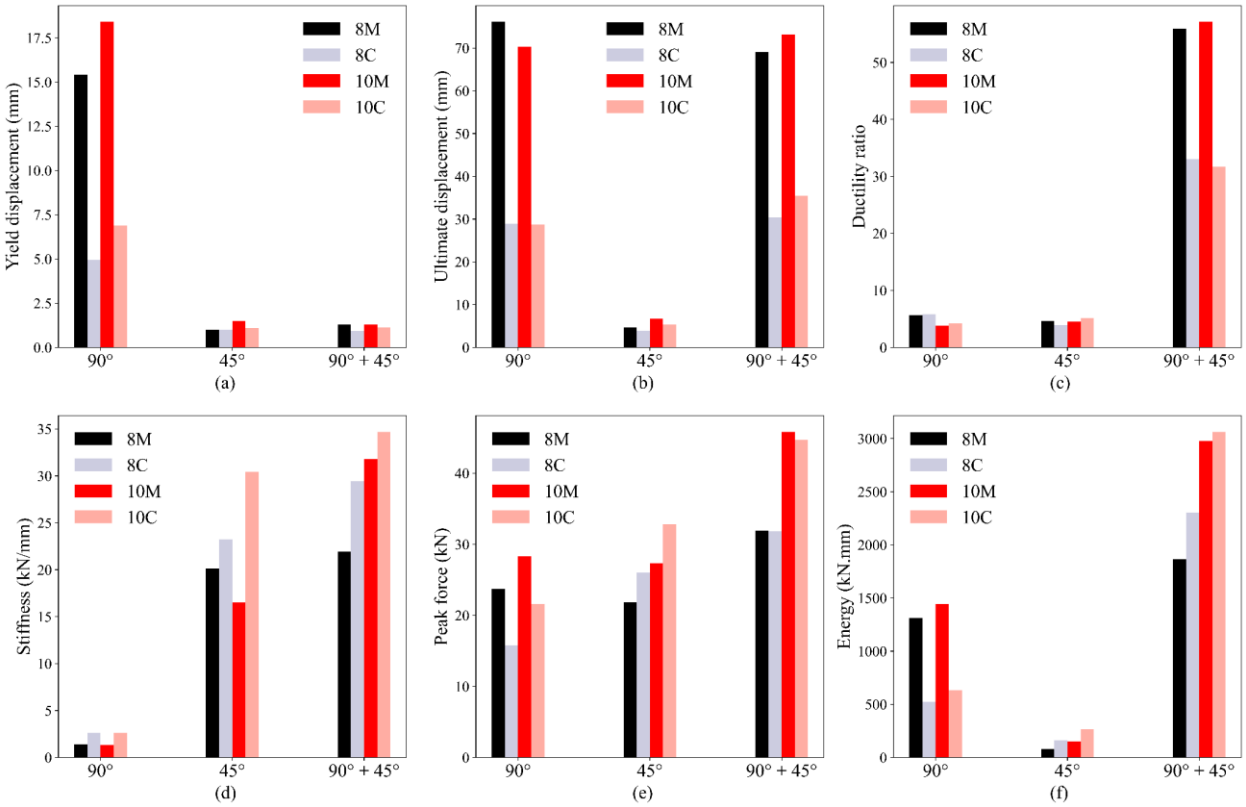

Figure 3.6. Comparison of average mechanical properties of STS connections: (a) yield displacement; (b) ultimate displacement; (c) ductility ratio; (d) stiffness; (e) peak force; and (f) energy.

There was a high variance in the stiffness of 10 mm STSs inserted at 45° under cyclic load (**Table 3.4**). This was due to the eccentric installation of STSs. There was a 2d offset (**Figure 3.2**b) between the two 45° STSs, which led to twisting in the lumber. **Figure 3.7** demonstrates the failure modes of self-tapping screws under monotonic and cyclic loads. All specimens with STSs inserted at 90°

showed two yielding points under monotonic loading, and all of them broke at these two points under cyclic loading. The breakage of 90° STSs under cyclic load was due to the cumulated damage in plastic deformation, which causes reduction of the ultimate displacement under cyclic load compared with that under monotonic load (**Table 3.3** and **Table 3.4**). In 45° STS connections under monotonic loading, one of the screws inserted at 45° broke due to a combination of compression and shear, and the other yielded in shear and was withdrawn. When loaded under reversed-cyclic load, all STSs inserted at 45° were slightly bent at two points. Therefore, the ultimate displacement of STSs inserted at 45° under cyclic load was similar to that under monotonic load (**Table 3.3** and **Table 3.4**). The failure of 45° STS because of the combination of compression and shear under monotonic load may have been due to buckling. Similarly, the 45° STSs in mixed angle connections remained unbroken and slightly bent, while the 90° STSs were broken under cyclic tests. Specimens with mixed angle STSs had the same failure modes as individual 45° STS and 90° STS connections under monotonic loading.

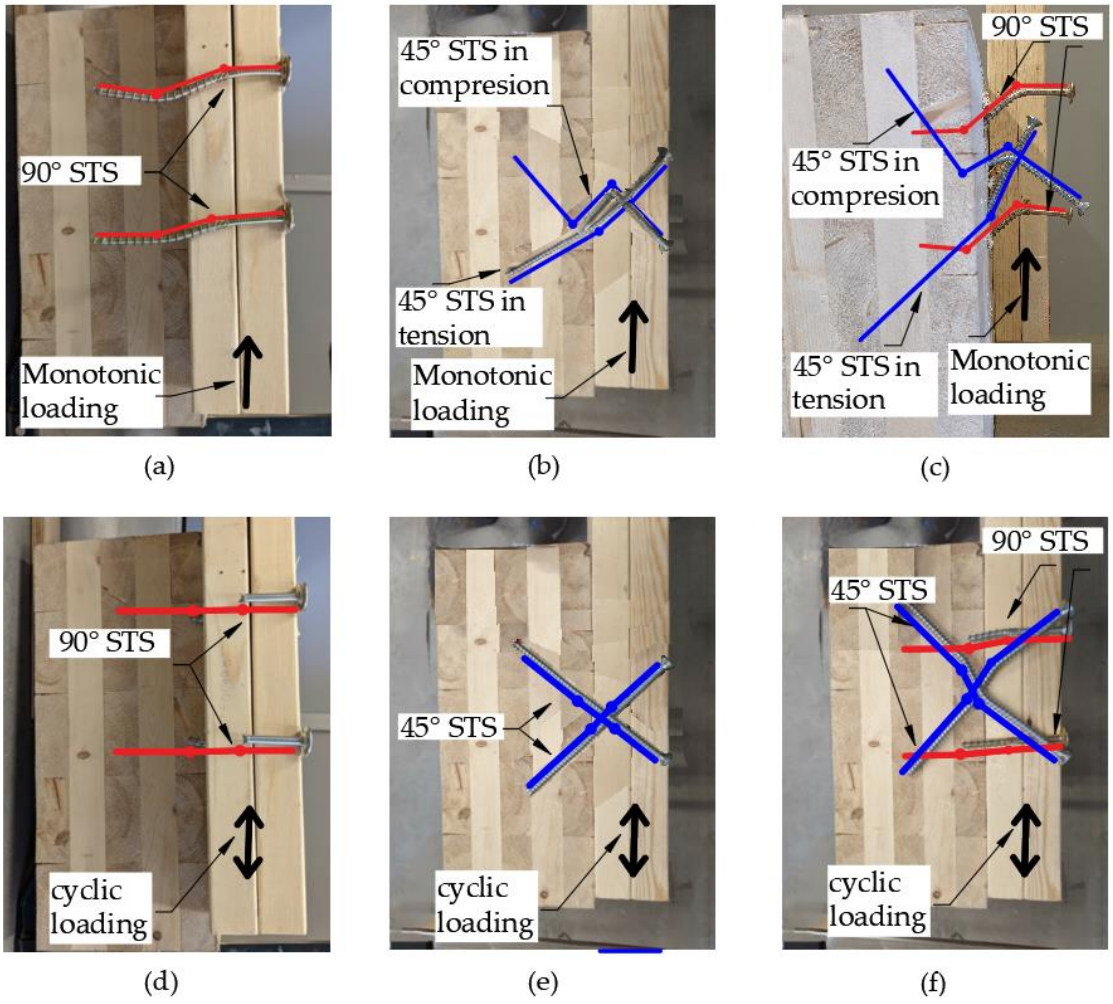

Figure 3.7. Failure modes of STSs in CLT-lumber connections: (a) 90° STS; (b) 45° STS; (c) mixed angle STS (45° and 90°); (d) STS at 90°; (e) STS at 45°; and (f) STS at mixed angles (90° and 45°).

The relationship between energy dissipation and ductility is not usually straightforward as revealed in Chapter 2 of this thesis. The total energy dissipation depends largely on the displacement history, i.e., the loading protocol. However, the ductility is sensitive to the yielding displacement or initial stiffness. Therefore, another parameter commonly used for evaluation of the energy dissipation capacity of a system, the equivalent viscous damping, is calculated for each cycle of the hysteresis loops using Equation (1) [67].

$$\zeta_{hyst} = \zeta_{eq.viscous} = \frac{A_{half-loop}}{\pi . F_{\max} . D_{\max}} \quad (1)$$

where $A_{half\text{-}loop}$ is half of the energy dissipated in each hysteresis loop. F_{max} and D_{max} are the maximum force and displacement of the same loop, respectively.

Equivalent viscous damping characterizes the energy dissipation due to plastic behavior. As shown in **Figure 3.8**, before yielding, the equivalent viscous damping was more than 10% for connections with 90° STSs, but for connections with 45° STSs and mixed angle connections, the equivalent viscous damping was smaller. At higher displacement, the equivalent viscous damping reached up to at least 20% for all configurations, which indicates good energy dissipation capacities of these connections. This conclusion seems neither consistent with what is derived based on ductility ratio nor energy dissipation. This is because the equivalent hysteretic damping is proportional to the energy dissipation normalized with the peak load and its corresponding displacement on each cycle (see Equation (1)), which is different from the value of total energy dissipation and ductility ratio. Further research should be carried out on the energy dissipation capacity of the three types of STS connections used in a hybrid CLT-light wood-frame structure through time history analysis.

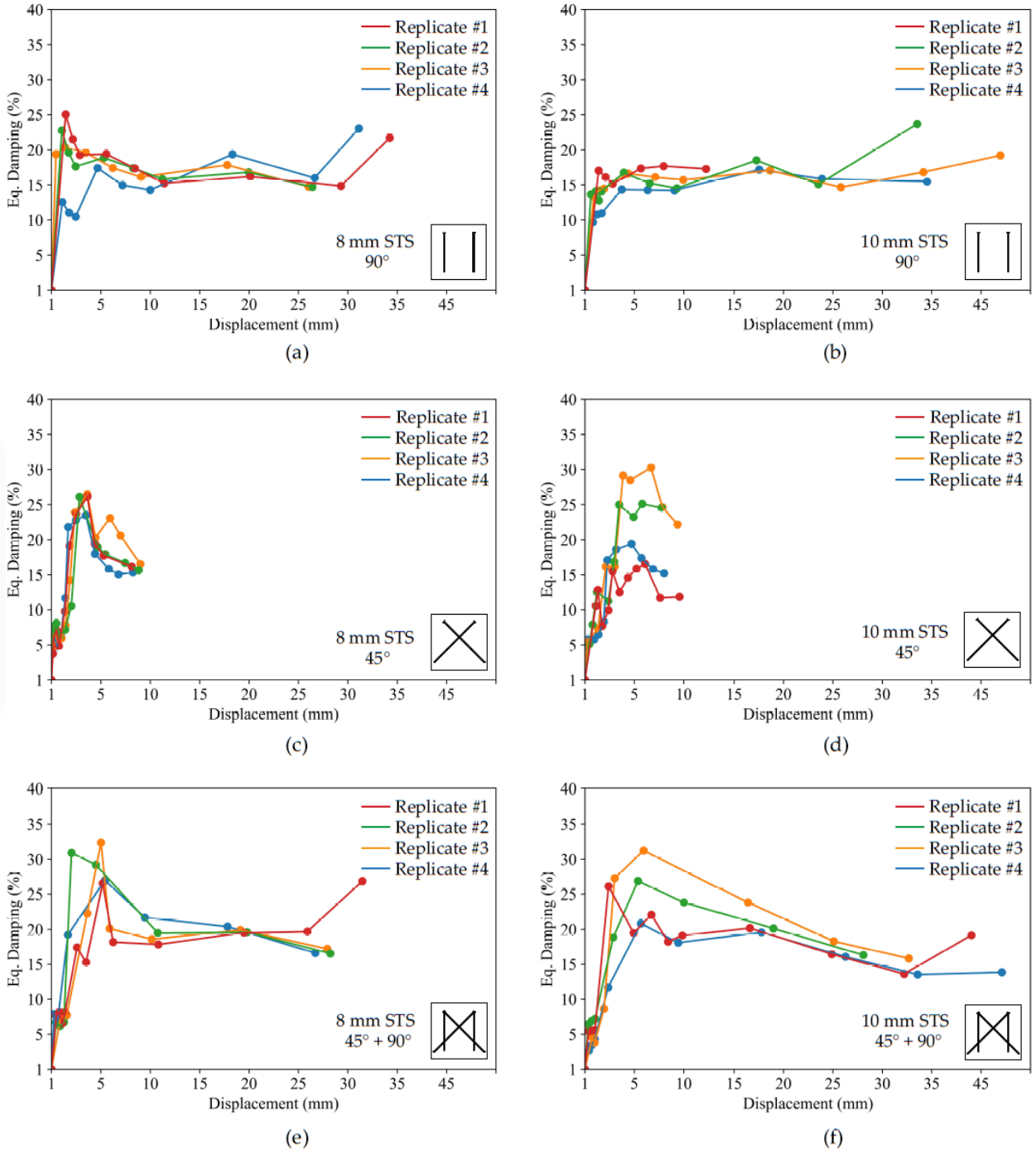

Figure 3.8. Equivalent viscous damping ratio of STS connections under reversed-cyclic loading: (a) 8 mm STS at 90°; (b) 10 mm STS at 90°; (c) 8 mm STS at 45°; (d) 10 mm STS at 45°; (e) 8 mm STS at mixed angles (45° and 90°); and (f) 10 mm STS at angles (45° and 90).

3.4 Conclusion

Forty-eight self-tapping screw (STS) connections used to connect a CLT core to light wood-frame floor headers were tested under monotonic and reversed-cyclic load to investigate the strength, stiffness, ductility, and energy dissipation capacity of the connections. Three types of STS insertion angles were tested and compared: 45°, 90°, and mixed angles (90° and 45°). The results showed that all configurations of the connections have acceptable lateral load capacity. Furthermore, the connections with mixed angle STSs possessed high stiffness, ductility, and energy dissipation capacity and can be an efficient way to connect the light wood-frame structure to CLT cores under wind and seismic load. The detailed findings are summarized below:

- STSs were capable of transferring high lateral forces, which makes them feasible to be used in hybrid light wood-frame structures connected to CLT cores where a limited length of CLT core is available for installing the connections.
- Connections with 10 mm STSs had slightly higher strength than those with 8 mm STSs. However, 10 mm STSs were more prone to splitting wood; therefore, distance should be maintained between screws when they are connected to dimension lumber. Predrilling may also help prevent lumber splitting if enough distance cannot be guaranteed.
- 45° STS connections had greater stiffness but significantly lower ultimate displacement than 90° STS connections. It is recommended that these connections be detailed in accordance with capacity design principles and be regarded as non-dissipative (force-controlled) connections.
- Although the 90° STS connections had similar ductility to 45° STS connections, which is due to the definition of ductility ratio, their energy dissipation capacity was much larger than that of 45° STS connections.

- When combining 45° and 90° STSs in a connection, the system benefitted from the advantages of individual connection and made the STS joint a much more ductile connection.
- All test specimens provided acceptable energy dissipation capacity, as indicated by equivalent viscous damping values, which is not consistent with the conductions derived based on ductility ratio and energy dissipation values. Further research is needed to address this issue.

Chapter 4 Seismic Assessment of a Hybrid Light Wood-Frame Structure Connected to a Balloon-Type CLT Core Wall

4.1 Introduction

Most low-rise (up to 4 storeys) residential buildings in North America are constructed with light wood-frame (LWF) system [1]. LWF structures are characterized by their flexibility and energy absorption capabilities through numerous nailing connections, enabling them to withstand earthquakes well in the past [3]. While the National Building Code of Canada [15] allows the construction of up to 6-storey buildings with LWF walls as the lateral load resisting system (LLRS), the use of LWF construction in mid-rise wood building sector remains challenging due to restrictions on architectural design and lack of stiffness in wind design [68]. To address these challenges, a program called TF2000 [69] had been initiated in the UK. In that project, dynamic characteristics of a full-scale six-storey LWF structure were tested under forced and ambient vibrations. The results showed that addition of a staircase to bare light wood-frame prototype significantly increased the translational stiffness. There have been many other efforts to combine LWF construction with stiffer structural systems to compensate for the low lateral rigidity [70-71] .

To increase the lateral rigidity of multi-storey LWF systems, a potential approach is to combine the CLT core with LWF construction. Combining the two subsystems could potentially result in improved stiffness, strength, ductility, thus achieving the desired design targets. CLT walls exhibit a relatively high level of rigidity, making the connections the primary source of ductility in the system [72]. When combining two structural systems, the links between the two subsystems could also contribute to the energy dissipation of the whole system. In current practice, the core such as stairways and elevator shafts are typically built structurally separate from the LWF system. NBCC

[15] recommends using the lowest value of the R_dR_o of individual systems when designing a hybrid structure. This means that the higher energy dissipation capacity of the more ductile system would be ignored in the design, which may be too conservative. This study investigates the effect of different connection properties on the seismic response of a hybrid building system. Hybrid structural models are designed with self-tapping screw (STS) connections inserted at 45°, 90°, and mixed angles (45° + 90°) and Incremental Dynamic Analysis (IDA) [73] was run to assess if the proposed R_dR_o provides sufficient safety margin.

Only a handful of studies attempted to evaluate the response modification factors of hybrid timber structures. Zhou et al [74] studied multi-story hybrid light wood-frame buildings connected to a masonry core assuming different resisting ratios of the two sub-systems and the connections between them. The seismic force modification factors and the fundamental periods were investigated. The authors found that the relative stiffness of the wood, masonry and connection systems and the ultimate deformation of the sub-systems influenced the failure mode. They proposed that a larger R_dR_o factor than the lowest values of the two systems could be used to design the hybrid structure. Follesa and Fragiacomo [75] studied a platform-type LWF/CLT building with CLT floor diaphragms with LWF walls and CLT walls as LLRS. The contribution of CLT wall and LWF wall to lateral resistance varied among archetypes. They proposed and verified the analytical formulation for determining the ductility-related force modification factor (R_d) of hybrid systems. Chen et al.[76] developed empirical equations of ductility ratio, μ, and R_d based on the strength ratio of the individual LLRSs for systems with different ductility levels. Tesfamariam et al.[77] evaluated a hybrid system of CLT walls and reinforced concrete beams with built up timber columns. They performed FEMA P695 [46] procedure using Canadian seismicity and design factors to quantify the

ductility-related force modification and found that the R_dR_o = 2 × 1.5 were acceptable for this hybrid system.

A thorough performance assessment is needed to get a better understanding of the influence of connection ductility on the performance of hybrid systems. Herein, the experimental results of a prior project (chapter 3) on self-tapping screw (STS) connections between LWF construction and CLT wall panels were employed to compare the seismic response of hybrid LLRS buildings. The Canadian Construction Material Center (CCMC) [18] procedure was used to quantify the force modification factors for the considered archetypes.

4.2 Methodology for Evaluation of Seismic Performance

The FEMA P695 [46] is a procedural methodology which establishes the seismic response parameters for a new lateral load resisting system. It requires that archetypes cover all expected range of structural and geometrical parameters which is usually time-consuming. Herein, the newly developed CCMC [18] guideline based on FEMA P695 which suits NBCC [15] was followed in this study. According to this simplified procedure, the evaluation of seismic performance was carried out with the following steps:

- There were 15 archetype structures (five configurations designed with three building heights) designed using Equivalent Static Force Procedure (ESFP) with initial estimates of R_dR_o.
- Nonlinear springs were used to simulate energy dissipative elements that include STS connections between the two subsystems, LWF shear walls, CLT-to-foundation hold-downs. The deformation capacity for yielding elements was specified as the displacement when the load drops to 80% of maximum resistance [66]. The non-

dissipative elements were designed using capacity design rules (low-ductility STS connections, shear connectors and CLT panels).

- The nonlinear dynamic analysis was performed using 22 far-field earthquake records recommended by FEMA P695 and scaled to the uniform hazard spectrum (UHS), a level of ground motion with 2% change of being exceeded in 50 years according to NBCC [15]. The maximum inter-storey drift ratio limit of 2.5% specified in the NBCC [15] was adhered to for all responses of buildings when the ground motions were scaled to 100% of UHS.
- If the design satisfied the requirements under the 100% UHS intensity level ground motion, a second series of nonlinear dynamic analysis was conducted using the ground motions scaled to 200% of the UHS. In other words, the acceptance criteria of CCMC are consistent with a collapse margin ratio of 2 in the FEMA P695 procedure.
- Failure of the hybrid structures was defined as either the dynamic instability (when the tangent slope of the IDA curve equals 20% of the initial IDA slope [48]) or deformation capacity (80% drop down displacement) exceedance happened. The system failure is also defined as when more than 50% of ground motions results in collapse.
- If all performance criteria were met at 100% and 200% of the UHS, then R_dR_o was accepted for the single archetype. Otherwise, the system was reanalyzed with a lower R_dR_o and the procedure was repeated.

4.3 Identification of Case Study Configurations

The first step is to establish archetypes which are representative of the possible design configurations. The properties of the connection between the LWF construction and CLT core influence how the two subsystems interact under the seismic load. Therefore, three types of connections were

considered for the hybrid archetypes: STS connections inserted at 45°, 90°, and mixed angles (45° + 90°) described in Chapter 3 of this thesis. As reported in the experimental study [20], 45° STS, 90° STS and mixed-angle STS connections have a ductility ratio (μ) of 3.3, 3.7 and 37.7, respectively. Since the 45° STSs have a small ultimate deformation (4.8 mm), they were considered as non-dissipative elements and designed based on capacity design rules. 90° STSs have large ultimate deformation (30.3 mm), so they were regarded as energy-dissipative connections in this project. The mixed-angle STSs have both high ductility ratio and large ultimate displacement (41.7 mm), so they are identified as high-ductility connections. There were three main configurations of LLRSs considered in this project: (1) pure LWF wall construction (Case A); (2) hybrid LWF-CLT building with different types of connections (case B: 45° STS connections, case C: 90° STS connections and case D: mixed-angle STS connections); (3) pure balloon-type CLT core wall building (Case E) which are presented in **Figure 4.1**. Each configuration was designed in 1, 4 and 6-storey archetypes to cover the range of low-rise to mid-rise LWF construction. The standard LWF shear wall tested by Ni et al. [78] was used as LWF walls in this study. Hold-downs with Φ20 mm dowels tested by Brown and Li [79] were used for CLT core wall connections to the foundation. The CLT core wall was detailed with capacity protected shear connectors to control the sliding of the wall. Conventional angle brackets test data [80] was used to represent shear connectors. The behavior of connections were derived from reversed-cyclic tests on 10 mm STS lumber-to-CLT connections loaded along the minor axis of 5-layer CLT panels in this study [20].

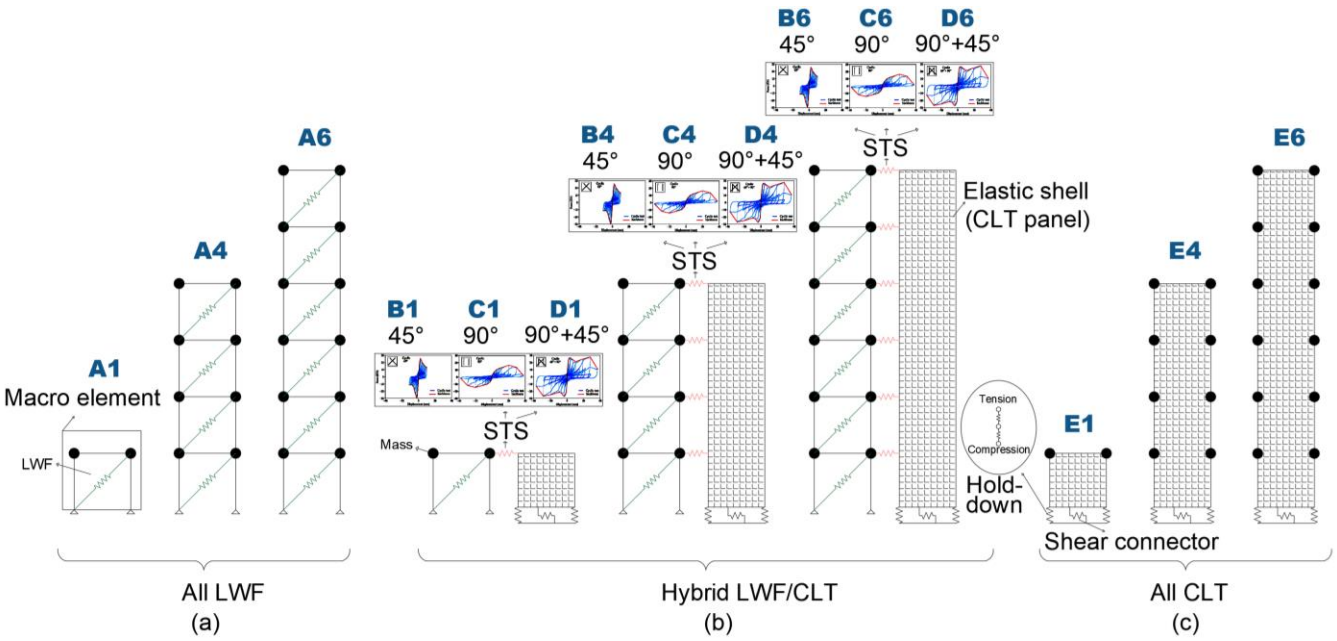

Figure 4.1. Archetype cases: (a) Pure LWF construction; (b) Hybrid LWF/CLT cases; and (C) Pure CLT core wall as LLRS.

4.4 Archetype Design

Five different building configurations were considered in this study. All these models were residential buildings that had the same plan layout of 33 × 26 m (**Figure 4.2**) and floor height of 2.8 m. The direction of earthquake load under consideration was along the East-West direction. The CLT core walls in case A were assumed to be structurally separated from the LWF system, as a result they were not included in the finite-element model. In hybrid configurations, CLT walls were structurally connected to the light wood-frame structures with self-tapping screws. In case C, the CLT cores are the only system resisting the lateral loads. Since the floor plan was symmetrical, only a quarter of layout was used in finite element modeling and mass calculation (containing one of the CLT core walls and surrounding LWF walls). The building was designed for a lumped dead load of 1.8 kPa and 0.95 kPa for floors and roof, respectively. A snow load of 1.08 kPa was also considered in the calculation of the roof seismic weight. The buildings were assumed to be in Vancouver on Site Class

C. According to NBCC [15] the design spectral acceleration for periods of 0.2 s, 0.5 s, 1 s, 2 s and 5 s were 1.09 g, 0.876 g, 0.508 g, 0.309 g, and 0.087 g, respectively. A primary Equivalent Static Force Procedure was carried out using fundamental periods (T_a) calculated based on NBCC [15] ($T_a = 0.05h^{3/4}$, where h is the building height in meter). Using the stiffness derived based on the equivalent energy elastic-plastic method [44], the analytical period was obtained. All analytical periods were more than twice the code's empirical value ($2T_a$) which are presented in **Table 4.1**. Since $2T_a$ is the cut off point for strength design required by NBCC [15], $2T_a$ was adopted as the final design period with no further iteration. The corresponding design spectral acceleration of the final design for 1, 4 and 6-storey buildings were 1.08 g, 0.79 g and 0.64 g, respectively.

Table 4.1. Fundamental periods of archetypes.

Period (s)	**1-storey**	**4-storey**	**6-storey**
Ta (NBCC)	0.11	0.31	0.41
2 × *Ta*	0.22	0.62	0.82

Notes: [1] Period calculated based on mechanical properties and EPP

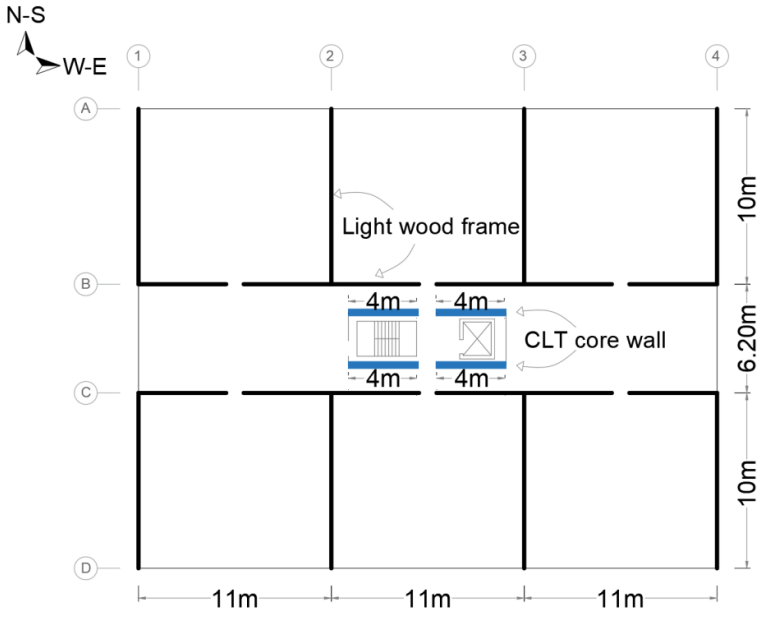

Figure 4.2. Floor plan.

The ESFP incorporates the inelastic behavior (ductility-related factor) and the dependable portion of reserved strength (overstrength-related factor) by reducing elastic base shear by R_dR_o. The NBCC [15] adopted the ductility factor (R_d) for the design of platform construction using CLT shear walls and LWF construction as 2 and 3, respectively. However, no seismic force modification factor is specified for designing balloon-type CLT walls in the NBCC [15]. The final values in the iteration process of quantifying R_d factor were presented in this paper. Case A was designed with $R_d = 3$. Case B, C and E were designed with $R_d = 2$, case D was designed with $R_d = 2.5$.

The overstrength factor takes into account the actual strength of materials, i.e., the effect of discrete member sizes, the increased strength due to nonstructural elements, strain hardening, difference between nominal and factored resistances and redistribution of internal forces in the inelastic range [81]. R_o was set to be 1.7 for the configurations with only LWF construction (case A). As suggested by CCMC [18] for balloon-type CLT and other hybrid configurations (case B, C, D and E) $R_o = 1.5$ was adopted. The final accepted seismic modification factors based on the time history analysis in this study according to CCMC guideline are listed in **Table 4.2**.

Table 4.2. Seismic modification factors of archetype cases.

Configuration	Description	R_o	R_d
Case A	LWF wall	1.7	3
Case B	Hybrid	1.5	2
Case C	Hybrid	1.5	2
Case D	Hybrid	1.5	2.5
Case E	CLT core wall	1.5	2

The LWF system on each storey was assumed to be a macro-element that represents all the LWF walls in that storey. According to wood design manual [82], the factored shear strength of LWF shear wall is equivalent to half the ultimate lateral load determined from testing. The reversed cyclic test

result of wall 3r' (2.44 m × 2.44 m) in Ni et al. [78] was used to calibrate the LWF wall macro-element. This wall has an ultimate deformation of 84 mm (3.5% drift ratio). Because the maximum resistance of the LWF wall was recorded 59.8kN (24.5 kN/m), a force of 29.9 kN was considered as the design shear strength of the 2.44 m long LWF wall.

The design strength of hold-downs (HD), shear connectors (SC) and connection (STS) between the two subsystems were obtained based on statistics of experiments and literature-based recommendations for capacity design principles. The capacity-based design rules have been integrated into seismic design guidelines to ensure the expected energy dissipation occurs in ductile elements and brittle failure modes are avoided. This is accomplished through multiplying the design resistance of non-dissipative connections with a capacity adjustment factor (γ) derived based on dissipative connections (the ratio of 95th percentile of dissipative connection to its design resistance). This factor is commonly known as overstrength factor [83]. To avoid confusion with the R_d (overstrength-related force modification factor) in this paper, the term "capacity adjustment factor" was used in this study to refer to γ throughout the remainder of the paper. As per CSA O86-19 [62], non-dissipative elements must remain elastic when the dissipative elements reach their 95th percentile ($R_{95^{th}}$) of ultimate strength. The $R_{95^{th}}$ of elements were found through the mean of test's maximum resistance ($R_{max,mean}$) and coefficient of variation (CoV), assuming a normal distribution in test results. Subsequently, the design value of connections (R_{design}) was determined as the ratio of $R_{95^{th}}$ to the corresponding γ factor. **Table 4.3** presents the design strengths of connections' tests before scaling and capacity protection rules were applied.

Table 4.3. Design strengths of connections and CLT core elements.

Element	Ductility (μ)	Ultimate deformation (mm)	$R_{max,mean}$ (kN)	CoV (%)	R_{95}^{th} (kN)[1]	γ	R_{design}[2] (kN)
45° STS (Case B) [20]	3.3	4.8	35.5	18.0	46.0	1.6 [83]	28.8
90° STS (Case C) [20]	3.7	30.3	22.4	5.0	24.2	1.6 [83]	15.1
45° + 90° STS (Case D) [20]	37.7	41.7	39.0	11.0	46.0	1.6 [83]	28.8
Hold-down (HD) [79]	23.2	42.5	268.5	1.2	273.8	1.5 [79]	182.5
Shear connector (SC) [80]	7.3	41.3	13.4	5.0	14.5	1.3 [83]	11.2

Notes: [1] $R_{95}^{th} = R_{max,mean}(1 + 1.645 \times CoV)$; [2] $R_{design} = R_{95}^{th} / \gamma$

The subsystems were designed to equally share the design base shear. Therefore, specified lateral earthquake force of NBCC was split in half and applied to both the LWF system and the CLT core wall. This approach makes the design forces of connections between the two substructures to be the same as the NBCC load distribution pattern, i.e. half of the design story forces are transmitted to the CLT core trough the connections on each floor. **Table 4.4** lists the design forces that were determined through Equivalent Static Force Procedure (ESFP). The design values have embodied the capacity rules for non-dissipative elements. In order to ensure that the design capacities of non-dissipative elements were appropriately accommodated, the elements in the numerical model were subjected to scaling to increase their design strengths (R_{design}) to the forces listed in **Table 4.4**.

The dissipative elements of case E (pure CLT) and case B (hybrid building with low-ductility connections) are the hold-downs for CLT core. Therefore, to ensure the yielding of hold-downs are given priority and CLT remains elastic, γ of hold-down was applied to the NBCC's seismic design

forces of CLT panels. Because shear connectors are designed to have limited sliding behavior, γ of hold-down was also applied to the NBCC's base shear and used as the force to scale shear connectors. γ of hold-down was set 1.5 (**Table 4.3**) which were recommended based on characteristic experimental strengths for dowelled CLT hold-downs [79].

Another primary energy dissipative element in hybrid configurations with 45°, 90° STS connections (Case C and D) are the STS connections between the LWF and CLT core systems. As recommended by Gavric et al. [83], a capacity adjustment factor of 1.6 was chosen for hybrid cases to design shear connectors, as the value considered for panel-to-panel screw connection test were reported 1.6 (**Table 4.3**). As explained in chapter 3 and due to limited deformation capacity, The 45° STS is categorized as a non-ductile element and is capacity protected to behave rigidly. Therefore, a capacity adjustment factor of 1.3 was chosen to design the 45° STS between the subsystems.

The CLT panels were designed to meet CSA O86-19 [62] requirements with a width of 4 m. The end distance between the hold-downs and the corner of wall was assumed to be 40 cm. For case E, the 1, 4 and 6-storey archetypes were detailed with 3-ply (105 mm thick), 5-ply (175 mm) and 7-ply (245 mm) grade E1 CLT panels, respectively. The 1, 4 and 6-storey hybrid archetypes were detailed with 3-ply (105 mm thick), 3-ply (105 mm thick) and 5-ply (175 mm thick) grade E1 CLT panels, respectively. Since the panel width plays an important role in rocking behavior of the CLT core, wall width was kept consistent (4 m) across all archetypes for the sake of comparison.

The detailed design calculation of the archetypes is presented in Appendix C.

Table 4.4. Design forces (kN) for LWF walls, STS connections, hold-downs (HD) and shear connectors (SC) of each archetype.

	A1	**B1**				**C1**				**D1**				**E1**	
Storey No	LWF	LWF	STS$^{*(1.3)}$	HD	SC$^{*(1.5)}$	LWF	STS	HD	SC$^{*(1.6)}$	LWF	STS	HD	SC$^{*(1.6)}$	HD	SC$^{*(1.5)}$
1	55.6	47.3	61.4	41.4	70.9	47.3	47.3	41.4	70.9	37.8	37.8	33.1	56.7	82.7	141.8
	A4	**B4**				**C4**				**D4**				**E4**	
Storey No	LWF	LWF	STS$^{*(1.3)}$	HD	SC$^{*(1.5)}$	LWF	STS	HD	SC$^{*(1.6)}$	LWF	STS	HD	SC$^{*(1.6)}$	HD	SC$^{*(1.5)}$
4	68.8	58.5	76.0	-	-	58.5	58.5	-	-	46.8	46.8	-	-	-	-
3	144.9	123.2	84.1	-	-	123.2	64.7	-	-	98.5	51.8	-	-	-	-
2	195.6	166.3	56.1	-	-	166.3	43.1	-	-	133.0	34.5	-	-	-	-
1	221.0	187.9	28.0	468.8	282.0	187.9	21.6	468.8	281.8	150.3	17.3	375.0	225.4	937.6	563.5
	A6	**B6**				**C6**				**D6**				**E6**	
Storey No	LWF	LWF	STS$^{*(1.3)}$	HD	SC$^{*(1.5)}$	LWF	STS	HD	SC$^{*(1.6)}$	LWF	STS	HD	SC$^{*(1.6)}$	HD	SC$^{*(1.5)}$
6	59.2	50.3	65.4	-	-	50.3	50.3	-	-	40.2	40.2	-	-	-	-
5	131.9	112.1	80.4	-	-	112.1	61.8	-	-	89.7	49.5	-	-	-	-
4	190.1	161.6	64.3	-	-	161.6	49.5	-	-	129.3	39.6	-	-	-	-
3	233.8	198.7	48.2	-	-	198.7	37.1	-	-	159.0	29.7	-	-	-	-
2	262.9	223.5	32.2	-	-	223.5	24.7	-	-	178.7	19.8	-	-	-	-
1	277.4	235.8	16.1	859.2	354.1	235.8	12.4	859.2	353.7	188.6	9.9	687.4	283.0	1718	707.4

Notes: $^{*(\gamma)}$ These elements are capacity protected and the applied capacity adjustment factors (γ) are stated in the parenthesis.

4.5 Incremental Dynamic Analysis

4.5.1 Finite Element Modeling

Simplified numerical models have been proven to reproduce responses that matched the experimental results [84]. As a part of the CUREE-Caltech wood frame research project [85], a program called Seismic Analysis of Wood-frame Structures (SAWS) [86] was developed which has been implemented as a material in OpenSees [31] platform and has the ability to model the building as a two-dimensional system. Each storey of the LWF construction was simulated with three rigid

truss elements and one diagonal nonlinear spring. The SAWS [32] model was adopted to simulate the hysteresis performance of this macro-element. The parameters of SAWS model are listed in **Table 4.5**.

Table 4.5. SAWS model parameters for LWF shear wall macro-elements.

Parameter	*S0*	*DU*	*α*	*ß*	*R1*	*R2*	*R3*	*R4*	*F0*	*FI*
Value	7.0	42	0.7	1.1	0.065	-0.09	1.22	0.03	68	8

As shown in **Figure 4.1**, elastic shell elements were used for CLT panels because nonlinearity is expected to happen only at the joints. Since hold-down was assumed to resists uplift only, DowelType uniaxial properties [87] in OpenSees were assigned to a nonlinear spring (zero length element) in tension to simulate the hold-down performance. The contact compression of the wall edge to the foundation was modelled with another spring using elastic-no-tension material with an elastic modulus of 1500 MPa as recommended by Sun et al. [88]. The shear connectors (CLT-to-foundation) and CLT-to-LWF connection were also modelled with the DowelType material (Appendix C) and the parameters of the models are listed in **Table 4.6**. To better simulate the experimental hysteresis of the mixed angle connection (45°+90° STS in case D), piece-wise linear envelope curves were adopted. All the other connections were simulated with Bézier curve as their backbone. The verification of numerical results with reversed cyclic loading test on each element is shown in **Figure 4.3**. The total energy dissipated during the cyclic tests is consistent with the energy observed during the tests. The 45° STS, 90° STS, mixed angle connection, hold-down, shear connector and LWF wall failed at 4.8 mm, 30.3 mm, 41.7 mm, 42.5 mm, 41.3 mm and 84 mm, respectively, based on 80% drop down of the peak resistance.

Table 4.6. Model parameters of connection, hold-down and shear connector.

Parameters (Bezier curve)	STS 90˚	STS 45˚	Hold-down	Shear connector	Parameters (Piece-wise linear)	STS 45˚+90˚
F_{I0}	1.3	4	2.5	0.53	-[1]	1.1
K_{p0}	0.97	10.4	0.6	0.75	-	2.8
K_{u0}	3.1	1.1	1.1	2.3	-	0.9
C	0.8	1.1	0.6	0.8	-	0.7
β	1.1	1.04	1.05	1.12	-	1.08
γ	1	1	1	1	-	1
η	0.1	0.14	0.07	0.14	-	0.08
D_y	3.4	1.15	0.1	2.1	-	0.85
a_p	1.1	1.29	0.2	0.9	-	1.15
a_u	0	0.1	0.06	0	-	0.03
a_r	0.85	0.7	0.68	0.31	-	0.7
D_{b1} (F_{b1})	2.1(11)	0.5(17)	0.3(255)	3(8.1)	D_1(F_1)	1.7(37.5)
D_{b2} (F_{b2})	7(12.1)	1.1(28)	5(260)	5.9(10)	D_2(F_2)	10(25)
D_c (F_c)	26(23)	2.5(35)	35(269)	24.5(14)	D_3(F_3)	34.2(39)
K_d (D_u)	1.5(30.5)	2.5(4.8)	5(42.5)	0.1(41.3)	D_4(F_4)	43(30.5)

Notes:[1] "-" the same as Bezier curve

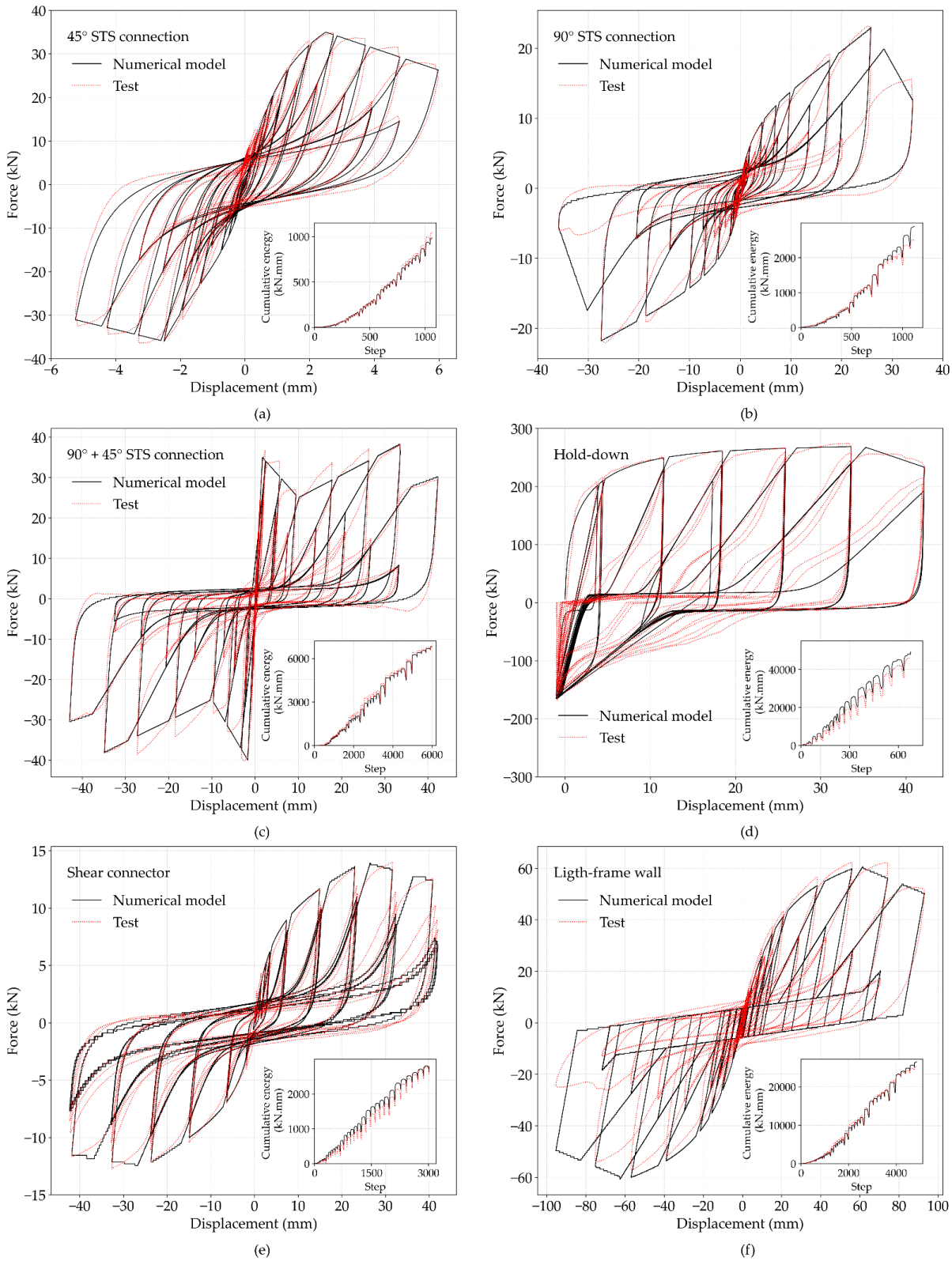

Figure 4.3. Comparison of hysteresis loops of numerical model and tests: (a) 45° STS connection; (b) 90° STS connection (c) 90° + 45° STS connection; (d) Hold-down; (e) Shear connector; and (f) LWF wall.

4.5.2 Non-linear Time History Analysis

To perform non-linear time history analysis, each archetype was subjected to a single component of the 22 far-field earthquake records suggested by FEMA P695 [77] guidelines. First, the ground motions were normalized with respect to median peak ground velocity. Then, the records were collectively scaled to the NBCC 2020 [15] uniform hazard spectrum (UHS) of Vancouver. **Figure 4.4** compares the median response spectra and the UHS. It shows that median response spectrum is higher than 90% of the UHS across a period range of 0.05 s to 1.66 s which covers up to two times the longest fundamental period of structures. A complete incremental dynamic analysis (IDA) [73] was carried out. The suite of ground motions was scaled up by increments of 0.1 g until the collapse of each archetype. The failure criteria was defined as the deformation demand on an element that exceeded its deformation capacity or when the dynamic instability happened, i.e., the tangent slope of the IDA curve equals 20% of the initial IDA slope [48]. To increase the accuracy of recorded collapse capacity, a linear search between the highest non-collapsing and lowest collapsing point with an acceptable tolerance of 0.01g was performed.

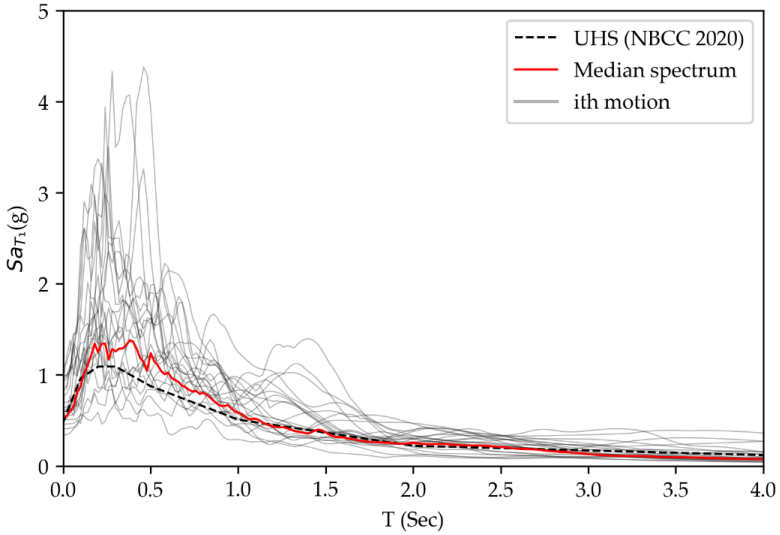

Figure 4.4. Comparison of response spectra of the FEMA P695 far-field ground motions and uniform hazard spectrum of Vancouver.

4.6 Performance Evaluation of Archetypes

Using the performance evaluation procedure outlined in CCMC [18] guideline, iteration procedures were carried out to evaluate the trial R_dR_o factors until satisfied values were achieved. This paper focuses on the final accepted factors which are $R_d = 2$ for case B, C and E and $R_d = 2.5$ for case D. Case A demonstrated satisfactory collapse capacities when designed with $R_d = 3$ (**Table 4.2**). At the design intensity (100% UHS), the NBCC sets a Maximum Inter-Storey Drift ratio (MISD) limit of 2.5%. **Figure 4.5** illustrates the median value of MISD under 22 ground motions until collapse.

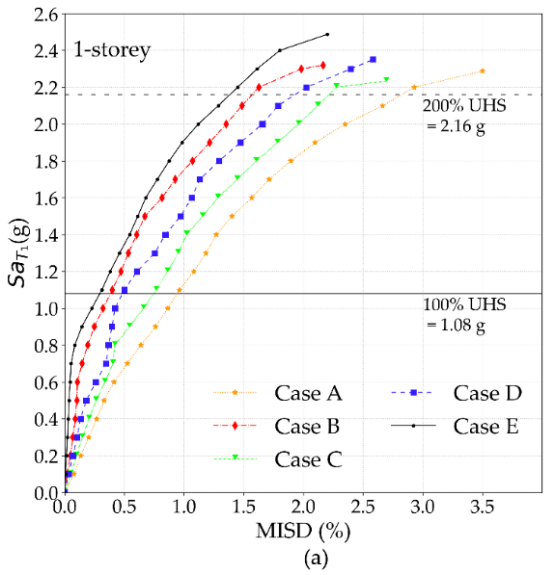

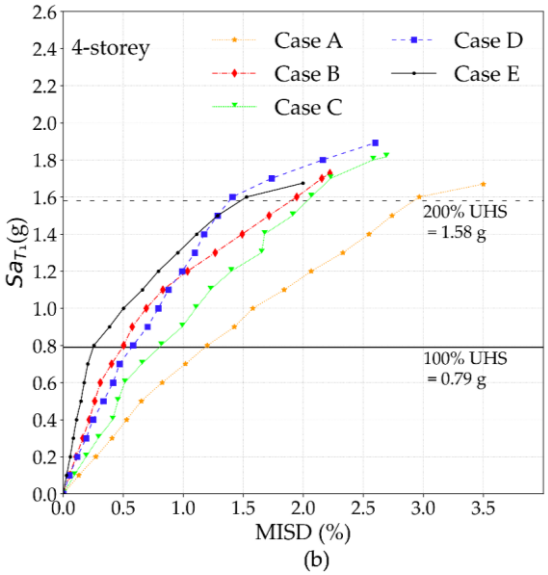

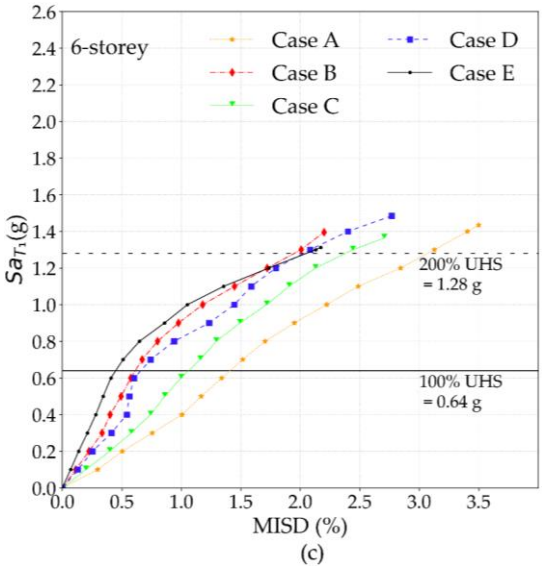

Figure 4.5. Median IDA curves: (a) single-storey; (b) 4-storey; and (c) 6-storey archetypes

The results clearly indicate that MISD of all archetypes is below 2.5% at the 100% UHS level. Moreover, all archetypes failed at an intensity level more than 200% UHS, which satisfy the second requirement of the CCMC guideline. The collapse MISD ranges between 2% to 3.5%. The high-capacity hold-downs used in case E (pure CLT core) were able to withstand high axial forces and provide the necessary energy dissipation. Among the hybrid cases designed with R_dR_o = 2.0 × 1.5 (Cases B and C), the MISDs at design intensity (100% UHS) of case B (hybrid structures with 45° STS) were 53%, 40% and 44% less than those of case C (hybrid structures with 90° STS) in 1-storey,4storey and 6-storey archetypes, respectively. Despite of lower deign force (R_dR_o = 2.5 ×1.5), Cased D (hybrid structures with mixed-angle STS) experienced design level drifts that were 33%, 19% and 26% less than case C in 1-storey,4storey and 6-storey archetypes, respectively.

These findings demonstrate that the use of 45° STS connections is considered the most effective means of controlling lateral displacement, but if one aims to both minimize displacement and design with a higher R_dR_o factor, employing mixed-angle STS connections is a preferable option.

Nevertheless, it is worth noting that while mixed-angle STS connections can achieve both objectives. Its displacement reduction capability may not be as efficient as that of 45° STS connections at design level intensities but provides a superior seismic safety margin at near-collapse state.

Case A archetypes (pure LWF construction) collapsed at MISD of 3.5% due to LWF walls reaching their ultimate deformation at the top storey. Collapse of Case B, C and E occurred because of hold-down failure, while only archetypes of case D collapsed as a result of connection failure at the top storey. The maximum value of median shear connector displacement at collapse of structures among all archetypes was 11.7 mm and 45° STS connections were deformed up to 2.3 mm in all cases at near-collapse limit state. The adequacy of capacity design procedure was proved since shear connectors and 45° STS connections sustained small deformations.

Figure 4.6 presents the elements' response of case B, C and D under Loma Prieta (Capitola station) in the 6-storey archetypes. Only 1st, 4th and the 6th storeys of the 6-storey are shown because these storeys had more significant contrast in response compared to 2nd, 3rd and the 5th storeys. The connection hysteresis loops indicate that with increase in building height the force demand on connections increases. The element failures that signaled collapse are pointed out in **Figure 4.6** c, g, and j.

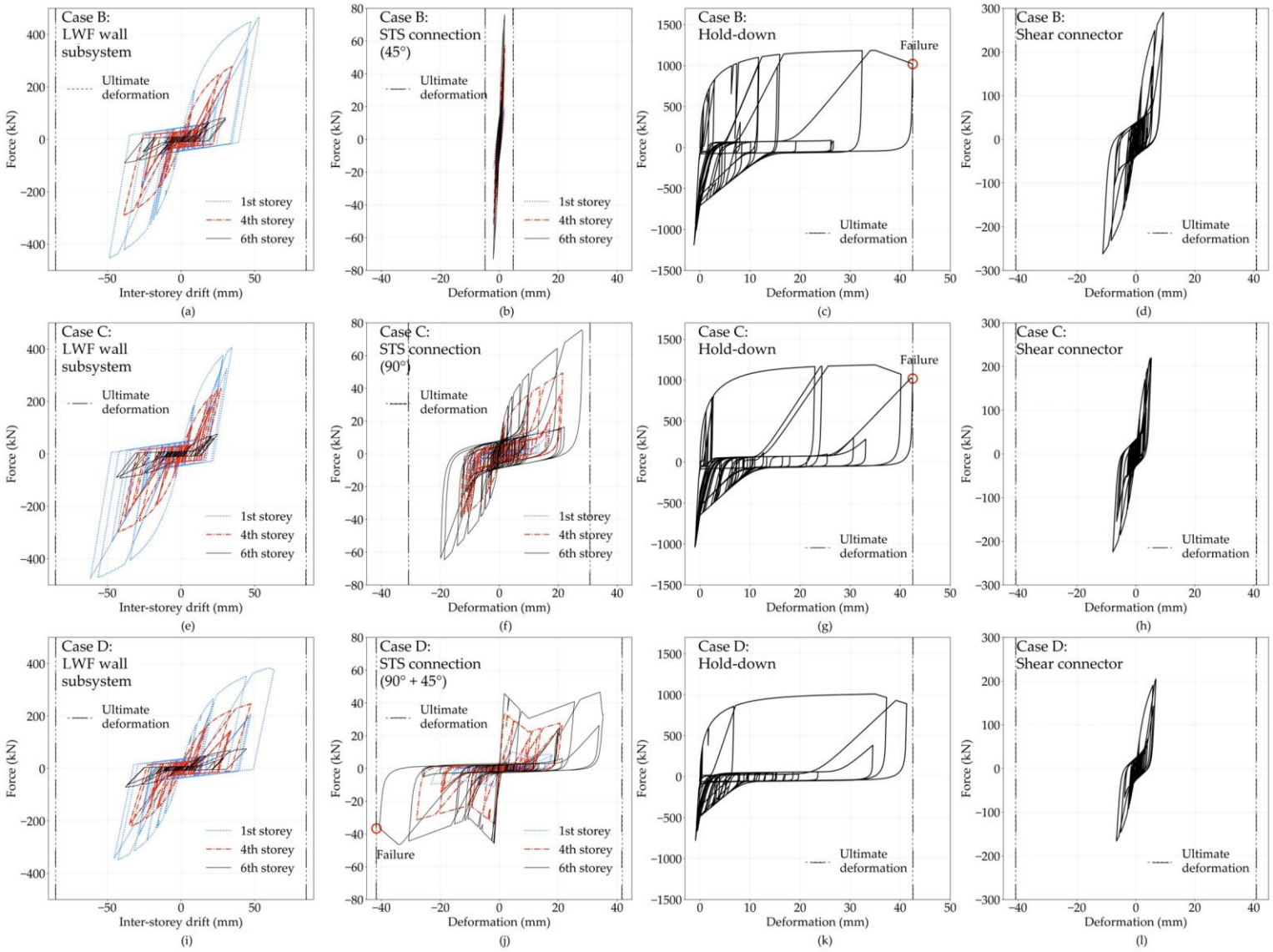

Figure 4.6. Element force-deformation hysteresis under Loma Prieta at collapse (6-storey archetypes): (a-d) Case B; (e-h) Case C; and (i-j) Case D.

The median interstorey drift and connection deformation of multistorey archetypes at collapse are shown in **Figure 4.7** and listed in **Table 4.7**. As depicted in **Figure 4.7**a, and f, case A exhibited an increasing trend in interstorey drift as the height of the building increased. The connection in the top storey sustained the most damage compared to lower storeys, to the extent that it was the primary cause of collapse in case D.

It is worth noting that under 6 out of 22 ground motions dynamic instability occurred before element failure in case D of one-storey structures. In cases with a CLT core, the interstorey drifts were approximately equal in the middle storeys (2nd and 3rd storeys in 4-storey and 2nd to 5th storeys in 6-storey structures) but the first storey significantly experienced higher drifts.

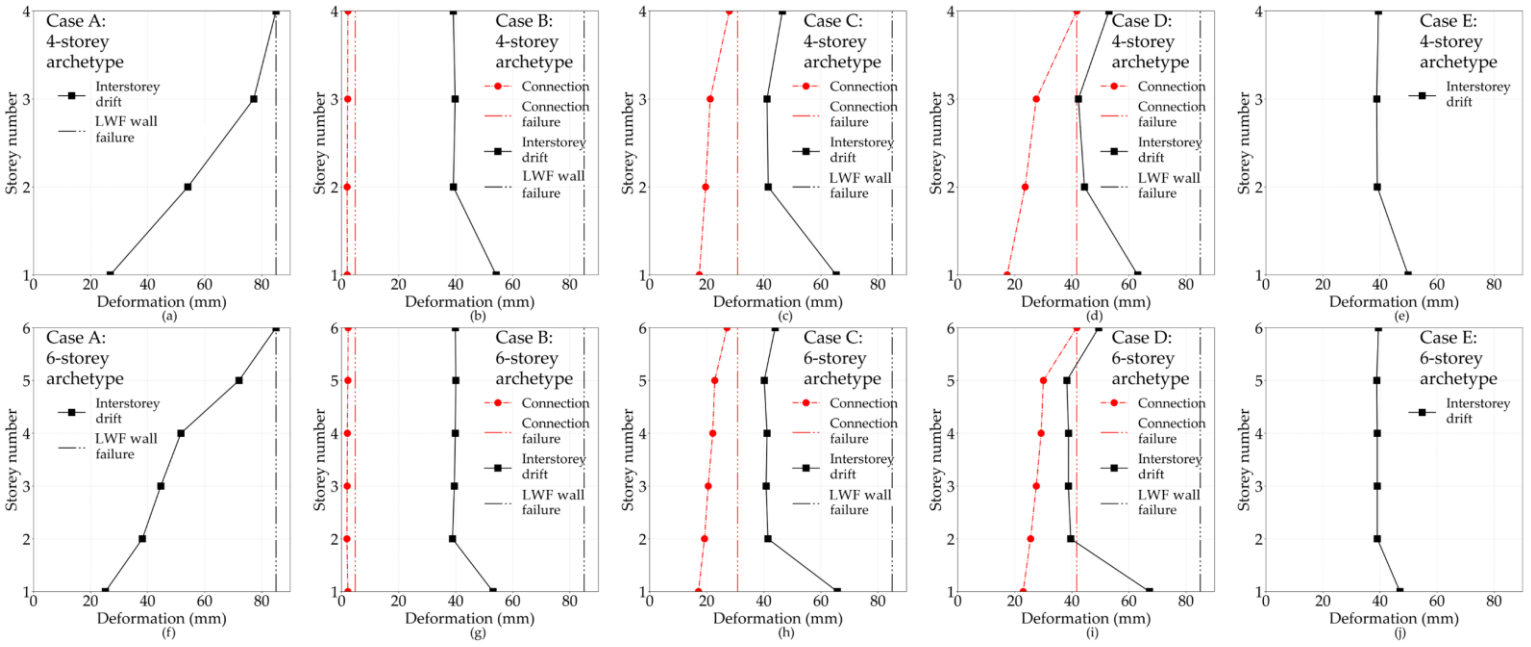

Figure 4.7. Median interstorey drift and connection deformation at collapse: (a-e) 4-storey archetypes; and (f-j) 6-storey archetypes

Table 4.7. Median interstorey drift and connection deformation at collapse

	A1	**B1**				**C1**				**D1**				**E1**	
Storey No	LWF	LWF	STS	HD	SC	LWF	STS	HD	SC	LWF	STS	HD	SC	HD	SC
1	85.0	52.8	2.3	42.5	10.7	65.3	25.4	36.5	6.7	63.5	29.3	30.2	5.9	42.5	11.7
	A4	**B4**				**C4**				**D4**				**E4**	
Storey No	LWF	LWF	STS	HD	SC	LWF	STS	HD	SC	LWF	STS	HD	SC	HD	SC
4	85.0	39.2	2.2	-	-	46.5	27.9	-	-	53.0	41.7	-	-	-	-
3	77.2	39.8	2.1	-	-	41.1	21.2	-	-	42.3	27.5	-	-	-	-
2	54.1	39.2	1.9	-	-	41.6	19.6	-	-	44.4	23.6	-	-	-	-
1	26.9	54.2	2.0	42.5	11.7	65.4	17.4	42.5	7.6	63.0	17.3	40.9	6.9	42.5	11.2
	A6	**B6**				**C6**				**D6**				**E6**	
Storey No	LWF	LWF	STS	HD	SC	LWF	STS	HD	SC	LWF	STS	HD	SC	HD	SC
6	85.0	40.4	2.3	-	-	44.0	27.1	-	-	49.4	41.7	-	-	-	-
5	72.0	40.0	2.2	-	-	40.2	22.8	-	-	38.2	30.0	-	-	-	-
4	51.7	39.9	2.0	-	-	41.1	22.1	-	-	38.8	29.2	-	-	-	-
3	44.6	39.5	1.9	-	-	40.8	20.5	-	-	38.8	27.5	-	-	-	-
2	38.2	38.9	1.9	-	-	41.4	19.2	-	-	39.6	25.5	-	-	-	-
1	25.2	53.1	2.2	42.5	11.6	65.8	17.1	42.5	8.3	67.2	22.9	39.9	6.1	42.5	7.6

4.7 Conclusion

The focus of the study was to evaluate the effect of ductility of inter-system connections on the R_dR_o of a hybrid LWF/CLT structure connected with self-tapping screws. Three types of connections with 45°, 90°, and mixed angles (45° + 90°) STSs were considered in the archetype development. One-, four- and six-storey structures with pure LWF wall (case A), hybrid buildings with 45° STS (case B), 90° STS (case C) and mixed-angle STS (case D) connections, along with a pure CLT core wall system (Case E) were investigated. The added energy dissipation was expected through yielding of connections in horizontal shear of LWF floor and CLT core wall. The results reported in this work are limited to accepted R_dR_o and the assumed half-half design resisting ratio of the two sub-systems. The following conclusions from this performance analysis are summarized:

- R_d = 2 and R_o = 1.5 were acceptable for hybrid structures with 45° STS and 90° STS connections (cases B, C) and pure CLT structures (Case E). The application of 45° STS and 90° STS connections did not improve the collapse capacity of the hybrid building to make higher R_d values suitable for design. Hybrid system with mixed-angle STS connections (Case D) designed with R_d = 2.5 and R_o = 1.5 satisfied the CCMC requirements. The trial Rd values were limited to 2, 2.5, and 3 (i.e., from 2 to 3 with 0.5 interval) during evaluation.
- Hybrid systems with CLT core wall and LWF system had lower interstorey drift compared to the pure LWF systems. Combining the two systems increased the lateral stiffness of the light-frame wood system, which addresses the rigidity issues often associated with LWF construction.
- The addition of CLT core to the LWF construction led to a more uniform drift distribution in LWF walls. Therefore, it can prevent concentration of damage and extreme responses in one storey.
- The displacement demands on STS connections are larger on higher storeys compared to lower storeys. Therefore, it is important to exercise greater care when designing connections on higher storeys.

Overall, the present study highlights the efficiency of hybrid LWF/CLT structures, particularly when using mixed-angle STS connections to link the two subsystems. This approach effectively addresses the rigidity issues often associated with LWF construction while also enabling a less conservative design. Designers could use a higher R_dR_o when designing the hybrid structure with mixed-angle STS connections compared to the R_dR_o of CLT structures. This approach can lead to more innovative and optimized designs. The current study provided fundamental insights for design of hybrid LWF/CLT structures. However, the study did not consider archetypes with varying level of design

resistance ratio between the two subsystems. The connection efficiency may be affected by the resistance ratio of the sub-systems which imposes limitations on generality of results.

Chapter 5 Conclusions

The primary goal of this study was to assess the effect of ductility of inter-system connections on the seismic performance of a hybrid LWF/CLT structure connected with self-tapping screws (STS). When combining two structural systems, the connections between the two subsystems could also contribute to the energy dissipation of the whole system. Since pinching effect is a general phenomenon of timber structures, which may significantly reduce their energy dissipation capacity, the first part of the research investigated the effect of pinching and energy dissipation capacity on the seismic performance of subsystems, i.e., timber structures. Light wood-frame structures with identical backbone curves but different pinching levels were analyzed. Incremental dynamic analyses were run on 72 SDOF systems that cover three levels of pinching stiffness, three levels of residual strength, and 12 fundamental periods. The seismic evaluation is presented by the spectral accelerations causing failure of the structure and the hysteresis energy dissipation under a suite of 22 ground motions (2 components per motion). The seismic resistance represented by Sa, and the hysteresis energy, Ey, of SDOF systems were compared and discussed. The main study findings are summarized as follows:

- Pinching effect on seismic performance of timber structures is period-dependent. Short period structures are more sensitive to the pinching effect of hysteresis loops than long period structures.
- Higher residual strength of pinched model leads to higher seismic resistance, while higher pinching stiffness leads to lower seismic resistance. The effect of pinching stiffness on the seismic performance of timber structures is less than that of residual strength.

- A linear relationship between spectral acceleration and the maximum displacement of hysteresis models is observed in IDA curves until the near-collapse state for long period structures, while short period structures experience softening of IDA curves.
- The elastic-perfectly plastic model has much higher seismic capacity than pinched models for structures with periods less than 0.7 s. For longer period structures, the benefit of EEP model is not significant.
- For pinched models, increasing the hysteretic energy dissipation capacity of systems under standard loading protocols will increase the seismic capacity of the systems. For EEP model, the same conclusion is only valid for short period structures.
- The relationship between the seismic capacity, Sa, and the hysteretic energy, Ey, under seismic loads is not always consistent.

In the second part of study, forty-eight self-tapping screw (STS) connections used to connect a CLT core to light wood-frame floor headers were tested under monotonic and reversed-cyclic load to investigate the strength, stiffness, ductility, and energy dissipation capacity of the connections. Three types of STS insertion angles were tested and compared: 45°, 90°, and mixed angles (90° and 45°). The results showed that all configurations of the connections have acceptable lateral load capacity and ductility ratio. However, as explained in Chapter 3, the 45° STS connection should be regarded as a non-energy dissipative connection due to its very limited ultimate displacement. Furthermore, the connections with mixed angle STSs possessed high stiffness, ductility, and energy dissipation capacity and can be an efficient way to connect the light wood-frame structure to CLT cores under wind and seismic load. The detailed findings are summarized below:

- STSs were capable of transferring high lateral forces, which makes them feasible to be used in hybrid light wood-frame structures connected to CLT cores where a limited length of CLT core is available for installing the connections.
- Connections with 10 mm STSs had slightly higher strength than those with 8 mm STSs. However, 10 mm STSs were more prone to split wood; therefore, enough screw spacing should be maintained to avoid this failure. Predrilling may also help prevent lumber splitting if enough distance cannot be guaranteed.
- 45° STS connections had greater stiffness but significantly lower ultimate displacement than 90° STS connections. It is recommended that these connections be detailed in accordance with capacity design principles and be regarded as non-dissipative (force-controlled) connections.
- Although the 90° STS connections had similar ductility to 45° STS connections, which is due to the definition of ductility ratio, their energy dissipation capacity was much larger than that of 45° STS connections.
- When combining 45° and 90° STSs in a connection, the system benefitted from the advantages of individual connection and made the STS joint a more ductile connection.

The final part of the study focuses on estimating the seismic force modification factors (R_dR_o) of a hybrid LWF/CLT structure connected with self-tapping screws. Three different connections with 45°, 90°, and mixed angles (90° and 45°) STSs were considered in the archetype development. One-, four- and six-storey structures with pure LWF wall (case A), hybrid buildings with 45° STS (case B), 90° STS (case C) and mixed-angle STS (case D) connections along with a pure CLT core wall system were investigated. Additional energy dissipation was expected through yielding of connections in horizontal shear between LWF floor and CLT core wall. The results reported in this

work is limited to accepted R_dR_o and the assumed half-half design resisting ratio of the two sub-systems. The following conclusions from this performance analysis are summarized:

- R_d = 2 and R_d = 1.5 were acceptable for hybrid structures with 45° STS and 90° STS connections (cases B, C) and pure CLT structures (Case E). The application of 45° STS and 90° STS connection did not improve the collapse capacity of the hybrid building to make higher R_d values suitable for design. Hybrid system with mixed-angle STS connections (high-ductile connections, i.e., Case D) designed with R_d = 2.5 and R_d = 1.5 satisfied the CCMC requirements. The trial Rd values were limited to 2, 2.5, and 3 (i.e., from 2 to 3 with 0.5 interval) during evaluation.
- Hybrid systems with CLT core wall and LWF system had lower interstorey drift compared to the pure LWF systems. Combining the two systems increased the lateral stiffness of the light wood-frame system, which addresses the rigidity issues often associated with LWF construction.
- The addition of CLT core to the LWF construction led to a more uniform drift distribution in LWF walls. Therefore, it can prevent concentration of damage and extreme responses in one storey.
- The displacement demands on STS connections are larger on higher storeys compared to lower storeys. Therefore, it is important to exercise greater care when designing connections on higher storeys.

Overall, the present study highlights the efficiency of hybrid LWF/CLT structures, particularly when using mixed-angle STS connections to link the two subsystems. This approach effectively addresses the rigidity issues often associated with LWF construction while also enabling a less conservative design. Designers could use a higher R_dR_o when designing the hybrid structure with mixed-angle

STS connections compared to the R_dR_o of CLT structures. This approach can lead to more innovative and optimized designs. The current study provided fundamental insights for design of hybrid LWF/CLT structures. However, the study did not consider archetypes with varying level of design resistance ratio between the two subsystems. The connection efficiency may be affected by the resistance ratio of the sub-systems which imposes limitations on generality of results.

5.1 Research Limitations

The findings of this study should be considered in light of some limitations. In the experimental study, there were only four replicates of each connection configuration tested. A larger sample size would have yielded more accurate values for the mechanical properties of the connections.

Due to limitations in the testing equipment, specimens with mixed angle STSs included only two 90° STSs and two 45° STSs (ratio of one). Exploring connections with varying resistance ratio could involve using different combinations of numbers of 90° STSs and 45° STSs in a single specimen.

While the structural models were designed for seismic hazard levels in south western British Columbia, the IDA analysis utilized standard far-field crustal motions from FEMA P695. The adoption of FEMA's records was due to the limited availability of suitable earthquake records that fit the seismic sources in the region and to avoid potential adverse effects from ground motion selection. Future studies could consider the influence of in-slab and interface earthquakes on the seismic response.

In the simulation of structural elements, DowelType and SAWS materials were used in OpenSees. However, an alternative approach could involve exploring the use of a simpler and more practical material, such as Pinching 4, which employs a piece-wise linear formulation for the backbone curve.

Investigating the differences between these materials could be an interesting avenue for future research.

In the design of hybrid buildings, both subsystems were considered to resist half of the design base shear (design resistance ratio of 0.5). Future studies could investigate the impact of different design resistance ratios between the two subsystems on the seismic performance.

References

[1] J. H. Rainer, X. Lu, C. Ni, H. Cheng, M. Follesa, and E. Karacabeyli, “Research program on the seismic resistance of conventional wood-frame construction,” in *Proceedings of the 8th US National Conference on Earthquake Engineering, San Francisco, California, USA*, p. 1203, 2006.

[2] F. Asdrubali, B. Ferracuti, L. Lombardi, C. Guattari, L. Evangelisti, and G. Grazieschi, “A review of structural, thermo-physical, acoustical, and environmental properties of wooden materials for building applications,” *Build. Environ.*, vol. 114, pp. 307–332, 2017.

[3] Y. Li, Bruce R. Ellingwood, “Reliability of woodframe residential construction subjected to earthquakes,” *Structural Safety,* vol. 29, no. 4, pp. 294-307, 2007.

[4] K. Conrad and A. R. Phillips, “Full scale testing and development of wood-steel composite shear walls,” in *Structures*, vol. 20, pp. 268–278, 2019.

[5] Z. Chen, Y. H. Chui, C. Ni, and J. Xu, “Seismic response of midrise light wood-frame buildings with portal frames,” *J. Struct. Eng.*, vol. 140, no. 8, p. A4013003, 2014.

[6] T. Sartori and R. Tomasi, “Experimental investigation on sheathing-to-framing connections in wood shear walls,” *Eng. Struct.*, vol. 56, pp. 2197–2205, 2013.

[7] J. Humbert, C. Boudaud, J. Baroth, S. Hameury, and L. Daudeville, “Joints and wood shear walls modelling I: Constitutive law, experimental tests and FE model under quasi-static loading,” *Eng. Struct.*, vol. 65, pp. 52–61, 2014.

[8] ASTM D7989. Standard Practice for Demonstrating Equivalent In-Plane Lateral Seismic

Performance to Wood-Frame Shear Walls Sheathed with Wood Structural Panels. American Society for Testing and Materials, West Conshohocken, USA, 2018.

[9] G. Di Gangi, C. Demartino, G. Quaranta, and G. Monti, “Dissipation in sheathing-to-framing connections of light-frame timber shear walls under seismic loads,” *Eng. Struct.*, vol. 208, p. 110246, 2020.

[10] A. Aloisio, A. Contento, R. Alaggio, B. Briseghella, and M. Fragiacomo, “Probabilistic assessment of a light-timber frame shear wall with variable pinching under repeated earthquakes,” *J. Struct. Eng.*, vol. 148, no. 11, p. 4022178, 2022.

[11] ASCE/SEI 41-13. Seismic Evaluation and Retrofit of Existing Buildings. American Society of Civil Engineers, Virginia, USA, 2014.

[12] A. Hashemi, P. Zarnani, and P. Quenneville, “Seismic assessment of rocking timber walls with energy dissipation devices,” *Eng. Struct.*, vol. 221, p. 111053, 2020.

[13] J. W. van de Lindt and T. N. Dao, “Performance-based wind engineering for wood-frame buildings,” *J. Struct. Eng.*, vol. 135, no. 2, pp. 169–177, 2009.

[14] L. Zhou, “Structural Response of Mid-rise Hybrid Building System Consisting of a Light Wood Frame Structure and Stiff Core,” University of New Brunswick, 2015.

[15] NRCC. National Building Code of Canada (NBCC 2020). Canadian Commission on Building and Fire Codes -National Research Council of Canada, Ottawa, Canada, 2020.

[16] R. Qiang, L. Zhou, C. Ni, and D. Huang, “Seismic performance of high-capacity light wood frame shear walls with three rows of nails,” *Eng. Struct.*, vol. 268, p. 114767, 2022.

[17] A. Ceccotti, M. P. Lauriola, M. Pinna, and C. Sandhaas, “SOFIE project-cyclic tests on cross-laminated wooden panels,” in *Proceedings of 9th World Conference on Timber Engineering (WCTE2006), Portland*, 2006.

[18] R. DeVall, M. Popovski, and J. B. W. McFadden, “Technical guide for evaluation of seismic force resisting systems and their force modification factors for use in the National Building Code of Canada with concepts illustrated using a cantilevered wood CLT shear wall example,” National Research Council of Canada, Canadian Construction Materials Centre (CCMC), 2021.

[19] A. Eini, L. Zhou, and C. Ni, “Pinching Effect on Seismic Performance of a SDOF Light Wood-Frame Timber Structure,” in *Proceedings of the world conference on timber engineering WCTE, Santiago, Chile*, 2021.

[20] A. Eini, L. Zhou, and C. Ni, “Behavior of Self-Tapping Screws Used in Hybrid Light Wood Frame Structures Connected to a CLT Core,” *Build. 2022, Vol. 12, Page 1018*, vol. 12, no. 7, p. 1018, Jul. 2022.

[21] A. Eini, L. Zhou, and C. Ni, “Cyclic and monotonic test of self-tapping screw connections used in CLT-light wood frame hybrid structures,” in *In Proceeding of the International Conference on New Horizons in Green Civil Engineering*, 2022.

[22] L. H. Lee, S. W. Han, and Y. H. Oh, “Determination of ductility factor considering different hysteretic models,” *Earthq. Eng. Struct. Dyn.*, vol. 28, no. 9, pp. 957–977, 1999.

[23] P. Paevere and G. C. Foliente, “Hysteretic pinching and degradation effects on dynamic response and reliability,” in *Proceedings of the international conference on applications of*

statistics and probability, Sydney, Australia. 2000.

[24] G. C. Foliente, "Hysteresis modeling of wood joints and structural systems," *J. Struct. Eng.*, vol. 121, no. 6, pp. 1013–1022, 1995.

[25] R. A. Medina and H. Krawinkler, "Influence of Hysteretic Behavior on the Nonlinear Response of Frame Structures," in *Proceedings of the 13th world conference on earthquake engineering*, no. 239, 2004.

[26] K. Goda, H. P. Hong, and C. S. Lee, "Probabilistic characteristics of seismic ductility demand of SDOF systems with bouc-wen hysteretic behavior," *J. Earthq. Eng.*, vol. 13, no. 5, pp. 600–622, 2009.

[27] W. Pu and M. Wu, "Ductility demands and residual displacements of pinching hysteretic timber structures subjected to seismic sequences," *Soil Dyn. Earthq. Eng.*, vol. 114, pp. 392–403, 2018.

[28] M. Gebrekirstos Mezgebo, "Estimation of Earthquake Input Energy, Hysteretic Energy and its Distribution in MDOF Structures," 2015.

[29] M. Molazadeh and H. Saffari, "The effects of ground motion duration and pinching-degrading behavior on seismic response of SDOF systems," *Soil Dyn. Earthq. Eng.*, vol. 114, 333–347, 2018.

[30] A. K. Kazantzi and D. Vamvatsikos, "The hysteretic energy as a performance measure in analytical studies," *Earthq. Spectra*, vol. 34, no. 2, pp. 719–739, 2018.

[31] B. McKenna, F., Fenves, G., Scott, H., & Jeremic, "Open System for Earthquake

EngineeringSimulation(OpenSees).” Pacific Earthquake Engineering Research Center, University of California, Berkeley, CA, 2000.

[32] “Exponent PU. SAWS Model (OpenSees User Documentation).” 2010.

[33] J. P. Judd and F. S. Fonseca, “Analytical Model for Sheathing-to-Framing Connections in Wood Shear Walls and Diaphragms,” *J. Struct. Eng.*, vol. 131, no. 2, pp. 345–352, 2005.

[34] D. Fischer, A. Filiatrault, B. Folz, C. M. Uang, and F. Seible, “Shake table tests of a two-story house,” *CUREE Publ. No. W-06,* Richmond, California, 2001.

[35] M. He, F. Lam, and R. O. Foschi, “Modeling three-dimensional timber light-frame buildings,” *J. Struct. Eng.*, vol. 127, no. 8, pp. 901–913, 2001.

[36] G. C. Pardoen, “Testing and analysis of one-story and two-story shear walls under cyclic loading,” *CUREE*, 2003.

[37] J. Xu, “Development of a general dynamic hysteretic light-frame structure model and study on the torsional behavior of open-front light-frame structures, ” vol. 68. Citeseer, 2006.

[38] D. W. Dinehart, R. M. Hoffman, and A. S. Blasetti, “Finite Element Modeling of Wood Shear Walls with VE Polymers,” in *Proceedings of the 9th World Conference on Timber Engineering*, 2006.

[39] S. Pei and J. W. Van de Lindt, “Coupled shear-bending formulation for seismic analysis of stacked wood shear wall systems,” *Earthq. Eng. Struct. Dyn.*, vol. 38, no. 14, pp. 1631–1647, 2009.

[40] F. Germano, G. Metelli, and E. Giuriani, “Experimental results on the role of sheathing-to-frame and base connections of a European timber framed shear wall,” *Constr. Build. Mater.*, vol. 80, pp. 315–328, 2015.

[41] Y. Verdret, C. Faye, S. M. Elachachi, L. Le Magorou, and P. Garcia, “Experimental investigation on stapled and nailed connections in light timber frame walls,” *Constr. Build. Mater.*, vol. 91, pp. 260–273, 2015.

[42] M. J. Mulder, “Numerical modeling of seismic performance of light-frame wood buildings,” University of British Columbia, 2017.

[43] J. M. Branco, F. T. Matos, and P. B. Lourenço, “Experimental in-plane evaluation of light timber walls panels,” *Buildings*, vol. 7, no. 3, p. 63, 2017.

[44] G. C. Foliente, “Issues in seismic performance testing and evaluation of timber structural systems.” 1996.

[45] D. Vamvatsikos and C. A. Cornell, “Incremental dynamic analysis,” *Earthq. Eng. Struct. Dyn.*, vol. 31, no. 3, pp. 491–514, 2002.

[46] FEMA P-695. Quantification of Building Seismic Performance Factors. Federal Emergency Management Agency, Prepared by Applied Technology Council (ATC), Washington, USA., 2009.

[47] C.-T. Yeh, B. J. Hartz, and C. B. Brown, “Damping sources in wood structures,” *J. Sound Vib.*, vol. 19, no. 4, pp. 411–419, 1971.

[48] FEMA P-350. Recommended seismic design criteria for new steel moment-frame buildings.

Federal Emergency Management Agency, SAC Joint Venture, Washington, DC, 2000.

[49] A. S. Veletsos and N. M. Newmark, “Effect of inelastic behavior on the response of simple systems to earthquake motions,” 1960.

[50] A. Polastri, L. Pozza, C. Loss, and I. Smith, “Numerical analyses of high- and medium-rise CLT buildings braced with cores and additional shear walls,” *Struct. Archit.*, pp. 128–136, 2016.

[51] J. W. Van De Lindt and M. Asce, “Evolution of Wood Shear Wall Testing, Modeling, and Reliability Analysis: Bibliography,” *Pract. Period. Struct. Des. Constr.*, vol. 9, no. 1, pp. 44–53, Feb. 2004.

[52] T. T. Nguyen, T. N. Dao, S. Aaleti, J. W. van de Lindt, and K. J. Fridley, “Seismic assessment of a three-story wood building with an integrated CLT-lightframe system using RTHS,” *Eng. Struct.*, vol. 167, pp. 695–704, 2018.

[53] Y. K. Anandan *et al.*, “Experimental Dynamic Testing of Full-Scale Light-Frame-CLT Wood Shear Wall System,” *J. Archit. Eng.*, vol. 27, no. 1, p. 04020042, 2021.

[54] S. Gagnon and E. Karacabeyli, “CLT handbook: Cross-laminated timber,” FPInnovations, 2019.

[55] C. Loss, A. Hossain, and T. Tannert, “Simple cross-laminated timber shear connections with spatially arranged screws,” *Eng. Struct.*, vol. 173, pp. 340–356, 2018.

[56] W. Muñoz, M. Mohammad, S. Gagnon. "Lateral and withdrawal resistance of typical CLT connections." in *Proceedings of the 11th World Conference on Timber Engineering,* Riva

del Garda, Italy. 2010

[57] A. Hossain, M. Popovski, and T. Tannert, “Cross-laminated timber connections assembled with a combination of screws in withdrawal and screws in shear,” *Eng. Struct.*, vol. 168, pp. 1–11, 2018.

[58] T. Roberto, et al. "A new ductile approach design of joints assembled with screw connectors." in *Proceedings of the World Conference on Timber Engineering, Portland, USA*. 2006.

[59] I. Gavric, M. Fragiacomo, and A. Ceccotti, “Cyclic behavior of typical screwed connections for cross-laminated (CLT) structures,” *Eur. J. Wood Wood Prod.*, vol. 73, no. 2, pp. 179–191, 2015.

[60] J. R. Brown, M. Li, T. Tannert, and D. Moroder, “Experimental study on orthogonal joints in cross-laminated timber with self-tapping screws installed with mixed angles,” *Eng. Struct.*, vol. 228, p. 111560, 2021.

[61] ANSI/APA PRG-320. Standard for performance-rated cross laminated timber. APA–The Engineered Wood Association, Tacoma, WA, 2012.

[62] CSA O86-19. Engineering Design in Wood. Canadian Standards Association, Mississauga, Ontario, Canada, 2019.

[63] CCMC 13677-R. Evaluation Report CCMC 13677-R, SWG ASSY® VG Plus and SWG ASSY® 3.0 Self-Tapping Wood Screws. Canadian Construction Materials Centre, Ottawa, Ontario, Canada, 2020.

[64] M. T. C. Solutions, “Structural Screw Design Guide.” Surrey, BC, Canada, 2020.

[65] ASTM D1761. Standard Test Methods for Mechanical Fasteners in Wood and Wood-Based Materials. American Society for Testing and Materials, West Conshohocken, PA, USA, 2020.

[66] ASTM E2126. Standard test methods for cyclic (reversed) load test for shear resistance of vertical elements of the lateral force resisting systems for buildings. American Society for Testing and Materials, West Conshohocken, PA, USA, 2019.

[67] H. Salazar and A. Varum, “Seismic assessment, strengthening and repair of existing buildings.” Universidade de Aveiro, Portugal, 2003.

[68] X. Zhang, M. Shahnewaz, and T. Tannert, “Seismic reliability analysis of a timber steel hybrid system,” *Eng. Struct.*, vol. 167, pp. 629–638, 2018.

[69] B. R. Ellis and A. J. Bougard, “Dynamic testing and stiffness evaluation of a six-storey timber framed building during construction,” *Eng. Struct.*, vol. 23, no. 10, pp. 1232–1242, 2001.

[70] M. He, Q. Luo, Z. Li, H. Dong, and M. Li, “Seismic performance evaluation of timber-steel hybrid structure through large-scale shaking table tests,” *Eng. Struct.*, vol. 175, pp. 483–500, Nov. 2018.

[71] C. Dickof, “CLT infill panels in steel moment resisting frames as a hybrid seismic force resisting system.” University of British Columbia, 2013.

[72] M. Izzi, D. Casagrande, S. Bezzi, D. Pasca, M. Follesa, and R. Tomasi, “Seismic behaviour

of Cross-Laminated Timber structures: A state-of-the-art review," *Eng. Struct.*, vol. 170, pp. 42–52, 2018.

[73] D. Vamvatsikos and A. Cornell, "The incremental dynamic analysis and its application to performance-based earthquake engineering," 2002.

[74] L. Zhou, C. Ni, M. Asce, Y.-H. Chui, Z. Chen, and A. M. Asce, "Seismic Performance of a Hybrid Building System Consisting of a Light Wood Frame Structure and a Reinforced Masonry Core," *J. Perform. Constr. Facil.*, vol. 28, no. 6, 2014.

[75] M. Follesa and M. Fragiacomo, "Force-based seismic design of mixed CLT/Light-Frame buildings," *Eng. Struct.*, vol. 168, pp. 628–642, 2018.

[76] Z. Chen, Y. H. Chui, C. Ni, G. Doudak, and M. Mohammad, "Load Distribution in Timber Structures Consisting of Multiple Lateral Load Resisting Elements with Different Stiffnesses," *J. Perform. Constr. Facil.*, vol. 28, no. 6, p. A4014011, 2014.

[77] S. Tesfamariam, K. Skandalos, K. Goda, M. A. Bezabeh, G. Bitsuamlak, and M. Popovski, "Quantifying the Ductility-Related Force Modification Factor for 10-Story Timber–RC Hybrid Building Using FEMA P695 Procedure and Considering the 2015 NBC Seismic Hazard," *J. Struct. Eng.*, vol. 147, no. 5, p. 4021052, 2021.

[78] C. Ni, L. Zhou, and S. S. Derakhshan, "Experimental study on a new high-capacity shear wall," in *Proceedings of the World Conference on Timber Engineering*, 2021.

[79] J. R. Brown and M. Li, "Structural performance of dowelled cross-laminated timber hold-down connections with increased row spacing and end distance," *Constr. Build. Mater.*, vol.

271, p. 121595, 2021.

[80] S. Rezvani, L. Zhou, and C. Ni, “Experimental evaluation of angle bracket connections in CLT structures under in-and out-of-plane lateral loading,” *Eng. Struct.*, vol. 244, p. 112787, 2021.

[81] D. Mitchell, R. Tremblay, E. Karacabeyli, P. Paultre, M. Saatcioglu, and D. L. Anderson, “Seismic force modification factors for the proposed 2005 edition of the National Building Code of Canada,” *Can. J. Civ. Eng.*, vol. 30, no. 2, pp. 308–327, 2003.

[82] Canadian Wood Council, “Wood design manual,” *Ottawa, Canadá*, 2020.

[83] I. Gavric, M. Fragiacomo, and A. Ceccotti, “Cyclic behaviour of typical metal connectors for cross-laminated (CLT) structures,” *Mater. Struct.*, vol. 48, no. 6, pp. 1841–1857, 2015.

[84] J. D. Dolan, “The dynamic response of timber shear walls.” University of British Columbia, 1989.

[85] F. Seible, A. Filiatrault, and C. M. Uang, “Proc., invitational workshop on seismic testing, analysis and design of woodframe construction,” *CUREE Publ. No. W*, vol. 1, 1999.

[86] B. Folz and A. Filiatrault, “Seismic analysis of woodframe structures. I: Model formulation,” *J. Struct. Eng.*, vol. 130, no. 9, pp. 1353–1360, 2004.

[87] H. Dong, M. He, X. Wang, C. Christopoulos, Z. Li, and Z. Shu, “Development of a uniaxial hysteretic model for dowel-type timber joints in OpenSees,” *Constr. Build. Mater.*, vol. 288, p. 123112, 2021.

[88] X. Sun, M. He, Z. Li, and Z. Shu, “Performance evaluation of multi-storey cross-laminated timber structures under different earthquake hazard levels,” *J. wood Sci.*, vol. 64, no. 1, pp. 23–39, 2018.

Appendix A Incremental Dynamic Analysis Curves of The Study on Pinching Effect of a SDOF Light Wood-Frame Timber Structure

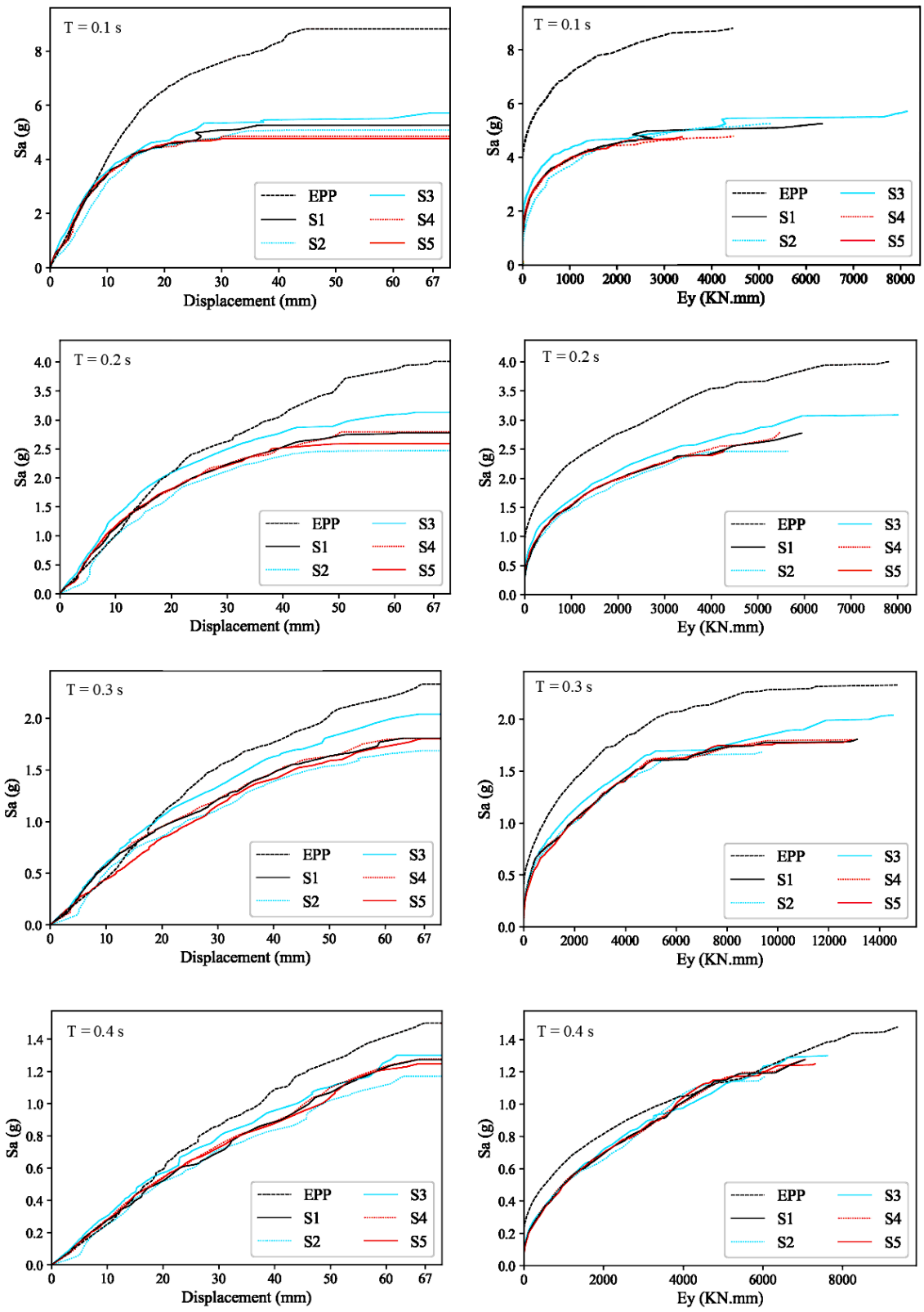

Figure appx. A.1. Median IDA curves of models with periods of 0.1 s to 0.4 s: (left) *Sa* vs displacement; and (right) *Sa* vs *Ey*.

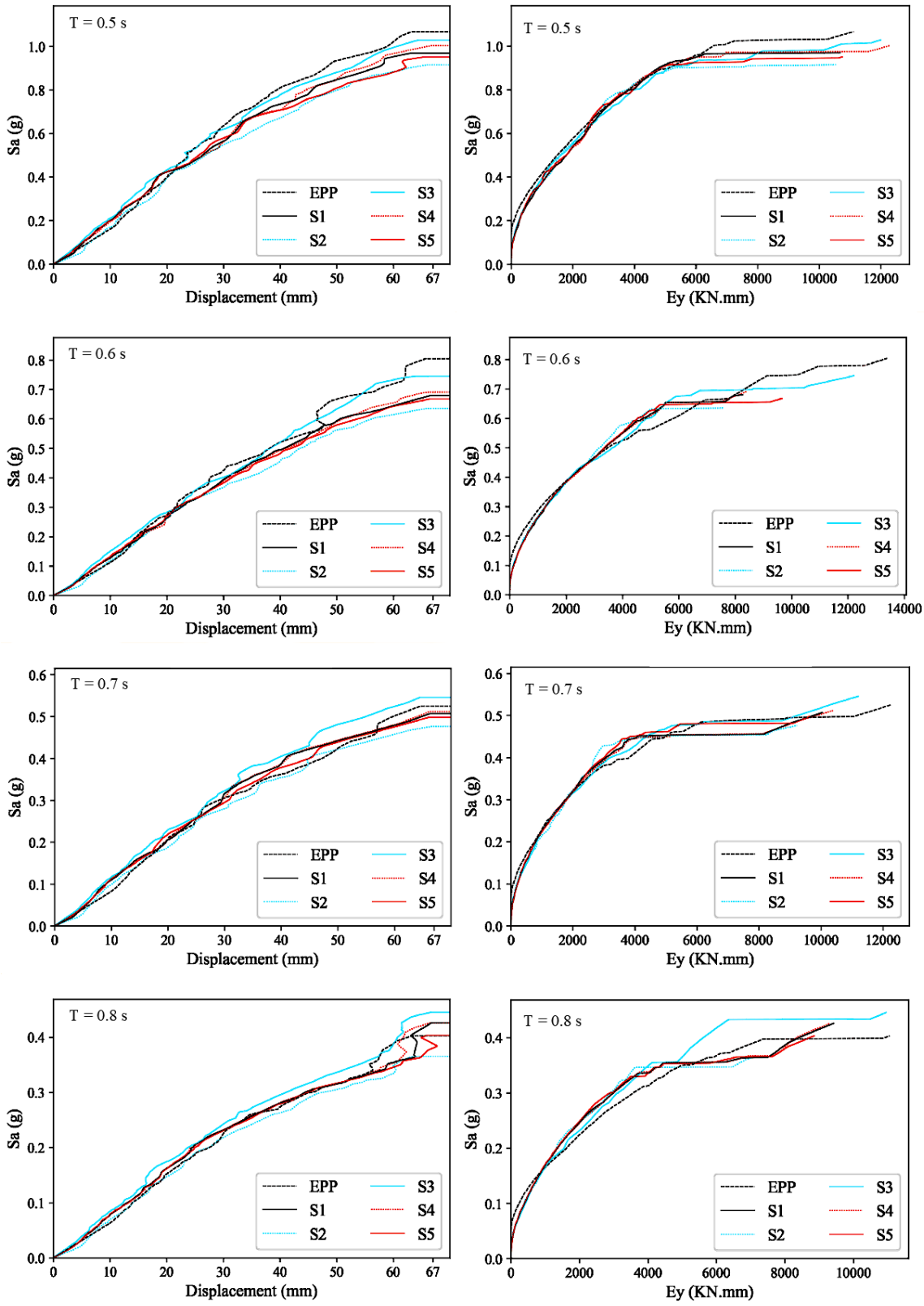

Figure appx. A.2. Median IDA curves of models with periods of 0.5 s to 0.8 s: (left) *Sa* vs displacement; and (right) *Sa* vs *Ey*.

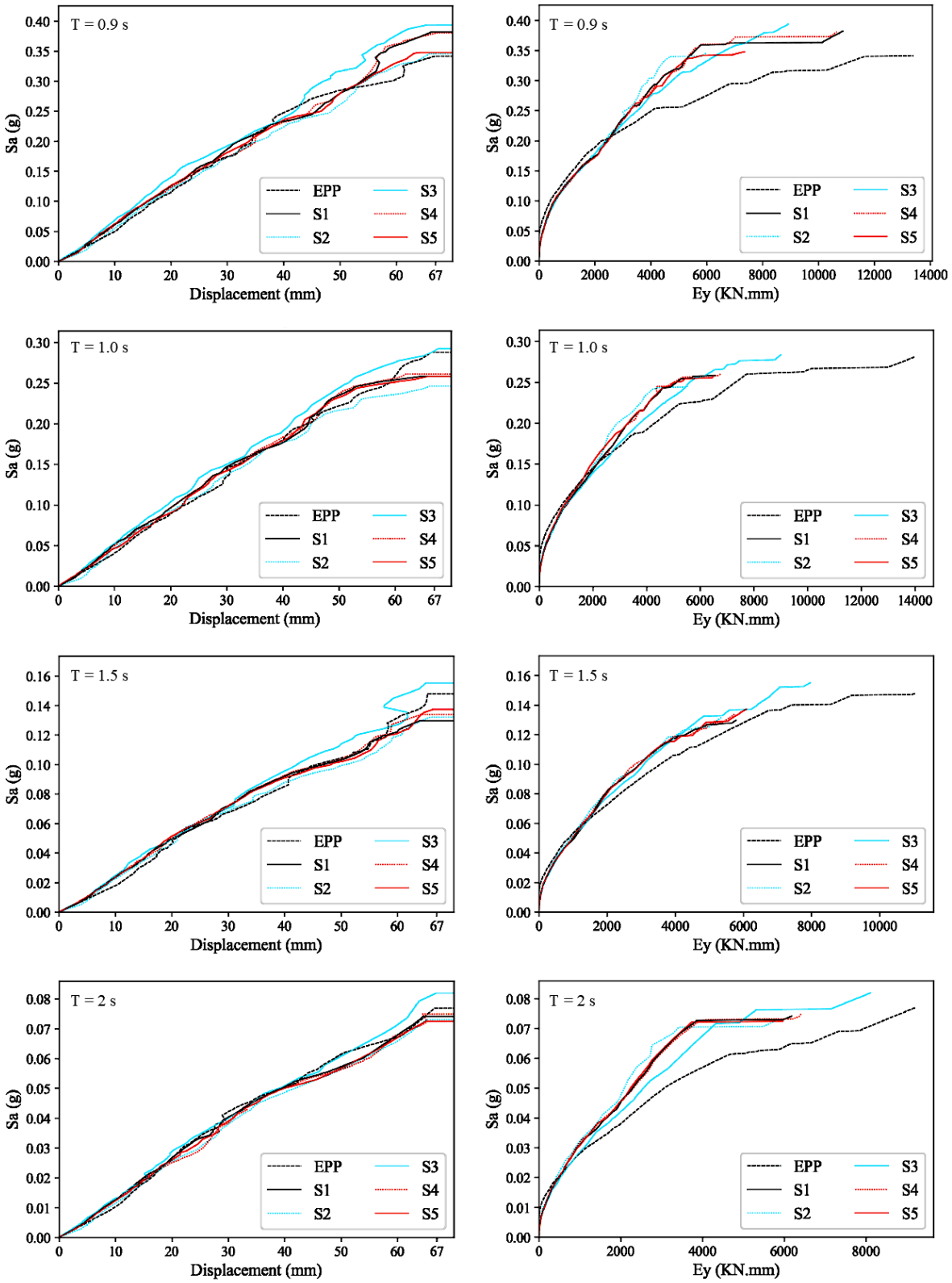

Figure appx. A.3. Median IDA curves of models with periods of 0.9 s to 2.0 s: (left) *Sa* vs displacement; and (right) *Sa* vs *Ey*.

Appendix B Reversed-Cyclic Test Results of the Self-Tapping Screw Connection in a Hybrid LWF/CLT Structure

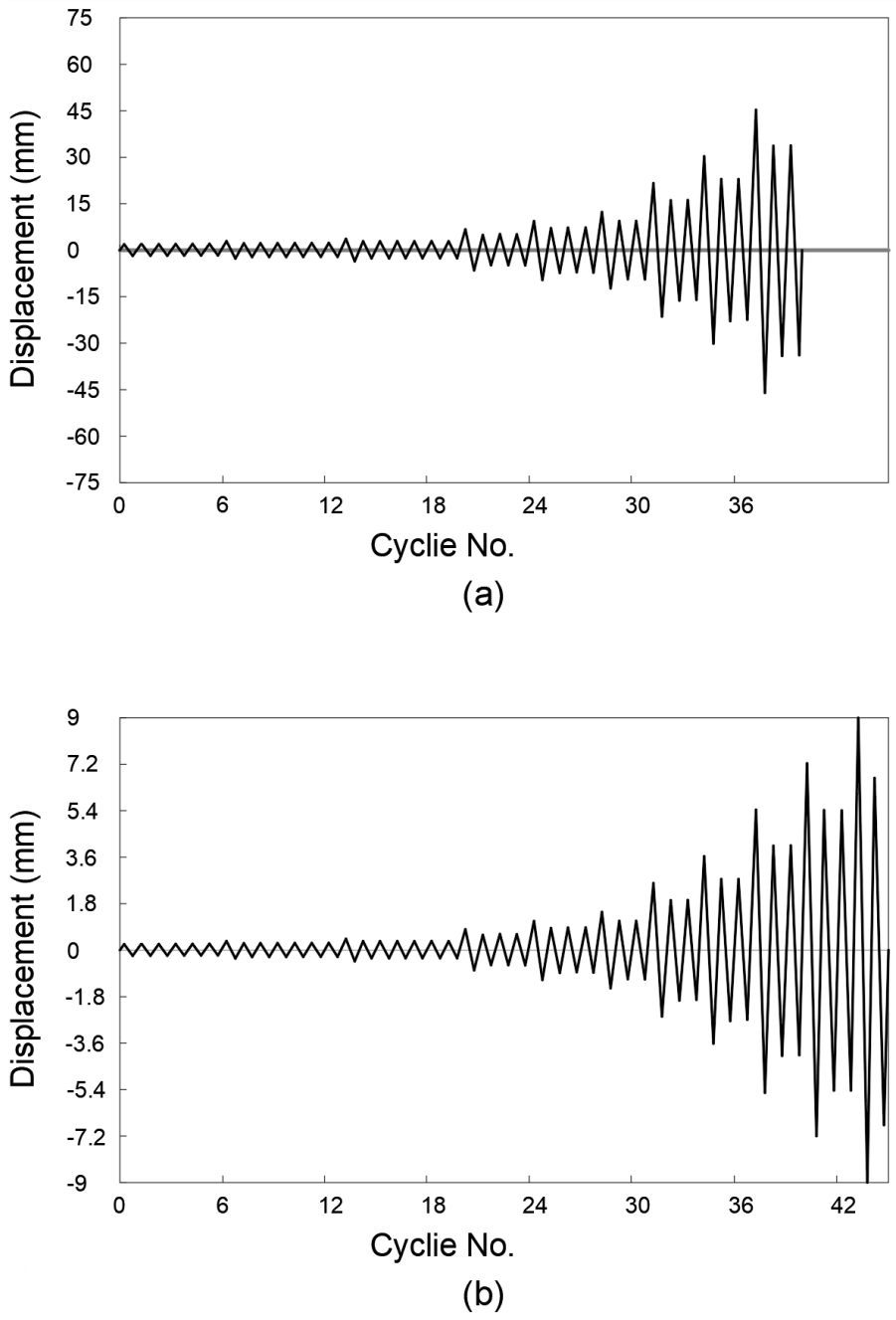

Figure appx. B.1. Loading protocols: (a) 90° STS and mixed angle (45° + 90°) connections with a target displacement of 30 mm; and (a) 45° STS connections with a target displacement of 3.6 mm.

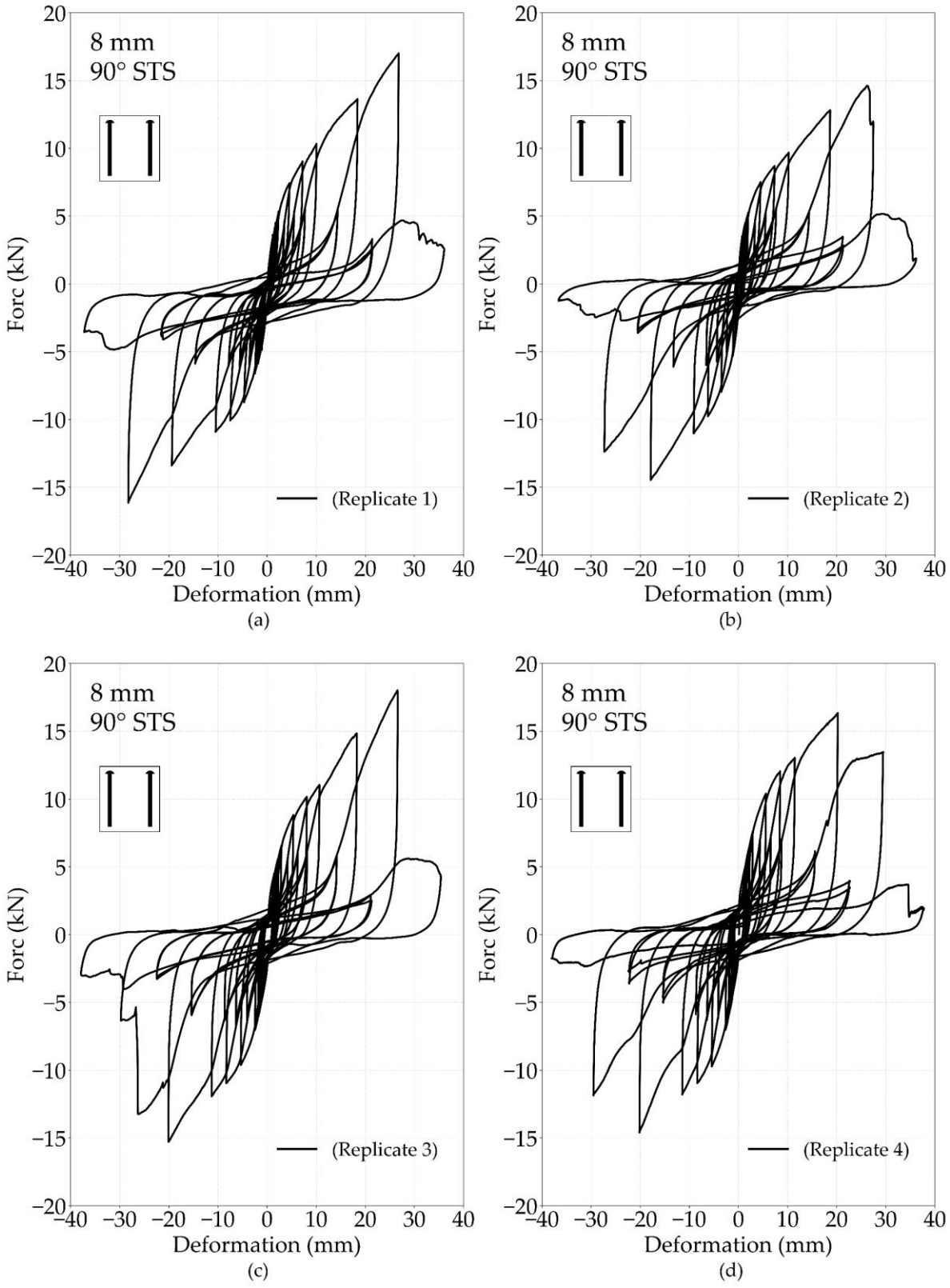

Figure appx. B.2. Load-displacement curves for 8 mm STSs (90°): (a) replicate 1; (b) replicate 2; (c) replicate 3; and (d) replicate 4.

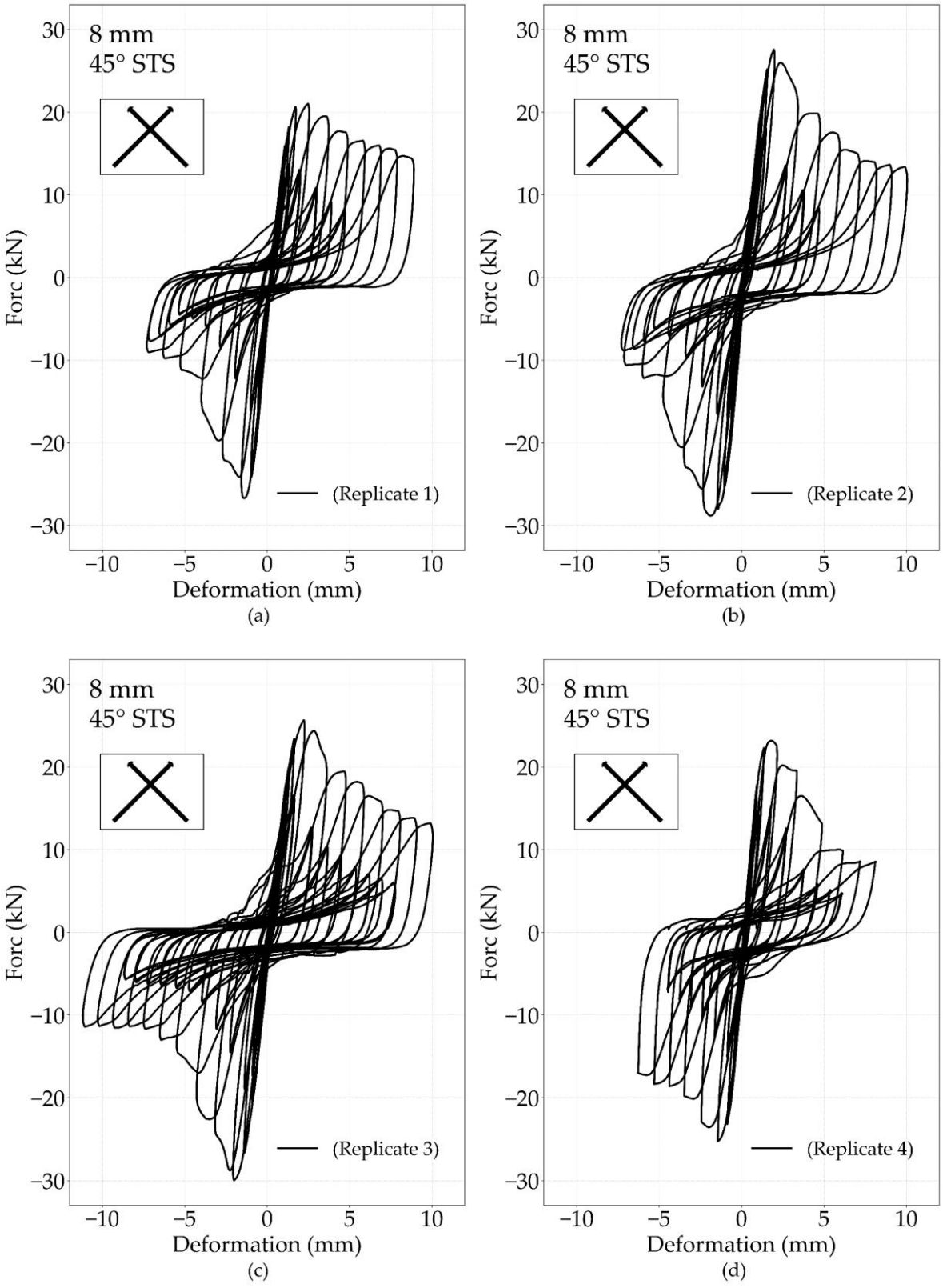

Figure appx. B.3. Figure appx. B.1. Load-displacement curves for 8 mm STSs (45°): (a) replicate 1; (b) replicate 2; (c) replicate 3; and (d) replicate 4.

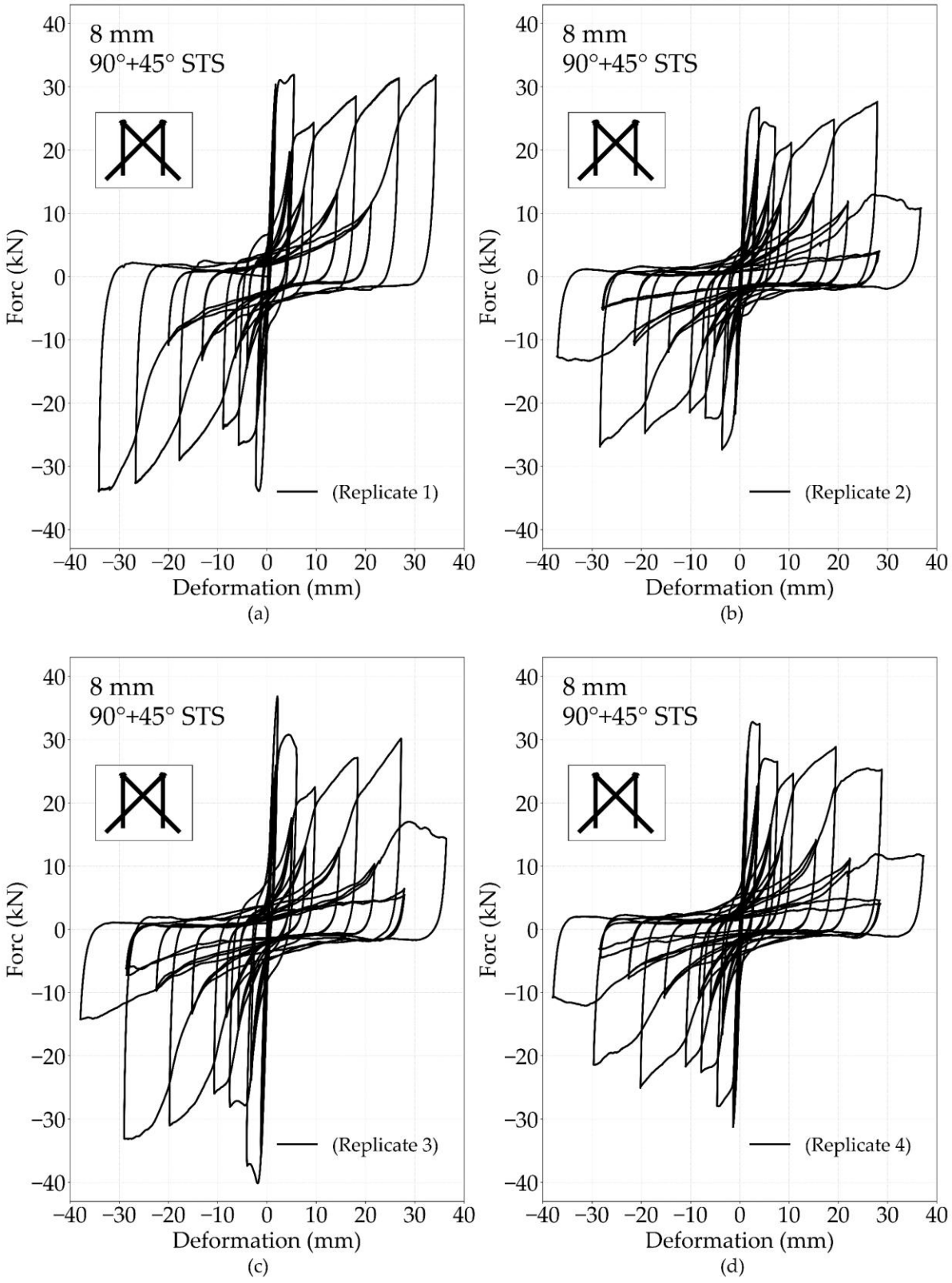

Figure appx. B.4. Load-displacement curves for 8 mm STSs (mixed angle (45° + 90°)): (a) replicate 1; (b) replicate 2; (c) replicate 3; and (d) replicate 4.

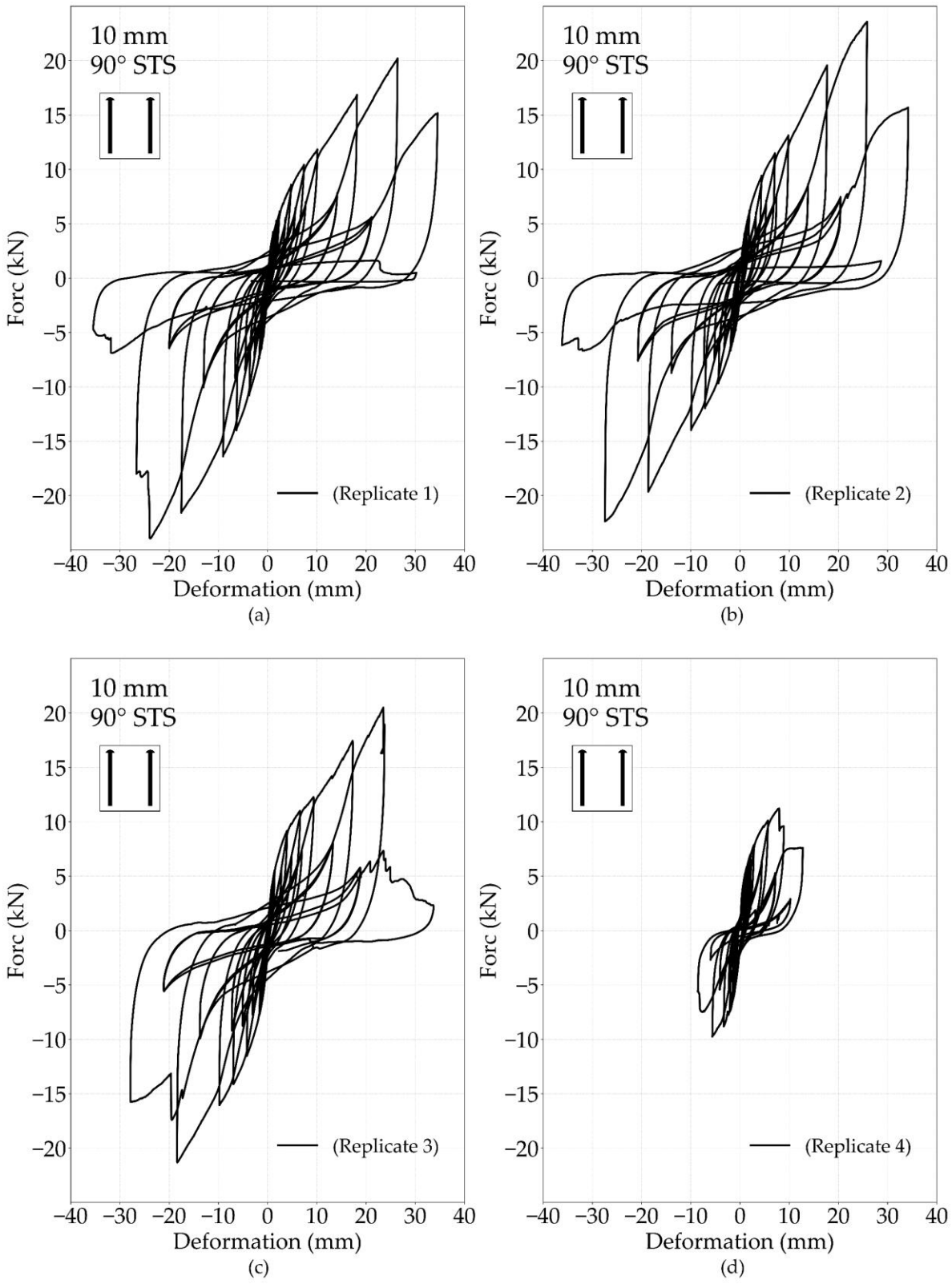

Figure appx. B.5. Load-displacement curves for 10 mm STSs (90°): (a) replicate 1; (b) replicate 2; (c) replicate 3; and (d) replicate 4.

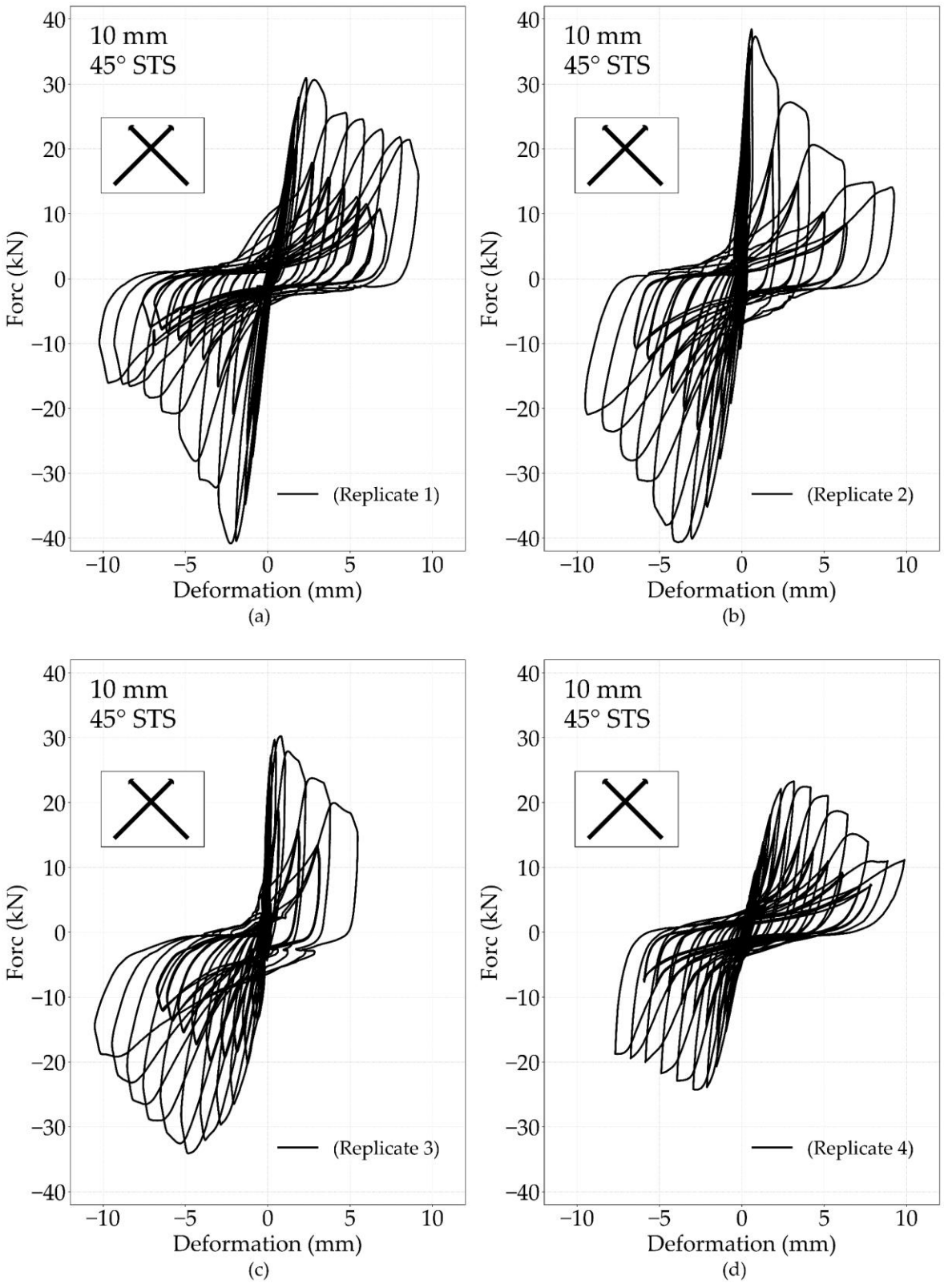

Figure appx. B.6. Load-displacement curves for 10 mm STSs (45°): (a) replicate 1; (b) replicate 2; (c) replicate 3; and (d) replicate 4.

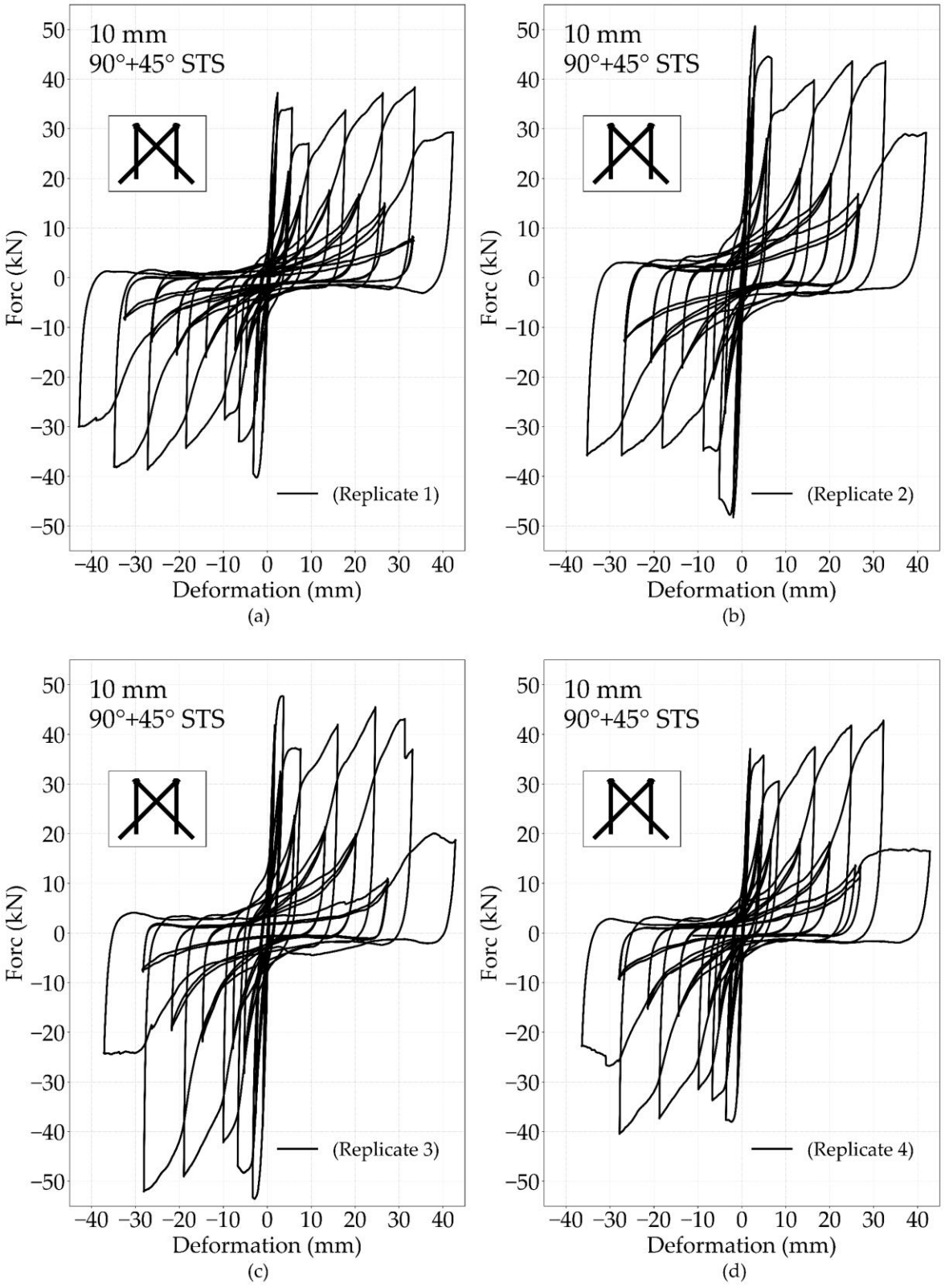

Figure appx. B.7. Load-displacement curves for 10 mm STSs (mixed angle (45° + 90°)): (a) replicate 1; (b) replicate 2; (c) replicate 3; and (d) replicate 4.

Appendix C Design of Archetypes Consisting of a Light Wood Frame Structure and Balloon-Type CLT Core

1. Building Description

The structures are assumed to be located in Vancouver on site of Class C. The height of each storey of is 2.8 m. There are five configurations considered for the hybrid LWF/CLT study. Case A is a pure LF system and the CLT core is not structurally connected to the floor. Case B, C and D are a combination of LF walls and balloon-type CLT core with 45° STS, 90° STS and mixed-angle STS connection between subsystems, respectively. Case E is the configuration with only the CLT core as lateral load-resisting system. The shear wall layout on each floor of these buildings is the same as shown in **Figure appx. C.1**. Only the shear walls along E-W direction are designed in this study. The floor diaphragm is assumed to be rigid. Each case is designed in 1,4 and 6-storey archetypes.

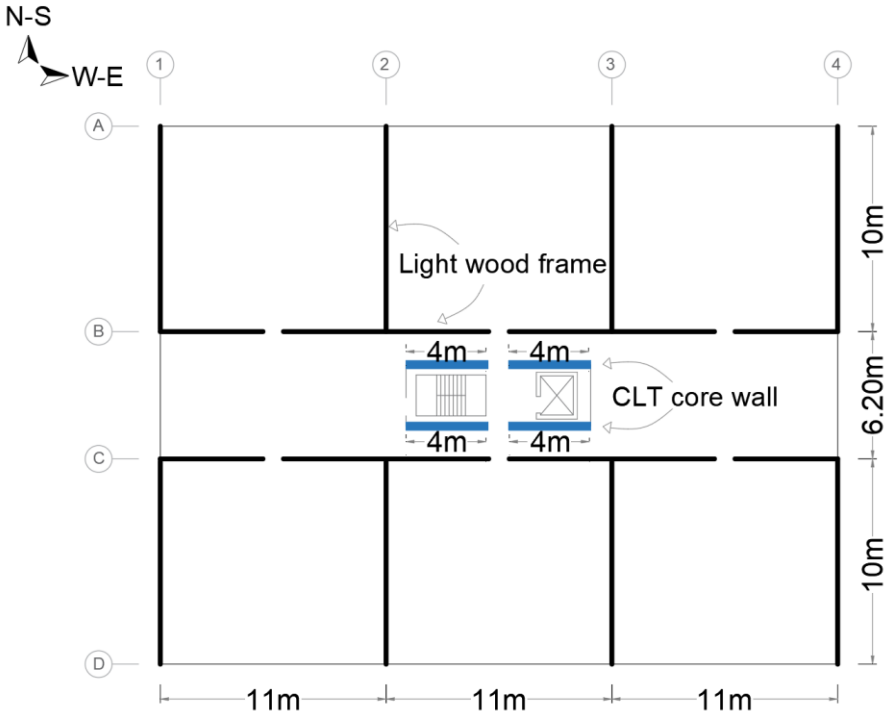

Figure appx. C.1. Layout of the hybrid building containing LF wood shear walls and CLT core wall.

2. Design Seismic Load

Archetypes were designed according to Article 4.1.8. Earthquake Load and Effects of National Building Code of Canada (2020) [15].

Importance Category: Normal (Table 4.1.8.5.-A of NBCC 2020)
Site Class: C (Table 4.1.8.4.-B of NBCC 2020)

Dead loads

Roof: $D_r = 0.7$ kPa

Floor: $D_f = 1.3$ kPa

Partition: $D_p = 0.5$ kPa (Article 4.1.8.2 2020)

Snow Load: (Article 4.1.6.2 and Table C-2 in Appendix C of NBCC 2020)

Ultimate limit state $\rightarrow S = I_s[S_s(C_b\ C_w\ C_s\ C_a) + S_r] = 1 \times [1.1 \times (0.8 \times 1 \times 1 \times 1) + 0.2] = 1.08$ kPa

Seismic Weight

Floor area: $A = 0.25 \times (33 \times 26.2) = 216\ m^2$ (Only a quarter of the layout was considered in FEM)

Roof weight: $W_r = A\ (0.25S + D_r + 0.5\ D_p) = 216\ m^2\ (0.25 \times 1.08 + 0.7 + 0.5 \times 0.5) = 264$ kN

Floor weight: $W_f = A\ (D_f + 0.5\ D_p) = 216\ m^2\ (1.3 + 0.5) = 389$ kN

1-storey building: $W_1 = W_r + 3W_f = 264 = 264$ kN

4-storey building: $W_4 = W_r + 3W_f = 264 + 3 \times 389 = 1431$ kN

6-storey building: $W_5 = W_r + 5W_f = 264 + 5 \times 389 = 2209$ kN

5%-Damped Spectral Acceleration (Table C-2 in Appendix C of NBCC 2020)

$S_a\ (0.2, X_C) = 1.09g$, $S_a\ (0.5, X_C) = 0.876g$, $S_a\ (1, X_C) = 0.508g$, $S_a\ (2, X_C) = 0.309g$, $S_a\ (5, X_C) = 0.087g$, $PGA(X_C) = 0.53g$

Design Spectrum (Table 4.1.8.4.-C)

$S(\leq 0.2) = 1.09g$, $S(0.5) = 0.876g$, $S(1) = 0.508g$, $S(2) = 0.309g$, $S(5) = 0.087g$

Empirical Fundamental Period (Article 4.1.8.11.3) c) of NBCC 2020)

1-storey building: $T_a = 0.05(h)^{0.75} = 0.05 \times (2.8)^{0.75} = 0.11$

4-storey building: $T_a = 0.05(h)^{0.75} = 0.05 \times (11.2)^{0.75} = 0.31$

6-storey building: $T_a = 0.05(h)^{0.75} = 0.05 \times (16.85)^{0.75} = 0.41$

Two times the empirical period was used for design. (Article 4.1.8.11.3) d) iii) of NBCC 2020)

1-storey building: $2T_a = 2\times 0.11 = 0.22$

4-storey building: $2T_a = 2\times 0.31 = 0.62$

6-storey building: $2T_a = 2\times 0.41 = 0.82$

Design Spectral Response Acceleration

Linear regression:

1-storey building: $S(0.22) = 1.09 + (0.22 - 0.2) \times (1.09 - 0.876) / (0.2 - 0.5) = 1.08$

4-storey building: $S(0.62) = 0.876 + (0.62 - 0.5) \times (0.876 - 0.508) / (0.5 - 1) = 0.79$

6-storey building: $S(0.82) = 0.876 + (0.82 - 0.5) \times (0.876 - 0.508) / (0.5 - 1) = 0.64$

Seismic Force Modification Factors (Table 4.1.8.9 of NBCC 2020)

Light wood-frame construction: $R_d = 3$, $R_o = 3$

CLT core wall system: $R_d = 2$, $R_o = 1.5$

Hybrid archetypes:

- Case B → $R_d = 2$, $R_o = 1.5$
- Case C → $R_d = 2$, $R_o = 1.5$
- Case D → $R_d = 2.5$, $R_o = 1.5$

The R values for hybrid archetypes showed above have met the acceptance criteria of CCMC.

Base Shear

The Higher Mode Factor, M_v, (Table 4.1.8.11) and Importance Factor for Earthquake Loads and Effects, I_E, (Table 4.1.8.5) are all unity for 4-, 6- and 8-storey buildings.

By Article 4.1.8.11, $V = S(T_a)\, M_v\, I_E\, W/(R_d R_o)$

But *V* shall not be less than $S(4.0)\, M_v\, I_E\, W/(R_d R_o) = 0.16\, W/(R_d R_o)$

and *V* need not be greater than maximum of $(2/3)\, S(0.2)\, I_E\, W/(R_d R_o) = 0.73\, W/(R_d R_o)$ and $S(0.5)\, I_E\, W/(R_d R_o) = 0.876\, W/(R_d R_o)$.

In order to maintain the design values proportional to the design spectrum, no modification was made based on this recommendation.

1-storey building: $V_d = S(0.22)\, W_1 / (R_d R_o) = 1.08 \times 264 / (R_d R_o) = 283.7 / (R_d R_o)$

4-storey building: $V_d = S(0.62)\ W_4 / (R_d R_o) = 0.79 \times 1431 / (R_d R_o) = 1127.1 / (R_d R_o)$

6-storey building: $V_d = S(0.82)\, W_6 / (R_d R_o) = 0.64 \times 2209 / (R_d R_o) = 1414.9 / (R_d R_o)$

Design base shears (V_d) are listed for each archetype in **Table appx C-1**.

Table appx C-1. Design base shear of each archetype.

Configuration	**R_o**	**R_d**	**1-storey V_d (kN)**	**4-storey V_d (kN)**	**6-storey V_d (kN)**
Case A	1.7	3	55.6	221.0	277.4
Case B	1.5	2	94.5	375.7	471.6
Case C	1.5	2	94.5	375.7	471.6
Case D	1.5	2.5	75.6	300.6	377.3
Case E	1.5	2	94.5	375.7	471.6

3. Equivalent Lateral Force

The empirical fundamental period (T_a) for all archetypes are less than 0.7 sec. therefore, $F_t = 0$ and the shear load distribution is obtained by the following equation for each storey. (Article 4.1.8.11.7))

Table appx C-2, 3 and 4 list the lateral load distribution in 1-storey, 4-storey and 6-storey archetypes, respectively.

$F_i = (V - F_t)\, W_i\, h_i / (\sum^{n}_{i=1} W_i\, h_i)$

Table appx C-2. Equivalent earthquake lateral load distribution and storey shear force of 1-storey archetypes.

	R_d = 3, R_o = 1.7 (Case A1)					R_d = 2.5, R_o = 1.5 (Case D1)					R_d = 2, R_o = 1.5 (Case B1, C1 and E1)				
Level	W_i (kN)	h_i (m)	$W_i.h_i$ (kN.m)	F_i (kN)	V_i (kN)	W_i (kN)	h_i (m)	$W_i.h_i$ (kN.m)	F_i (kN)	V_i (kN)	W_i (kN)	h_i (m)	$W_i.h_i$ (kN.m)	F_i (kN)	V_i (kN)
1	263.7	2.8	738.4	55.6	55.6	263.7	2.8	738.4	75.6	75.6	263.7	2.8	738.4	94.6	94.6

Table appx C-3. Equivalent earthquake lateral load distribution of 4-storey archetypes.

	R_d = 3, R_o = 1.7 (Case A4)					R_d = 2.5, R_o = 1.5 (Case D4)					R_d = 2, R_o = 1.5 (Case B4, C4 and E4)				
Level	W_i (kN)	h_i (m)	$W_i.h_i$ (kN.m)	F_i (kN)	V_i (kN)	W_i (kN)	h_i (m)	$W_i.h_i$ (kN.m)	F_i (kN)	V_i (kN)	W_i (kN)	h_i (m)	$W_i.h_i$ (kN.m)	F_i (kN)	V_i (kN)
4	263.7	11.2	2953.5	68.8	68.8	263.7	11.2	2953.5	93.5	93.5	263.7	11.2	2953.5	116.9	116.9
3	389.1	8.4	3268.2	76.1	144.9	389.1	8.4	3268.2	103.5	197.1	389.1	8.4	3268.2	129.4	246.3
2	389.1	5.6	2178.8	50.7	195.6	389.1	5.6	2178.8	69.0	266.1	389.1	5.6	2178.8	86.3	332.6
1	389.1	2.8	1089.4	25.4	221.0	389.1	2.8	1089.4	34.5	300.6	389.1	2.8	1089.4	43.1	375.7

Table appx C-4. Equivalent earthquake lateral load distribution of 6-storey archetypes.

	R_d = 3, R_o = 1.7 (Case A6)					R_d = 2.5, R_o = 1.5 (Case D6)					R_d = 2, R_o = 1.5 (Case B6, C6 and E6)				
Level	W_i (kN)	h_i (m)	$W_i.h_i$ (kN.m)	F_i (kN)	V_i (kN)	W_i (kN)	h_i (m)	$W_i.h_i$ (kN.m)	F_i (kN)	V_i (kN)	W_i (kN)	h_i (m)	$W_i.h_i$ (kN.m)	F_i (kN)	V_i (kN)
6	263.7	16.8	4430.2	59.2	59.2	263.7	16.8	4430.2	80.5	80.5	263.7	16.8	4430.2	100.6	100.6
5	389.1	14.0	5447.0	72.8	131.9	389.1	14.0	5447.0	98.9	179.4	389.1	14.0	5447.0	123.7	224.3
4	389.1	11.2	4357.6	58.2	190.1	389.1	11.2	4357.6	79.2	258.6	389.1	11.2	4357.6	98.9	323.2
3	389.1	8.4	3268.2	43.7	233.8	389.1	8.4	3268.2	59.4	317.9	389.1	8.4	3268.2	74.2	397.4
2	389.1	5.6	2178.8	29.1	262.9	389.1	5.6	2178.8	39.6	357.5	389.1	5.6	2178.8	49.5	446.9
1	389.1	2.8	1089.4	14.6	277.4	389.1	2.8	1089.4	19.8	377.3	389.1	2.8	1089.4	24.7	471.6

As an example, **Figure appx. C.2** (a) and (b) shows a schematic diagram of lateral force in multistorey archetypes of pure LF construction (case A) and CLT-core wall system (case E), respectively. The earthquake force is equally shared between the two subsystems in hybrid cases and is shown in **Figure appx. C.2** (c). In multistory buildings, vertical distribution of equivalent static force follows the fundamental mode. The distribution is commonly represented by an inverted force triangle in seismic design codes. In hybrid structures, each storey of the light wood-frame subsystems (LWF) was designed for the cumulative equivalent static forces applied on that

storey and all the storeys above (Figure C.2. (c)). The other half of the inverted triangle storey force was transmitted to the CLT core through the connections between the two-subsystems. Therefore, the design force on each story of the connections was assumed to be equal to half of the story force of the hybrid buildings.

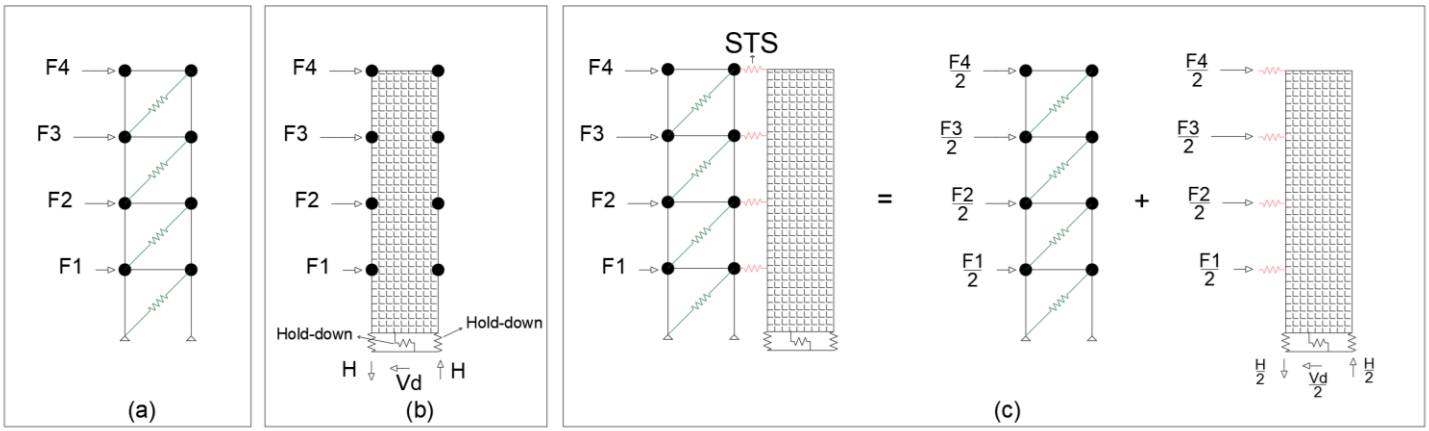

Figure appx. C.2. Design load distribution in 4-storey archetypes: (a) Pure LF construction (case A4); (b) Pure CLT core wall (case E4); and (c) Hybrid system (case B4, C4 and D4).

Shear design force for the i^{th} storey of the n storey light wood-frame system:

$$V_{d,\ hybrid,\ LWF}(i^{th}) = \sum_{i}^{n} F_i\ /2$$

Shear design force for the connection on the i^{th} storey of the n storey hybrid structure:

$$V_{d,\ hybrid,\ Conn}(i^{th}) = F_i\ /2$$

4. Shear Connector and Hold-Down Design

To limit the damage in shear connector and allow the hold-downs to dissipate energy, the design base shear is adjusted by $\gamma = 1.5$ to obtain the shear connector's design force (V_{sc}). The design values are listed in **Table appx C-5**.

- Case B, C and D $\rightarrow V_{sc,\ hybrid} = \gamma \times (V_{d,\ hybrid} / 2) = 0.75\ V_{d,\ hybrid}$
- Case E $\rightarrow V_{sc,\ pure} = \gamma \times (V_{d,\ pure}) = 1.5\ V_{d,\ pure}$

Table appx C-5. Design force of shear connectors.

Configuration	Description	1-storey $V_{sc,1}$ (kN)	4-storey $V_{sc,4}$ (kN)	6-storey $V_{sc,6}$ (kN)
Case B	Hybrid with 45° STS connection	70.9	281.8	353.7
Case C	Hybrid with 90° STS connection	70.9	281.8	353.7
Case D	Hybrid with mixed-angle STS connection	56.7	225.5	283.0
Case E	Pure CLT core wall system	141.8	563.6	707.4

The axial design force of hold-downs (H) is obtained using the overturning moment and shown in **Table appx C-6** to **Table appx C-8**.

$M_f = \sum^{n}_{i=1} F_i \, h_i$

$H = M_f \, (L\text{-}2a)$, $\quad [L = 4 \text{ m}], [a = 0.4 \text{ m}]$

Where M_f is the overturning moment, L is the CLT wall length and a is the distance from the hold-down to the wall edge. In hybrid cases, (H/2) is the hold-down design force.

Table appx C-6. Design axial force of hold-downs of 1-storey archetypes.

	Case B1 and C1					Case D1					Case E1				
Level	h_i (m)	F_i (kN)	$F_i.h_i$ (kN.m)	M_f (kN.m)	H (kN)	h_i (m)	F_i (kN)	$F_i.h_i$ (kN.m)	M_f (kN.m)	H (kN)	h_i (m)	F_i (kN)	$F_i.h_i$ (kN.m)	M_f (kN.m)	H (kN)
1	2.8	47.3	132.4	132.4	41.4	2.8	37.8	105.9	105.9	33.1	2.8	94.6	264.8	264.8	82.7

Table appx C-7. Design axial force of hold-downs of 4-storey archetypes.

	Case B4 and C4					Case D4					Case E4				
Level	h_i (m)	F_i (kN)	$F_i.h_i$ (kN.m)	M_f (kN.m)	H (kN)	h_i (m)	F_i (kN)	$F_i.h_i$ (kN.m)	M_f (kN.m)	H (kN)	h_i (m)	F_i (kN)	$F_i.h_i$ (kN.m)	M_f (kN.m)	H (kN)
4	11.2	58.5	654.8	-	-	11.2	46.8	523.8	-	-	11.2	116.9	1309.6	-	-
3	8.4	64.7	543.4	-	-	8.4	51.8	434.7	-	-	8.4	129.4	1086.8	-	-
2	5.6	43.2	241.5	-	-	5.6	34.5	193.2	-	-	5.6	86.3	483.0	-	-
1	2.8	21.6	60.4	1500.1	468.8	2.8	17.3	48.3	1200.1	375.0	2.8	43.1	120.8	3000.2	937.6

Table appx C-8. Design axial force of hold-downs of 6-storey archetypes.

	Case B6 and C6					Case D6					Case E6				
Level	h_i (m)	F_i (kN)	$F_i.h_i$ (kN.m)	M_f (kN.m)	H (kN)	h_i (m)	F_i (kN)	$F_i.h_i$ (kN.m)	M_f (kN.m)	H (kN)	h_i (m)	F_i (kN)	$F_i.h_i$ (kN.m)	M_f (kN.m)	H (kN)
6	16.8	50.3	845.0	-	-	16.8	40.3	676.0	-	-	16.8	100.6	1689.9	-	-
5	14.0	61.9	865.7	-	-	14.0	49.5	692.6	-	-	14.0	123.7	1731.5	-	-
4	11.2	49.5	554.1	-	-	11.2	39.6	443.3	-	-	11.2	98.9	1108.1	-	-
3	8.4	37.1	311.7	-	-	8.4	29.7	249.3	-	-	8.4	74.2	623.3	-	-
2	5.6	24.8	138.5	-	-	5.6	19.8	110.8	-	-	5.6	49.5	277.0	-	-
1	2.8	12.4	34.6	2749.6	859.2	2.8	9.9	27.7	2199.7	687.4	2.8	24.7	69.3	5499.1	1718.5

5. CLT Panel Design

The factored edgewise bending moment resistance ($M_{r,e}$) and the effective edgewise bending stiffness, ($EI_{eff,e}$) values shall be based on the effective width in edgewise bending ($b_{eff,e}$) and depth of the panel (d). (Clause 7.5.6.5 of CSA O86:19).

Calculations are based on S-P-F MSR 1950 F-1.7E lumber (f_b = 28.2 MPa, E = 11 700 MPa) for loading perpendicular to outermost layers. Since the CLT core is decoupled from gravity system and does not carry vertical loads, the design for interaction of combined bending and axial loads were ignored. The CLT panels layup for each configuration is shown in **Table appx C-9**.

Design of 6-storey archetype of case E configuration is presented as an example:

CLT panel: 7-Ply with a total width of 245 mm

L = 6 × 2.8 m = 16.8 m (wall length)

$b_{eff,e}$ = 5 (layers) × 35 mm = 175 mm (effective width in edgewise bending)

d = 4 m (wall depth)

- Bending resistance

  Factored bending resistance is the lesser of M_{r1} and M_{r2}.

  $M_{r1} = \phi F_b S K_x K_{Zbg}$

$M_{r2} = \phi F_b S K_x K_L$

Where ϕ= 0.9, f_b = 28.2, $F_b = f_b (K_D K_H K_{sb} K_T)$, d = 4 m, S = $b_{eff,e}$ $d^2/6$,

$K_{Zbg} = (130 / b_{eff,e})^{0.1} (610 / d)^{0.1} (9100 / L)^{0.1}$, L = 2.8 m (1-storey), K_x = 1, K_L = 1(out of plane displacement is restrained)

Therefore, M_{r1} = 0.9 × 28.2 (1.15×1×1×1) × 175 × $4^2/6$ × 1 × $(130 / 175)^{0.1}$ $(610 / 4000)^{0.1}$ $(9100 / 16800)^{0.1}$ = 10303 × 10^6 N.mm = 10303 kN.m and

M_{r2} = 0.9 × 28.2 (1.15×1×1×1) × 175 × $4^2/6$ × 1 × 1 = 13620 × 10^6 N.mm = 13620 kN.m

M_r = Minimum (10303, 13620) = 10303 kN.m

M_f = 8798 kN.m < M_r ☑

- Shear resistance

  The factored edgewise shear resistance values, $V_{r,e}$, are based on the gross cross-sectional area of the panel and calculated using the specified edgewise shear strength, $f_{v,e}$. (Clause 7.5.7.3b) of CSA 086:19)

  $V_{r,e} = \phi F_v 2A_g / 3 = \phi f_{v,e,0} (K_D K_H K_{sv} K_T) 2A_g / 3$ = 0.9 × 2.4 × (1.15×1×1×1) × 245 × 4000 = 1525.7 × 10^3 N = 1525.7 kN

  V_f = 754.6 kN < $V_{r,e}$ ☑

Table appx C-9. CLT panel design.

	R_d = 2, R_o = 1.5 (Case B and C)	R_d = 2.5, R_o = 1.5 (Case D)	R_d = 2, R_o = 1.5 (Case E)
1-storey	Layup[1]:105-3s	Layup :105-3s	Layup :105-3s
4-storey	Layup :105-3s	Layup :105-3s	Layup :175-5s
6-storey	Layup :175-5s	Layup :175-5s	Layup :245-7s

[1] Thickness and orientation of layers: (105-3s) = 35L-35T-35L, (175-5s) = 35L-35T-35L-35T-35L, (245-7s) = 35L-35T-35L-35T-35L-35T-35L

35 = 35mm, L = longitudinal, T= Transversal

6. Hysteretic Models Used in OpenSees

SAWS uniaxial material [32]: This material was used in modeling the light wood-frame shear walls.

Table appx C-10. Parameters used in SAWS model.

Group	Parameter	Description
Hysteresis	*FI*	(Residual strength) Intercept strength of the pinching branch of the hysteretic curve
	R3	Stiffness ratio of the unloading branch off the envelope curve. The slope of this line is R3 S0.
	R4	Stiffness ratio of the pinching branch. The slope of this line is R4 S0.
Degradation	*α*	Stiffness degradation parameter.
	ß	Stiffness degradation parameter.
Envelope	*S0*	Initial stiffness of the spring element.
	R1	Stiffness ratio of the asymptotic line to envelope curve. The slope of this line is R1 S0.
	R2	Stiffness ratio of the descending branch of the envelope curve. The slope of this line is R2 S0.
	F0	Intercept strength for the asymtotic line to the envelope curve.
	DU	Displacement at ultimate load

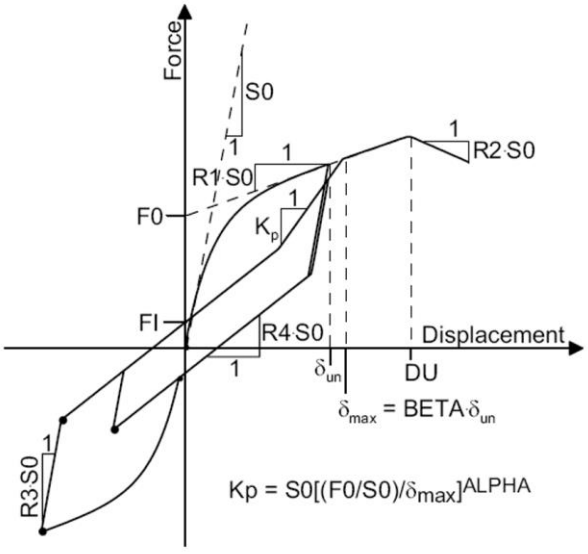

Figure appx. C.3. SAWS model.

DowelType uniaxial material [87]: This material was used in modeling the connections.

Table appx C-11. Parameters of DowelType model.

Group	Parameter	Description
Hysteresis	F_{I0}	Intercept strength of the pinching branch of the hysteretic curve
	K_{p0}	Pinching branch stiffness
	K_{u0}	Unloading stiffness to initial stiffness ratio
	C	Curve shape factor
Degradation	ß	Reloading target displacement amplification factor
	γ	Reloading degradation factor due to energy dissipation
	η	Pinching intercept moving parameter
	D_y	Apparent yielding displacement
	a_p	Pinching stiffness degradation factor
	a_u	Unloading stiffness degradation factor
	a_r	Reloading stiffness degradation factor
Envelope	D_{b1}	Displacement of the first controlling point
(Bézier curve)	F_{b1}	Force of the first controlling point
	D_{b2}	Displacement of the second controlling point
	F_{b2}	Force of the second controlling point
	D_c	Displacement of the cap point
	F_c	Force of the cap point
	K_d	Descending absolute stiffness
	D_u	Ultimate displacement
Envelope	D_1	Displacement of interpolation point 1
(Piece-wise linear)	F_1	Force of interpolation point 1
	D_2	Displacement of interpolation point 2
	F_2	Force of interpolation point 2
	D_3	Displacement of interpolation point 3
	F_3	Force of interpolation point 3
	D_4	Displacement of interpolation point 4
	F_4	Force of interpolation point 4

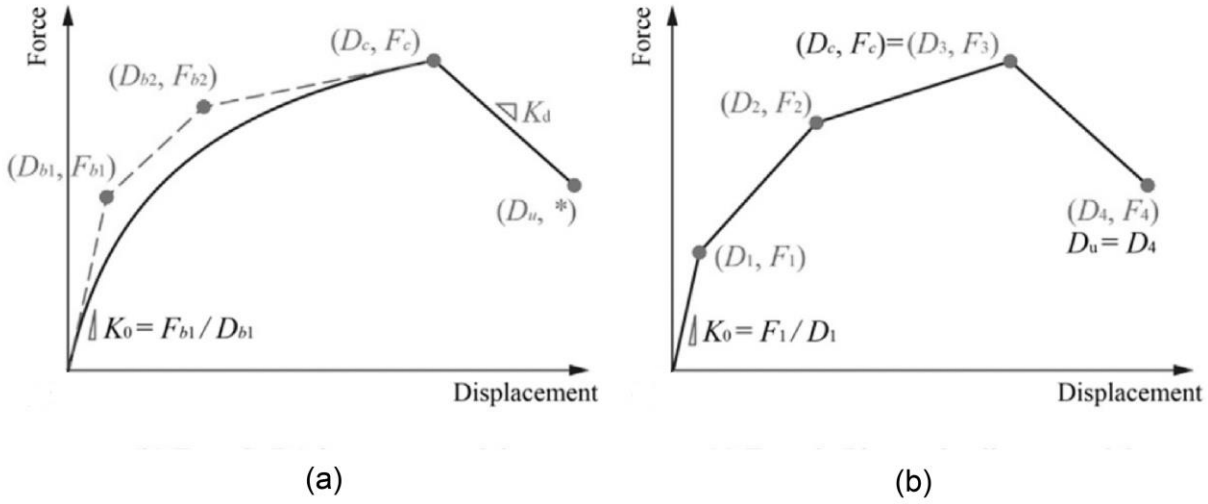

Figure appx. C.4. Envelope curve models for DowelType material: (a) Bezier curve; and (b) Piece-wise linear.

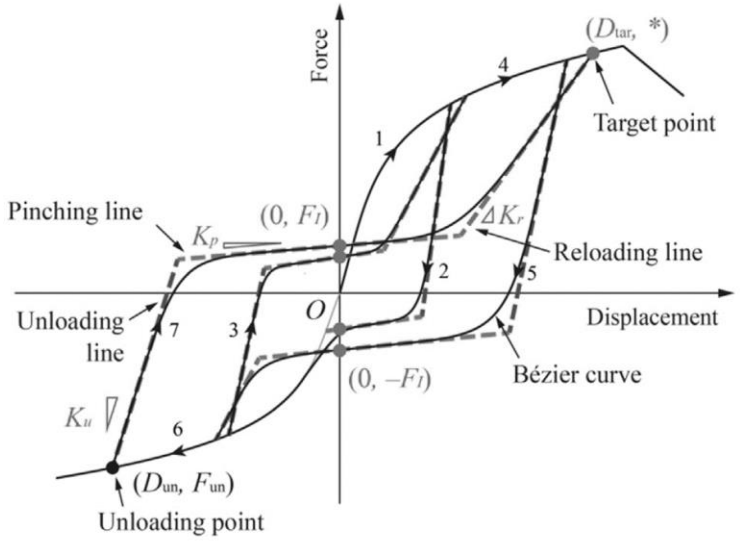

Figure appx. C.5. Hysteresis model in DowelType material.